ISBN 978-82-326-6222-7 (printed ver.)
ISBN 978-82-326-6604-1 (electronic ver.)
ISSN 1503-8181 (printed ver.)
ISSN 2703-8084 (electronic ver.)

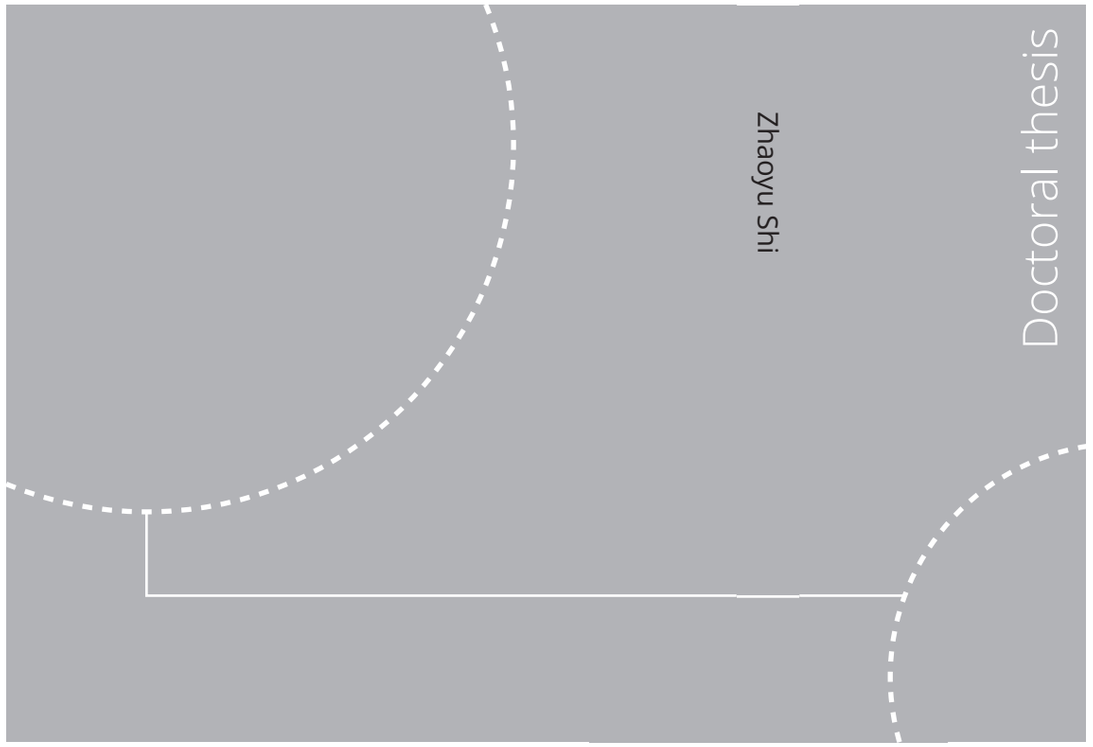

Doctoral theses at NTNU, 2022:51

Zhaoyu Shi

Numerical studies of particle clustering in circular cylinder wake flows

NTNU
Norwegian University of
Science and Technology

Thesis for the degree of
Philosophiae Doctor
Faculty of Engineering
Department of Energy and Process Engineering

NTNU
Norwegian University of
Science and Technology

Doctoral theses at NTNU, 2022:51

NTNU

Zhaoyu Shi

Numerical studies of particle clustering in circular cylinder wake flows

Thesis for the degree of Philosophiae Doctor

Trondheim, Feburary 2022

Norwegian University of Science and Technology
Faculty of Engineering
Department of Energy and Process Engineering

NTNU
Norwegian University of
Science and Technology

NTNU
Norwegian University of Science and Technology

Thesis for the degree of Philosophiae Doctor

Faculty of Engineering
Department of Energy and Process Engineering

ISBN 978-82-326-6222-7 (printed ver.)
ISBN 978-82-326-6604-1 (electronic ver.)
ISSN 1503-8181 (printed ver.)
ISSN 2703-8084 (electronic ver.)

Doctoral theses at NTNU, 2022:51

PRINTED IN NORWAY
NO - 1598

NORDIC SWAN ECOLABEL
Printed matter
2041 0731

Printed by Skipnes Kommunikasjon AS

Preface

This thesis is submitted to the Norwegian University of Science and Technology (NTNU) for partial fulfillment of the requirements for the degree of doctor of philosophy. The doctoral work has been performed at the Department of Energy and Process Engineering (EPT) from September 2018 to November 2021. The work has been supervised by Professor Helge I. Andersson and co-supervised by Associate professor Lihao Zhao from Tsinghua University and Doctor Fengjian Jiang from SINTEF Ocean.

The research has been fully funded by NTNU Energy.

The thesis is made up of four chapters and six scientific papers. The first two chapters introduce the background and progress in the field of particle-laden flow, explain the physical insights and the numerical approach. The research articles are summarized in Chapter III and included in full text at the end of the thesis.

Trondheim, December 2021
Zhaoyu Shi

Abstract

The emphasis of this thesis is to investigate how inertial point particles are clustered and dispersed in the wake of a circular cylinder with an uniform free stream. The numerical simulations that directly solved Navier-Stokes equations were carried out to achieve the single-phase carrier flows in a range of Reynolds number (Re). The movement of spherical particle is one-way coupled to the fluid element and solely subjected to the viscous drag force.

The continuous study of particle concentration starts from the 2D unsteady laminar wake. The particle-cylinder impaction at the front-side cylinder induces a peculiar bow shock cluster convected downstream. The radial component of viscous drag force, as balancing the centrifugal force, alters the direction around the inflection point along particle trajectory. This physical mechanism indicates a convergent tendency that contributes to the dense concentration. In the near wake, the path memory effect along particle trajectories was found to result in the smooth clusters encompassing the local vortex cells at the upstream side. The aiding and opposing dynamics are different for particles emanating from the opposite sides of the cylinder, and lead to different concentration patterns.

As Re increases to the transition-in-wake regime, the mode A instability gives rise to the streamwise vortical braids. The presence of the secondary vortices shapes the particular clustering topology and tends to attenuate the space-averaged particle velocity. A new criterion of defining clusters and voids was proposed based on the co-variance of Voronoï volumes and local flow quantities. This approach is suitable for the present flow where inertial particles are preferentially sampled by velocity gradients. The effect of particle inertia varies non-monotonically in Stokes number (Sk) with the strongest preferential concentration at $Sk = 1$, as the majority of particles are located in high-strain/low-vorticity regions.

In a shear layer instability-induced turbulent wake, the finer vortices are likely to increase the mixing thus weaken the preferential concentration.

The less asymmetric sampling of rotation- and strain-dominant regions indicates the non-negligible role of other mechanisms yet unknown. Another manifestation of an enhanced mixing is the smaller physics-based threshold for void scale than the conventional probability-density-based counterpart. A further investigation of the potential mechanism is possible via a scale-filtering analysis.

Acknowledgements

At this moment of collecting my memory of the sneakily past three years, it just strikes me that this adventure really comes to an end and I can actually escape for a 'real' vacation without checking emails and worrying about CPU hours! My PhD journey could be unexpectedly bumpy without the supports in any form from all lovely people I have luckily met.

First and foremost, I would like to extend my appreciation to my supervisor Helge Andersson. You have always left me enough freedom to mature my own ideas yet at the same time closely guided me through the bottlenecks. Your preciseness and high standards in many senses benefit me a lot in my transition to be a qualified and independent researcher. I feel more confident with so much trust and encouragement you offered. Besides our academic interaction, I so enjoyed our chats about many other topics, especially your taste in music! (thanks for introducing great Norwegian musicians to me)

My co-supervisors, Lihao Zhao and Fengjian Jiang, are always there whenever I need discussions, even though Lihao was far located in Beijing that we had to hold you til late night! I am particularly thankful to Fengjian, for your considerate guidance and patience in my two-month code training in Marine Tech and for your enthusiasm and optimism that always saved me from my excessive introspection. I must also thank Jason Hearst for including me into your turbulence experimental group meeting and opened a new door outside my numerical terrain. The fluid bowl karting event that almost got me 'killed' shall be never forgotten with my trophy reminding me everyday!

There are so many wonderful moments bringing to mind, my dear fellows in the bubble of Thermo-fluid lab. Thank you guys for all the terrific skiing and hiking trips, lighthearted lunch and coffee routines, barbecues, beers and concerts. I would like to give special thanks to my three amazing officemates who accompanied me the most and longest at different stages. Pawel, I am always impressed and motivated by your knowledge, sharp mind, curiosity

to any new scientific problems and also your cool personality. I missed our fruitful and inspiring discussions over many fluid topics. Anna, thanks for acquainting me into this growing lab after you moved in and you are always a helpful and cheerful good friend both in and out of office. Pim, moving to your office turned out to be such a pleasure. Your mental support and academic help (my cover letter instructor!) are much appreciated.

Mom and Dad, thanks for everything you provided to get me this far. You always embolden me to face the certain uncertainties in life.

Florian, at this point, ever knowing you, has already been a healing gift to me. Thank you, for all the care and joy you ever warmed me with in the past years, for respecting our parting in this path. I wish you nothing but the best as a dear old and new friend.

Contents

The task is not to see what has never been seen before, but to think what has never been thought before about what you see everyday.

— *Erwin Schrödinger*

1 Introduction

This thesis presents the computational investigation of flow past a circular cylinder laden with inertial particles. On one hand, the suspended particles are self-organized due to their intrinsic inertia; on the other hand, the unsteady vortex shedding and local vortex structures are influential to the final fate of particles. Our main goal is to better characterize their dynamics and distributions in the near wake at different regimes. Of most importance is to explore its accountable mechanisms. This introductory chapter provides the motivation which covers a broad relevant viewpoints. An overview of particle-laden wake flow and some core concepts are described in separate sections.

1.1 Motivation

Driven by the innate curiosity towards fluid dynamics, it always feels mesmerizing to observe a mayfly drifted in a vortical stream during a hike break, a toothpaste foam bubble swirling into a sink hole, or flocks of birds formation over clouds as lying on beach. The hard truth, however, is that the beauty of nature often strongly implies the presence of complex systems in every detectable scale[1]. One contributor to the complexity is the inter-

[1] It feels obligatory to hereby mention Nobel Prize Physics of year 2021, which appreciated the fundamental contribution to complex (chaotic) systems from atomic to planetary

play process between multiple phases in real-world environment, such as aforesaid dispersed (bubbles, birds) and continuous (river, air) phases. This long-existent two-phase problem has fascinated mathematicians and physicists to solve the puzzles embedded in abundant phenomena for decades. Precisely, it is referred to particle-laden flows, where the suspended particles are entrained by continuous carrier flow.

A prudent physics-based understanding of particle-laden flow is of substantial relevance to not only the romantic nature but practical lifematter issues. As the pandemic of COVID-19 hit the world from 2019, massive attention has been cast on airborne transmission of respiratory virus-laden droplets or aerosols[2] under different environmental conditions (humidity, temperature) (Ng et al. 2021). The exhalation process can be modeled as respiratory turbulent jet flow generating the clouds/puffs. To this point, one can be fully aware of the significant perspectives from fluid dynamics, particularly as a particle-laden flow problem, to understand the spreading of respiratory disease[3].

Let us extend our vision to a kilometer-based meteorological scale, the side effect[4] brought by global warming has aroused immediate and paramount investigations of fluid dynamicists. The formation and growth of atmospheric clouds are significantly related to climate change (Grabowski and Wang 2013, Shaw 2003). Besides the collision-coalescence of droplets/aerosols in vortical atmosphere, the wake-induced activation of ice particles within a cloud is also a relevant physical process (Bhowmick et al. 2020a,b). The eruption of volcanic plumes/ash also affect the environments in a long period, which is closely relevant to the growing topic of compressible particle-laden flows. A physics-based prediction of ash/dust dispersion and deposition in atmosphere is important to take precautions. In the oceanic context, the transportation of oil spills and micro-plastic pollution around obstacles (islands) are at play in environmental issues. The ecological systems often

scale by three scientists (Schirber 2021). Challenges for all humans, such as climate change and pollution, are closely relevant to fluid dynamics, particularly turbulence.

[2]Droplet size ranges from $O(1\mu m)$ to $O(1mm)$(visible to naked eyes); droplet nucleus is roughly smaller than $\sim O(10\mu m)$; aerosol generally describes any matter suspended in air.

[3]The thought-provoking discussions in Bourouiba (2020), Mittal et al. (2020) both stressed the somewhat neglected thus slowly advanced research of transmission, from a flow physics point of view. A long-term dedication is much constructive than a crash course driven by an urgent need of certain knowledge and guidance.

[4]Since July 2021, rare and catastrophic floods damaged over western Germany and Netherlands. Soon later, similar floods occurred in Henan and Shanxi (my home province), China.

Figure 1.1: Left: volcanic peaks of Cabo Verde disrupt an atmospheric flow accustomed to an empty ocean; air wraps around the volcanoes and creates vortex shedding (image credit: L.Dauphin/NASA; via NASA Earth Observatory). Right: Mauritius oil spill in Indian Ocean; oil droplets float around an island (image credit: Mauritian Wildlife Foundation Ministry).

involve the transportation of aquatic organisms or phytoplankton as encountering coral vegetation, of which the mechanisms can be investigated as modeling particles past a cylindrical structures (Espinosa-Gayosso et al. 2013). Further broadening the scope even to a planetary scale, the accretion of small dust particles around a planetesimal can be modeled as particle-laden wake flows (Homann et al. 2016).

In industrial scenarios, suspended particles in wake flows can cause irreversible impacts, such as scouring around the offshore wind-turbine foundation by sediments at seabed, clogging of combustion system or nuclear power plants. Our motivation for this thesis work can start from this practical application to contribute the knowledge of particle behaviors in bluff-body flows. The fundamental physical insights can always be applied or improved in investigating other similar conditions. Beyond the significance of turbulent flows, particle dispersion at laminar regime also has practical values, for instance of the separation of cancer cells at microfluidic biological devices. Such flow problem is ubiquitous in a wide range of spatial and temporal scales. However, as the quote of this chapter illuminates, it is frequently encountered in many situations, yet clearly lacks of persistent explorations til today, despite of being limited by the available tools at the time.

As one may agree, any real-life physical problem needs to be mathematically modeled to feature the essential properties. The most classic one to represent bluff-body flow is the circular cylinder wake, which has been extensively scrutinized for decades. It exemplifies that a simple geometry can give rise

to complex vortical flow. Experimental approach is natural and more accessible to reach turbulent condition, in contrast with computational efforts. The later one, however, advantages to manipulate certain inevitable factors in lab, such as gravity, boundary condition effect etc. The maturity and accessibility of supercomputers[5] enable the close-to-reality computations of single- and multi-phase flows nowadays. All analysis achieved in this thesis research are based on the high-fidelity and high-resolution numerical simulations directly solving the full Navier-Stokes equations, with the aim to provide more in-depth physical interpretations.

1.2 Single-phase circular cylinder flows

In reality, a bluff body (i.e. island, submarine, bridge) often possesses complex geometry with irregular edges and shapes. A circular cylinder has been serving as a prototype for flow past an obstacle since it can qualitatively characterize the bluff-body flows, such as vortex shedding, separation etc. Such a geometric simplicity though can give rise to a complex wake flow problem, which has been actively investigated and updated till today (see a comprehensive introduction by Zdravkovich (1997)). The state of unladen single-phase circular cylinder flow depends on the non-dimensional Reynolds number $Re = U_0 D/\nu$ (U_0 free stream velocity[6], D cylinder diameter, ν kinetic viscosity). Three major regimes based on Re-range were summarized by Williamson (1996) to describe the development of unsteady flow[7], i.e. 2D laminar vortex shedding, 3D wake transition, turbulence. The present PhD involves all three regimes, despite that the shear-layer induced turbulence for the last case is relatively weak but the computational cost is affordable.

Transition-in-wake

We start with Kármán street vortex featuring the 2D unsteady laminar regime in a range of $49 < Re < 194$. Strouhal number $St = fD/U_0$ measures the shedding frequency f, which increases with Re before the onset of three-dimensionality, see Figure 11 in Williamson (1996) of Strouhal-Reynolds

[5] An updated rank of worldwide supercomputers can be found in `www.top500.org/lists/top500`, in terms of only computing power.

[6] Incoming flow can be uniform and laminar (U_0 is constant) or turbulent (U_0 is mean flow velocity)(Aarnes et al. 2018). Without specification in this thesis, uniform free stream is referred by default.

[7] At very low Re(<40), flow is highly viscous thus maintains laminar and steady, known as creeping flow. As Re increases to $\approx$ 47, a Hopf bifurcation generates the periodic oscillation and the flow becomes unsteady. This steady regime is out of our interest though.

number relationship. As Re further increases ($190 < Re < 230$), a secondary instability, also known as *mode A* instability, is developed in wake, where the consequent occurrence of finer-scale loops evolve into streamwise vortices (ribs). The primary shedding vortices (rollers) become wavy due to the spanwise variation, resulting in a $3 \sim 4D$ spanwise wavelength λ_z. The onset of three-dimensional transition-in-wake can be detected by a discontinuous drop in $St-Re$ variation as the sub-critical instability of mode A emerges. A sharper drop on St can also be observed as the intermittent spot-like vortex dislocations caused by mode A instability appear (Zhang et al. 1995). Those large-scale vortices adhering to the cylinder are discovered to be responsible for the low-frequency velocity fluctuations (Williamson 1992).

The other successive phase in transitional wake, termed as *mode B* instability, develops as Re exceeds 230. The finer streamwise vortical braids with $\omega_z \approx 1D$ alternate in-phase, the opposite with the case in mode A. A hybrid of mode A and B exists in a range of $210 < Re < 220$. As mode B develops alongside with mode A, the shedding frequency increases asymptotically to a 2D state. The identification of critical Re in wake transition is sensitive to other objective factors, such as spanwise length of computational domain, blockage ratio and near-cylinder spatial resolution.

Often one can observe the oblique shedding either arsing from the shear layer and growing downstream, which was interpreted as end-wall effect by Williamson (1996) in experimental scenario. However, this seemingly robust explanation fails as oblique shedding still exists observed in our computational results at $Re = 200$ using periodic boundary condition in spanwise direction (an auxiliary finding from Shi et al. (2021b)). This numerical examination indicates a misleading understanding by end effect. A clear lack of relevant investigations on the physical significance to the formation and growth of oblique shedding. We attempted to explore the association with characteristic natural vortex dislocations (c.f. article 4.2).

Transition-to-turbulence

As Re reaches a sub-critical range of $(10^3, 2 \times 10^5)$, the transition to turbulence is induced by shear layer instability. Further increasing Re to post-critical regime, the boundary layer on cylinder surface becomes turbulent. In the context of numerical simulations, it is accessible to obtain a sub-critical case for comparison with equivalent experiments (PIV). A benchmarking $Re = 3900$ has been extensively studied mostly by means of large eddy simulation (LES) (Kravchenko and Moin 2000, Parnaudeau et al. 2008) and a few direct numerical simulations (DNSs) (Dong et al. 2006, Strandenes

et al. 2017).

Discrepancies between experiments and simulations still exist since such unsteady flow is sensitive to spanwise configuration, resolution in the vicinity of cylinder, statistical time period, the choice of subgrid scale model etc. A high-resolution DNS is expected to improve the reliability yet knowingly costs a substantial computational power. The region of interest is cast on the near wake ($0 < x/D < 10$), where the important dynamic behaviors, such as shear layer separation, subsequent rolling up process, formation and shedding of detached primary vortices, can be observed.

Characteristic variables, such as recirculation length, Strouhal number, hydrodynamic forces, Reynolds stresses, separation angle, mean velocity profiles are compared with experimental data to examine the development of turbulence. Of particular importance is reciculation length L_r[8], which is a deciding qualification of agreement between experiment and LES. It is especially sensitive to the statistical sampling period, which was suggested variously from 50 (Dong et al. 2006), 250 (Parnaudeau et al. 2008) to 400 vortex shedding periods (Strandenes et al. 2017). Other factors, such as boundary condition, spanwise length and subgrid model, also can shift the value of L_r within a small range. The recirculation length is found to remarkably decrease with increasing Re in shear-layer instability regime. Another characteristic length representing vortex formation $L_{\langle u'u' \rangle}$[9] is obtained given the single-peak value of $\langle u'u' \rangle$ in LES. The two-peak $\langle u'u' \rangle$-profile in PIV measurements leaves uncertainty though two peaks are close[10]. The local peak of $\langle u'u' \rangle$-variation in streamwise is not evidently associated to certain vortical mode while its transverse variation (y/D) indeed reveals the presence of up/bottom shear layer. Strandenes et al. (2017) demonstrated the quite evident effects of boundary condition (periodic/no-slip) and span length in spanwise.

In recirculation region ($0 < x/D < 3$), the U- and V-shape of mean streamwise velocity profiles at three typical streamwise positions[11] characterize the strong velocity deficit in the near wake. The disagreement of LES and

[8] The distance between the base of cylinder and the sign-change x-position in centerline of mean $\langle u \rangle$-profile.

[9] The distance between the base of cylinder and the x-position corresponding to the peak value of $\langle u'u' \rangle$-variation in centerline (u' streamwise velocity fluctuation).

[10] Parnaudeau et al. (2008) suggested to use $\langle v'v' \rangle$-profile to define vortex formation length since the peak is always observed in centerline.

[11] One in the very near wake: $x/D = 1.06 \leqslant 1.3$; the other two in recirculation region: $x/D = 1.54$ and 2.02.

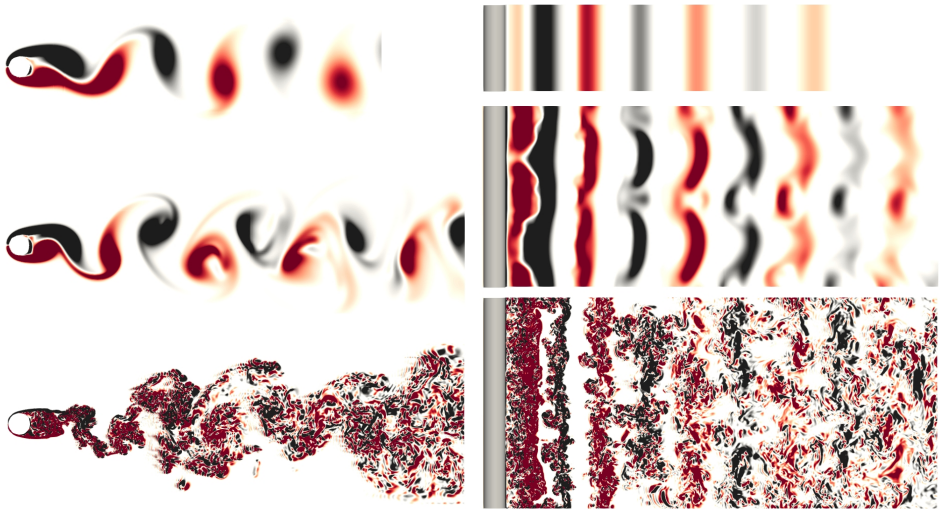

Figure 1.2: Contours of instantaneous primary vorticity ω_z in a (x, y)-(left) and (x, z)-(right) plane at three typical $Re = 100$ (top), 200 (middle) and 3900 (bottom), representing 2D unsteady laminar regime, 3D transitional wake with mode A instability and shear-layer induced turbulent wake, respectively.

experiments of U/V-shape at a fixed position are heavily sensitive to the averaging time interval, spanwise resolution and length. Mesh refinement seems not greatly affect the prediction of mean velocity. A summary of characteristic variables from available experimental and numerical references can be referred to Jiang and Cheng (2021), Lehmkuhl et al. (2013).

1.3 Particle-laden wake flows

Numerous efforts at both numerical and experimental levels have been made on investigating particle-laden flows with a long history. Given the fundamental properties and accessibility of homogeneous isotropic turbulence (HIT), the insights we obtained so far benefit a lot from research of paradigmatic particle-laden HIT. Nevertheless, particle transportation in different carrier flows can not be generally characterized, as a consequence of distinct vortex structures. For instance of vortex-dominant or wall-bounded flows with fairly large velocity gradient in some directions, the non-homogeneity can bring quite different concentration patterns from HIT. An upcoming review article by Brandt and Coletti (2022) will report the significant progress from both numerical and laboratory perspectives, involving a wide range of aspects.

The pioneering studies on particle-laden vortical flows shed light on free shear layers, such as plane mixing layer, plane wake and axisymmetric jet [12]. By contrast, numerical investigations were developed behind, of which the seminal work by Tang et al. (1992) employed discrete vortex method (DVM) to simulate a plane wake formed by a thick trailing edge. Particle dispersion in jet flow has also been earlier explored (Lau and Nathan 2014, Longmire and Eaton 1992) in respective of concentration pattern at various configurations (mass loading, particle inertia). Particular interest is given to the near-field jet flow, which approximates 2D axisymmetric flow dominated by large vortex rings while the helical structures in far-field are less coherent. Particle clusters are also co-paired with the corresponding vortex rings.

Particle-laden cylinder wake flow, however, greatly lacks of in-detail quantified investigations both numerically and experimentally. The earliest attempts mostly used analytically modeled vortex arrays to mimic Kármán street, such as the 2D co-rotating periodic Stuart vortex arrays (staggered point vortices) (Burns et al. 1999), steady Burgers vortex (Marcu et al. 1995). Jung et al. (1993) modeled a 2D periodic flow in the wake of a cylinder, analytically described by stream function to qualitatively represent N-S equation. The finding of periodic orbits for passive tracers at the very rear of cylinder, inspired the follow-up study on advection of finite-size particles in such chaotic system, i.e. von Kármán flow (Benczik et al. 2003). Equipped with the developed perturbation study (Burns et al. 1999) and dynamical system (Benczik et al. 2003, Jung et al. 1993), a series of studies on inertial particle's asymptotic behavior, i.e. attracting slow manifold, have been extended from 2D laboratory scale (Haller and Sapsis 2008) to 3D hurricane scale (Sapsis and Haller 2009). A reduced-order Maxey-Riley equations for inertial particle's motion (see details in chapter 2.3), was developed yet restricted in low particle inertia and small particle size. This set of theory has been assisted with a kinetic-model-based machine learning approach to predict particle trajectory (Wan and Sapsis 2018). Such spatially smooth, analytical Kármán flow has also been applied in other relevant studies with inclusion of memory force (Daitche and Tél 2014) (introduced below in 1.4).

The advantage of abovementioned simulated Kármán wake apparently can reduce the computational cost at presence of turbulence and the large-scale vortex structures are believed well-depicted. The downsides are also in-

[12] An earlier review by Fessler et al. (1994) can be referred to experimental research of particle concentration in abovesaid three vortical flows and wall-bounded flows, at the time of publishing. Another review by Elghobashi (1994) at the same year summarized the numerical development on particle-laden turbulent flows.

evitable, namely, no individual model can take all intrinsic features of real-life circular cylinder wake into account, such as three-dimensionality, viscous effect or unsteadiness at the same time. The development of DNS on turbulent multiphase flow in recent decades, enables us to overcome the disadvantages of those constrained models and obtain a sufficiently resolved cylinder wake flow. A number of earlier attempts provided introductory observation on clustering patterns varying with particle inertia and Reynolds number (Liu et al. 2015, Luo et al. 2009, Yao et al. 2009). Particles are one-way coupled to fluid velocity in most available studies, nevertheless, efforts have also been made in two-way coupling (Burger et al. 2006, Liu et al. 2015). Liu et al. (2015) performed the benchmarking turbulent case at $Re = 3900$, where particle feedback stimulates the appearance of V-shape profile in a shortened recirculation region and the suppressed vortex shedding due to enhanced drag force[13]. Burger et al. (2006) investigated the effect of particle inertia and loading on phase instability in an oscillating laminar droplet-vortex system.

Other relevant studies (Aarnes et al. 2019, Haugen and Kragset 2010) also briefly presented the particle concentration in a well-resolved circular cylinder flow, yet with an emphasis on particle-cylinder impaction in the near-cylinder region (Jørgen 2018)[14]. Investigations of particle-laden sphere wake are worth mentioning since the essential characterizations are similar in bluff-body flows. A few extensive studies provided the informative input in this somewhat overlooked field, of which Homann and Bec (2015) compared three profiles of mean preferential concentration at three regimes while Homann et al. (2016), Vallée et al. (2018) focused on Re- and particle inertia-dependency on particle-sphere collision[15].

Although the previous attempts on particle-laden circular cylinder flow laid a foundation of descriptive information, the valid quantitative analysis through meaningful physics-based statistics is apparently insufficient. The updated experimental input is also in great need on this important particle problem. Dedication of the present PhD work is to contribute more precise

[13]Earlier, the same group conducted two-way coupling DNSs of particle-laden jet (Gui et al. 2013), where particle inertia- and mass loading-dependency were reported in terms of flow structure, velocity profiles, turbulence intensity, particle concentration and so on.

[14]Instead of setting a uniform incoming flow, authors generated a turbulent free-stream to investigate its effect on front-side impaction efficiency.

[15]The study of collision efficiency in a sphere wake is of relevance for the accretion of dust in planet formation, ice nucleation or aerosol scavenging in meteorological context (Chouippe et al. 2019). A better understanding of heat and mass transfer of rain or clouds is essential to predict global warming.

observations of particle clustering by means of the high-resolution numerical simulations and explore the responsible mechanisms aside from the known. More detailed introduction of the included articles can be referred to chapter 3.

1.4 Mechanisms of preferential concentration

One can easily take *preferential concentration* (Squires and Eaton 1991) and *clustering* as equivalent to describe the non-uniform distribution of inertial particles. The slight distinction narrates in that the later particularly specifies the clusters at high-strain/low-vorticity regions while the former refers to spatial non-uniform distribution[16]. Preferential sampling and clustering are strongly dependent on particle inertia, typically measured by a non-dimensional parameter $Sk = \tau_p/\tau_f$ (i.e. ratio of particle residence time τ_p and fluid time scale τ_f).

Centrifugal mechanism

The conventional *centrifugal* ejection (Eaton and Fessler 1994, Maxey 1987) perceptually explains the clustering in general cases. The dominance, however, varies with different types of flows and there exists a Sk-regime indicating the existence of other mechanisms. Nevertheless, the strain-vorticity-dominant mechanism has been demonstrated in 2D laminar plane wakes, mixing layer and Kármán vortex street, where inertial particles are repelled away from vortex cores and thereby cluster in low-vorticity regions. *Voids*, regions depleted of particles, co-appear with clusters as a result of centrifugal ejection. Tang et al. (1992) also proposed a stretching-folding mechanism in mixing layer where vortex mergering contributes to the focusing of inertial particles. In cylinder wake flows, this mechanism is not applicable since a pair of two opposite-sign vortices barely sustain the vortex paring process. Preferential concentration in wake exhibits more organized than in mixing layer. The contribution of large-scale vortex structures to preferential concentration is supported by the subsequent experiments (Yang et al. 2000).

An unambiguous definition of *cluster* is given in a review by Monchaux et al. (2012) as *'groups of particles that remain close to one another (and possibly interact) on time scales long compared to some turbulence time scale'*, and further addressed as *'dynamical evolutive entities implying possible collective effects'*. It is noteworthy that clusters still lack of a concrete topological

[16] Bragg et al. (2015a) mentioned scenarios where clustering can appear without preferential concentration regardless of their locations characterized by local flow quantities, such as in white-noise flow (Bec 2003) or in the presence of gravity Tom and Bragg (2019).

definition despite of the common statistical approach (c.f. section 2.6)[17]. Clusters are found to be coherent, by that it means the formation is in relation to the coherent vortex structures, for instance of Kármán rollers in laminar wake (Shi et al. 2021a) and statistical self-similarity eddies at dissipative scale in turbulence (Baker et al. 2017). Turbulence-driven clustering is associated with the multi-scale nature of turbulent flow. Centrifugal mechanism has been corroborated to be robust within sub-Kolmogorov regime $Sk \ll 1$[18], where the self-similar coherent clusters are only Sk-dependent.

Sweep-stick mechanism

Although vortex ejection can be extended to an effective dissipation scale (up to $O(10\eta)$)[19], it fails to explain the scale-variant preferential concentration at high Re. The role of multiscale coherent vortices should be taken into account to interpret the properties of particle concentration (Bec et al. 2007, Yoshimto and Goto 2007)[20]. Outside Kolmogorov regime $Sk \gg 1$, a strong correlation of fluid acceleration field and clustering of heavy particles has been suggested (Bec et al. 2007). Particles can be therefore sampled not only by vorticity field, e.g. Q-invariant of velocity gradient tensor (Baker et al. 2017, Shi et al. 2021b)[21], but also local fluid acceleration. The *sweep-stick* mechanism was wherefore developed (Coleman and Vassilicos 2009), where particles tend to stick to and thus move with zero fluid acceleration points instead of low-vorticity points, independent of Sk. For those particles on low acceleration regions, a velocity of acceleration field demonstrates the sweeping of such regions by local fluid velocity. Coleman and Vassilicos (2009) suggested the reasonable extension to inhomogeneous flows, which could be investigated in particle-laden wake flows. Generally, centrifugal mechanism prevails at low Sk and Re regimes while sweep-stick mechanism plays a leading role at $Sk > 1$ and high Re.

Non-local (path history) effect

An alternative, apart from inspecting the instantaneous outcome, is to investigate the resultant response at a given time of the constant interaction with fluid velocity or vorticity field at earlier times along its path history.

[17] Baker et al. (2017) used singular value decomposition (SVD) to detect the principal axes of each coherent cluster.

[18] In HIT, Stokes number is usually defined based on Kolmogorov scale, i.e. $Sk = \tau_p/\tau_k$.

[19] Baker et al. (2017) found that clusters persist to be self-similar at scale larger than twice the Kolmogorov length.

[20] Coarse-grained/filtered density or velocity gradient can be applied in turbulence to separate the effect of various scales on preferential concentration.

[21] Scalar field $Q = \frac{1}{2}(|\boldsymbol{\Omega}|^2 - |\boldsymbol{S}|^2)$(Hunt and Moin 1988), $\boldsymbol{\Omega}$ and $\boldsymbol{S}$ are the rotation- and strain-rate tensor, respectively.

For $Sk \geqslant O(1)$, Bragg and Collins (2014) proposed that a *non-local* effect outweighs centrifugal mechanism as another candidate besides sweep-stick mechanism. This physical explanation is also referred to *path history symmetry breaking*, which was derived from a Lagrangian analysis based on radial distribution function. Increasing particle pair separation $\boldsymbol{r}$ on average leads to a larger velocity difference between particle and local fluid element, vice versa. Therefore, the asymmetric variation of velocity difference with separation generates a net inward drift[22], indicating clustering. Furthermore, Bragg et al. (2015b) reported an enhancement of inward drift velocity by non-local mechanism increasing the clustering. Nevertheless, both preferential sampling and non-locality strongly contribute to clustering at $Sk = O(1)$. Bragg et al. (2015b), however, argues that sweep-stick mechanism does not provide more fundamental change from dissipative to inertial range since it is essentially equivalent to coarse-grained preferential sampling at $\boldsymbol{r}$ for $Sk_r \leqslant 1$[23] in inertial range.

A conceptually similar 'path history' effect has also been investigated by Shi et al. (2021a) in a laminar Kármán wake. An accumulation of a finite memory of influence by transient local vortices, indeed leads to a special clustering pattern (c.f. review of article 4.2).

Role of Basset history force

The mechanisms summarized above are all proposed with the assumption of heavy particles merely under viscous drag force. More studies considered the plausible non-negligible role of Basset history force, which describes the diffusion of vorticity around the particle during its full time history. One might confuse the abovesaid effects of path history origin and history force in governing equation, although they both reflect the footprints of particle inertial memory. The presence of history force is demonstrated in available literature to counteract the inertial effect/centrifugal force, resulting in a weakened preferential concentration in attractors (Daitche 2015, Olivieri et al. 2014). However, Daitche and Tél (2014) suggested that history force contributes a viscous effect but also can leads to the decreasing slip velocity, which indicates that history force can not be taken solely as a drag force since particle acceleration varies oppositely for heavy and light particles. A recent numerical study of particle dispersion over a duct cylinder (Bagheri and Sabzpooshani 2020), however, found that particle clustering at high Sk can be enhanced by the history force for both medium and high particle

[22] Analogous to *turbophoresis* in wall-bounded flows, where particles in regions with high turbulence intensity are drifted to lower counterparts (close to walls) without returning.

[23] Separation scale r-based Stokes number represents arbitrary spatial scale.

density at the presence of intense vortices in the near wake.

All consistencies and discrepancies within those fruitful research, have deepened our understanding in such complex particle-laden flows. Although the clustering mechanisms are still debatable in terms of scale-dependency and Sk-regime, it leaves us an ample room to explore even in paradigmatic HIT and convenient point-particle model. Comparable attention and investigations should be given to vortex-dominant flows, such as the prototypical cylinder wake flows. Distinct vortex structures may bring new mechanisms thus the validity of available mechanisms should be case-dependently examined.

Remember that all models are wrong; the practical question is how wrong do they have to be to not be useful.

— George E. P. Box

2

Methodology and Computational aspects

In this chapter the details regarding the numerical methods and modeling techniques for both fluid and particle phase are introduced. We chose to directly solve Navier-Stokes equations to obtain the physical characteristics at all spatial and temporal scales. Being mindful that the massive particle tracking involved with complex vortex structures can bear heavy CPU-usage, particularly for transition-to-turbulence and fully turbulent regimes. Nevertheless, the well-verified and highly paralleled code *MGLET*[1] utilized for this PhD work enables us to conduct particle-laden wake flows at a reasonable computational cost. The estimated millions of CPU-hours spent during three years are supported by UNINETT Sigma2[2].

2.1 Eulerian transient flow

Navier-Stokes equations

The incompressible flow is governed by the time-evolving Navier-Stokes

[1] Abbreviation for **M**ulti **G**rid **L**arge **E**ddy **T**urbulence. This DNS/LES solver is currently maintained by *Kreuzinger and Manhart Turbulenz GmbH* based in Munich.

[2] National Infrastructure for High Performance Computing and Data Storage in Norway.

equations for continuity and momentum of Newtonian fluid, which can be formulated in integral form as

$$\oint_A \boldsymbol{u} \cdot \boldsymbol{n} dA = 0 \tag{2.1}$$

$$\frac{\partial}{\partial t} \int_\Omega u_i d\Omega + \oint_A u_i \boldsymbol{u} \cdot \boldsymbol{n} dA = -\frac{1}{\rho} \oint_A p \boldsymbol{n} dA + \nu \oint_A \Delta u_i \cdot \boldsymbol{n} dA \tag{2.2}$$

since *MGLET* uses a second order finite volume method (FVM) in Eulerian reference frame spatially discretized on staggered Cartesian grids (Ferziger and Perić 2002). Herein, each control volume Ω is bounded by a surface A and $\boldsymbol{n}$ is the unit vector on dA pointing outwards the center of control volume. Integration of instantaneous velocity components and pressure are computed over the surface of control volume based on the midpoint rule[3], resulting in the volume-averaged fluid quantities in each grid cell. In this staggered arrangement, the updated pressure is preserved at the center of control volume while velocity components are stored at the center of cell faces.

2.2 Multi-level mesh generation

A high-quality mesh plays a significant role in obtaining a trustworthy simulated flow field as a foundation for subsequent statistical analysis. *MGLET* adopts a multi-level structured Cartesian grid to discretize the computational domain. The generated mesh is constructed with cubic boxes (i.e. grids) in a hierarchical arrangement, wherein the number of grids varies at different levels (i.e. sizes). All grids in spanwise direction is homogeneous and each grid is divided into $N \times N \times N$ cubic cells in equidistant spacing[4]. In contrast, the classic grid stretching technique applied in three dimensions can easily result in a waste of computation on the domain of non-interest, namely, the quiescent regions without significant vortices identified. Although the stretching method is well employed in channel flows or boundary layers, the present multi-gird method is apparently advantageous to bluff-body wake flows. It remarkably reduces the total number of cells thereby improves the computation efficiency.

Local refinement

[3]Integrals are the product of cell-surface area and integrand value at the surface center for all convective fluxes.

[4]The number of grid levels and N are jointly chosen to keep the total number of grid cells necessarily sufficient. Each core on supercomputer Betzy can safely handle no more than 5×10^5 cells with a feasible utilization of computational resources.

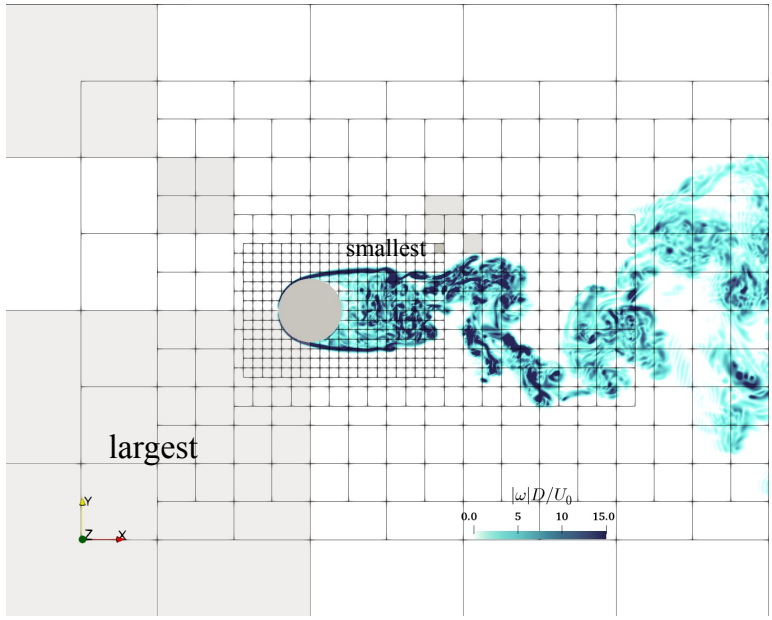

Figure 2.1: Illustration of a slice of computational domain in (x, y)-plane superimposed by vorticity magnitude $|\boldsymbol{\omega}|$, i.e. root square of enstrophy. Six grid levels are outlined by the shade squares corresponding to the decreasing size by a factor of 2. Each square, regardless of size, represents a grid box that consists of $N \times N \times N$ uniform cubic cells.

Multiple local refinements with various spatial resolutions can be enforced accordingly at regions of interest by a zonal algorithm (Manhart 2004). Each refinement is simply a cell splitting, where every parent-level grid is divided into eight equal 3D child cells. In the vicinity of cylinder, the finest resolution is enforced since the boundary layer and shear layer with large velocity gradient have to be accurately resolved. The instantaneous information of velocity components and pressure are preserved at every level of the whole mesh. A linear interpolation is imposed to merge data saved at various levels onto single-resolution Eulerian points in each dimension. The spacing between two points usually takes the second finest resolution, which is more robust than choosing the finest one. An arrangement of reasonably refined multi-grid mesh is exemplified in Figure 2.1 for the turbulent case, where the finest grid cells almost cover the recirculation region.

Cut-cell immersed boundary method (CCIBM)

The representation of a solid geometry is important to achieve a high-

Table 2.1: Computational set-ups and mesh parameters in simulations of Re = 200 and 3900.

Re	N_{core}	Δ_{min}/D	Δt	$L_x \times L_y \times L_z(/D)$	N_{grid}	N_{cell}
200	320	0.02	0.008	58.2×16.64×16.64	4068	7.15×10^7
3900	3200	0.005	0.001	81.6×38.4×9.6	33424	9.02×10^8

accuracy numerical solution. A solid object can be represented by either traditional body-fitted or non-body conformal grids[5]. The practical advantages of the later one are that all simulations are performed on Cartesian grids and the simplified mesh generation eliminates the concerns of grid distortion and high-cost iteration process especially for moving boundaries. The body-fitted mesh, however, does provide a highly accurate no-slip boundary condition (BC) on solid-fluid interface. Such Cartesian grid-based approach is referred as immersed boundary method (IBM) (Peskin 1972), and it stands out by the easy implementation of high-order schemes but also requires critical local fine cell size near IB.

The boundary condition on the immersed boundary is imposed by exerting a discrete forcing term in Navier-Stokes equation[6]. The idea is to transform the no-slip and impermeability boundary conditions at the solid surface (Lagrangian points) into internal BC at the nodes of Cartesian grids (Eulerian points). The immersed boundary is treated as a 'sharp' interface to avoid the spreading of effect of the IB, which are usually achieved by ghost-cell (GC) or cut-cell (CC) method to construct the stencil of IB (Mittal and Iaccarino 2005). The ghost-points inside a solid body and mirror-points in the adjacent flow are combined to reconstruct the solid boundary in GCIBM. The detailed procedure of implementing GCIBM in *MGLET* can consult (Peller et al. 2006). For the purpose of accurately resolving the impaction of particle and cylinder surface, the CCIBM can exactly compute the shapes of polyhedron cells intersected by the solid surface. The normal and tangential vectors of the intersected cells can be used to modify the kinetic energy loss as particles are detected to hit the cylinder. The finite-volume method can globally and locally guarantee the mass and momentum conservation with cut-cell methodology. A recent work (Roland and Kreuzinger 2021) ex-

[5] A hybrid method, i.e. *overset grids*, is worth mentioning which applies both techniques with the overlapped grid cells on top of one another (Jørgen 2018). It shares certain similarities with *multi-level grid*, such as the communication and interpolation between grids at different levels.

[6] A continuous forcing function (Mittal and Iaccarino 2005) is preferred by elastic boundaries, such as in blood flow (Peskin 1972).

ploited CCIBM in a compressible flute flow to investigate the flow-acoustic problem.

By far, *MGLET* exploiting IBM has been applied successfully in other bluff-body geometries with complex solid geometry, such as the concave curved cylinder (Jiang et al. 2019), step cylinder (Cai et al. 2020) and prolate spheroid (Strandenes et al. 2019).

2.3 Lagrangian particle dynamics

Maxey-Riley equation

The evolution of flow field is described in Eulerian space, provided that fluid element in carrier-phase is regarded as a continuum. A nontrivial alternative to improve the statistical analysis of turbulence is Lagrangian tracking of passively advected particles (i.e. tracers) (Toschi and Bodenschatz 2009). In the context of particle-laden flows, the suspended particles are considered inertial, whose trajectories depart from the streamlines of fluid-phase. The appropriate choice of mathematical modeling for individual particle's movement is dependent on particle class (see discussions below). The present PhD work considers a simple rigid sphere point-particle modeling described by Maxey-Riley (M-R) equation under Euler-Lagrange framework (Maxey and Riley 1983). These idealized particles are one-way coupled to the underlying flow at a low volume fraction, i.e. no feedback effect from particle dynamics on fluid. The full-term M-R equation in vectorial form is expressed as

$$
\begin{aligned}
\frac{\mathrm{d}\boldsymbol{u}_p}{\mathrm{d}t} = \underbrace{\frac{\rho_p - \rho_f}{\rho_p}\boldsymbol{g}}_{\text{I. bouyancy}} + \underbrace{\frac{\rho_f}{\rho_p}\frac{\mathrm{D}\boldsymbol{u}_{f@p}}{\mathrm{D}t}}_{\substack{\text{II. fluid acceleration force} \\ \text{(pressure gradient effect)}}} \\
+ \underbrace{\frac{\rho_f}{2\rho_p}\frac{\mathrm{d}}{\mathrm{d}t}(\boldsymbol{u}_{f@p} - \boldsymbol{u}_p + \frac{\mathrm{d}^2}{40}\nabla^2\boldsymbol{u}_{f@p})}_{\text{III. added mass}} \\
+ \underbrace{\frac{1}{\tau_p}(\boldsymbol{u}_{f@p} - \boldsymbol{u}_p + \frac{d^2}{24}\nabla^2\boldsymbol{u}_{f@p})}_{\substack{\text{IV. Stokes-like drag force} \\ \text{(viscous effect)}}} + \\
\underbrace{\frac{d}{2\tau_p}\int_0^t \frac{\mathrm{d}\tau}{\sqrt{\pi\nu(t-\tau)}}\frac{\mathrm{d}}{\mathrm{d}\tau}(\boldsymbol{u}_{f@p} - \boldsymbol{u}_p + \frac{\mathrm{d}^2}{24}\nabla^2\boldsymbol{u}_{f@p})}_{\text{V. Basset history force}}
\end{aligned}
\tag{2.3}
$$

where $\mathrm{D}/\mathrm{D}t = \partial/\partial t + \boldsymbol{u}_{f@p}\cdot\nabla$ denotes material/Lagrangian derivative along the local fluid element, $\mathrm{d}/\mathrm{d}t = \partial/\partial t + \boldsymbol{u}_p \cdot \nabla$ is the total derivative following inertial particle trajectory.

Note that M-R is valid as $Re_p = d||\boldsymbol{u}_{f@p} - \boldsymbol{u}_p||/\nu$ remains small ($Re_p \leq 1$), practically applicable up to $Re_p \approx 17$ found by Maxey et al. (1996). The viscous drag force (term IV) and history force (term V) represent the dissipative effect, despite that the former is a steady component while the later is a transient integral. In the limit of $Re_p \to 0$, the relative motion of inertial particle to the surrounding fluid is small, leading to the steady Stokesian drag force $\boldsymbol{F}_d = 3\pi\rho_f\nu d(\boldsymbol{u}_{f@p} - \boldsymbol{u}_p)$. Another assumption of the derivation of M-R equation is the small particle diameter, i.e. $d < \eta$ (the smallest resolved Kolmogorov scale), while the LES relaxes the criterion as d only needs to be smaller than the minimum spatial resolution or smallest resolved scale. At high Re_p, a single finite-size sphere can induce the wake evolved with complex physics to be taken into account, such as separation, recirculation and vortex shedding. For larger particles ($d \gg \eta$), there barely exists a relatively robust equation to predict their behavior.

Considerable efforts have been made to compensate errors due to finite-Re_p (a few hundred) effect by including empirical correction in Re_p-dependent term III, IV and V. Nevertheless, there lacks of confident formulations that can be generally applied in non-uniform flows (Balachandar and Bagchi 2003)[7]. Another tricky problem lies in a proper definition of slip velocity $\boldsymbol{U}_s = \boldsymbol{u}_{f@p} - \boldsymbol{u}_p$, wherein the choice of 'undisturbed' fluid velocity conditioned on particle position $\boldsymbol{u}_{f@p}(\boldsymbol{x}_p, t)$ is critical for either larger particle or two-way coupling scenario (i.e. including feedback of particle to fluid) (Bellani and Variano 2012)[8]. This concern is neglected in present work with restrictions on small particle size and Re_p.

Classification concerning mathematical modeling

The real-world particles suspended in oceanic or atmospheric flows are categorized into different particle classes characterized by particle size (d/η) and density ratio (ρ_p/ρ_f). A precise mathematical description of particle regime decides an appropriate computational approach, illustrated in Figure 2.2.

[7] The commonly used drag laws, e.g. Oseen correction, Schiller and Neuman formula, is well-justified as the flow is not greatly unsteady or vortical (e.g. shear flows). From a practical view, people mostly still stick to those well-accepted coefficients, arguably though.

[8] For solid spherical particle with $d > \eta$, immersed boundary method can be used to resolve the ambient flow (Lucci et al. 2010).

As addressed in conditions for M-R equation, the size of particle in present Euler-Lagrange point-particle approach should be smaller than the smallest scale of flow ($d/\eta \lesssim 0.1$, see Figure 2.2(a)), critically demanded in DNS for turbulent flows. Note that it does not necessarily require the actual physical size to be infinitesimal, despite the fact that aerosol in cloud is less than $1\mu m$ and cloud droplet in air only ranges within $1 - 20\mu m$ (Grabowski and Wang 2013)[9]. A comparison of point-particle model applied in DNS and LES can refer to a review by Balachandar (2009).

Irrespective of the small particle size, the level of two-phase interaction also greatly depends on fractional volume ϕ_v[10] (Balachandar and Eaton 2010, Elgobashi 2006). A small value of $\phi_v \leqslant 10^{-6}$ guarantees an insignificant momentum exchange between two phases due to negligible concentration (i.e. dilute suspension). In two-way coupling regime, the non-negligible alteration of particle dynamics on turbulence also depends on Stokes number $Sk = \tau_p/\tau_f$ ($\tau_p = \rho_p d^2/18\rho_f\nu$)[11]. Figure 2.2(b) illustrates a transition at $\tau_p/\tau_f \approx 10$, beyond which the large particles at $Re_p > 400$ produce wake flow corresponding to a fully resolved approach.

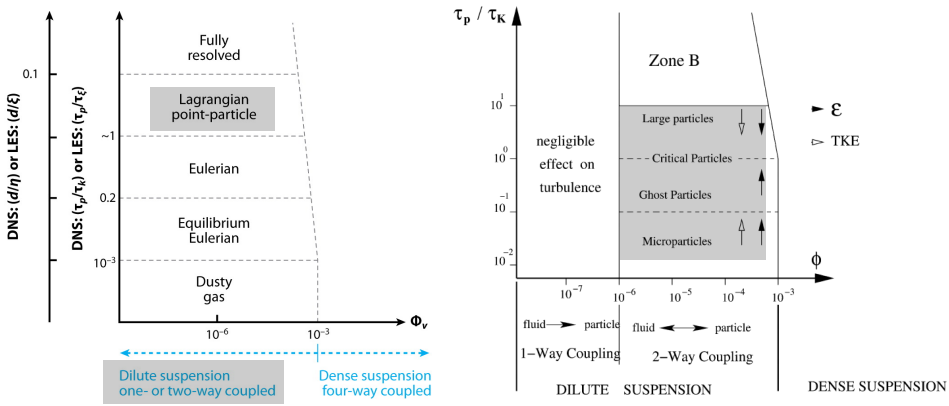

Figure 2.2: Computational approaches to particle-laden turbulent flows (Balachandar and Eaton 2010)(left) (Elgobashi 2006)(right). The classification map is separated by particle time scale, volume fraction and particle size. The present simulations adopts Lagrangian point-particle one-way coupled to local fluid in a dilute suspension.

[9]Brownian motion is out of consideration since the particle size is significantly larger than the molecular size (i.e. fluid mean free path).

[10]$\phi_v = N_p V_p/V$, N_p: total number of particles, V_p: volume of single particle, V: total volume of domain.

[11]The choice of τ_f can be nominally defined for book-keeping or associated with characteristic physical scale for different types of flow.

Besides, particle mass loading should be carefully chosen since an excessive value requires the inclusion of inter-particle collision and one particle's disturbance on the ambient fluid around another particle, i.e. four-way coupling. Often, in one-way coupled point-particle simulations, it is tricky to simultaneously satisfy the number of samples from statistical perspective and justify the dilute suspension. In practice, the number of particles $N_p \sim O(10^5)$ within the domain of interest can safely reach the balance. Additionally, the local preferential concentration for inertial particles is often questioned to take inter-particle collision into account. Being aware of this practical issue, our particular aim is to study individual particles' behavior instead of focusing on particle's interaction in present work.

As earlier introduced in chapter 1, preferential concentration indisputably depends on Sk, a function of both particle size (d/η) and density ratio (ρ_p/ρ_f). The latter one defines heavy and light particles relative to the corresponding carrier flow, of which examples are $\rho_p/\rho_f \approx 2$ for sand in water, $\sim O(10^2)$ for heavy droplet in air, $\to 0$ for spherical bubbles in water (Daitche and Tél 2014). Practically but not rigorously, as density ratio is larger than 10^3, the sufficiently small prefactors for fluid acceleration force and added mass in Eq.(2.3) allows them to be neglected. An evaluation of Basset force is necessary as this integral term requires the full history of particle acceleration yet the applied numerical scheme still remains an open question. Attempts have been made to estimate its contribution under different combinations of density ratio and Stokes number. Olivieri et al. (2014) found that Basset force roughly accounts for 10% of total force as $\rho_p/\rho_f = 10^3$ in a range of $Sk \in (0.1, 1)$, of which viscous drag force dominates. Daitche (2015) reported the particle size-dependency, wherein memory force is 7% of viscous drag force as particle radius $a/\eta \approx 0.1$.

Simplifications for present simulations

To this point, we are able to justify and specify the simplifications applied in present simulations. We consider pointwise heavy particles with a fixed density ratio $\rho_p/\rho_f = 10^3$, therefore larger Sk is obtained by increasing particle diameter[12]. The original M-R equation can be stripped down without fluid acceleration, added mass, history force. And gravity effect is excluded since the present work focuses on particle dispersion and mixing in the near

[12]Technically, there exists a threshold for Sk constrained by the assumption of small particle, i.e. $d < \Delta_{min}$. This criterion is more critical in turbulent case since a proximity of particle size to the smallest resolved scale presumably modulates turbulence thereby clustering pattern.

wake. Particle settling can be further investigated as an independent topic. For viscous drag force, the non-linear Faxén correction $\frac{\mathrm{d}^2}{24\tau_p}\frac{\partial u_{f@p,i}}{\partial x_j^2}$ accounting for the finite-size effect is theoretically negligible as long as $d < \eta$. In order to compensate the errors of deviated trajectories derived from particle size[13], a well-acknowledged empirical piecewise correction coefficient C_D as a function of Re_p is adopted in our codes (Cliff et al. 1978, Gobert 2010), given as

$$C_D = \begin{cases} 3/16 + 24/Re_p & Re_p < 0.01, \\ \frac{24}{Re_p}(1 + 0.15Re_p^{0.687}) + \frac{0.42}{1+4.25\times10^4 Re_p^{-1.16}} & Re_p < 3\times10^5. \end{cases} \tag{2.4}$$

On the variation of $C_D - Re_p$ shown in Figure 2.3, the drag force linearly decreases as $24/Re_p$ in the Stokesian regime ($Re_p < 1$). In the wake instability regime ($Re_p < 400$), Schiller and Naumann approximation $C_D = 24/Re_p(1 + 0.15Re_p^{0.6876})$ is also widely used and valid up to $Re_p = 800$. In a high subcritical flow regime ($400 < Re_p < 3.5\times10^5$), it is debatable to involve the transition to turbulence since the unsteadiness of the boundary layer and wake significantly affect the drag force[14]. The wake is laminar at rear of the cylinder and the boundary layer stays laminar as $Re_p < 3.5\times10^5$ (Cliff et al. 1978). In present simulations, the peak particle Reynolds number computed from the average slip velocity was quite small (below 10). The full M-R equation (2.3) is replaced by a simplified M-R as follows

$$\frac{\mathrm{d}\boldsymbol{u}_p}{\mathrm{d}t} = \frac{C_D Re_p}{24\tau_p}(\boldsymbol{u}_{f@p} - \boldsymbol{u}_p) \tag{2.5}$$

$$\frac{\mathrm{d}\boldsymbol{x}_p}{\mathrm{d}t} = \boldsymbol{u}_p \tag{2.6}$$

Initially, Stokes number is defined based on a nominal fluid time scale $\tau_f = D/U_0$ without revealing any relationship between particle relaxation time and physical time scale of cylinder wake flow, namely, it only serves for the purpose to introduce the inertia difference[15]. For cylinder wake flows, one characteristic time scale is vortex shedding period T representing a global time evolving. The other vorticity-based physical time scale

[13] At a given $\rho_p/\rho_f = 10^3$, the criterion of particle size $d < \eta$ can not be perfectly satisfied at larger Sk.

[14] C_D depends on surface roughness, fluid viscosity, particle shape and its rotation, flow compressibility etc. Herein we consider smooth sphere solid particle in a steady ambient flow.

[15] In HIT, Stokes number can be defined by the smallest Kolmogorov scale or the largest integral scale. The former is commonly used though to relate to the small-scale clustering.

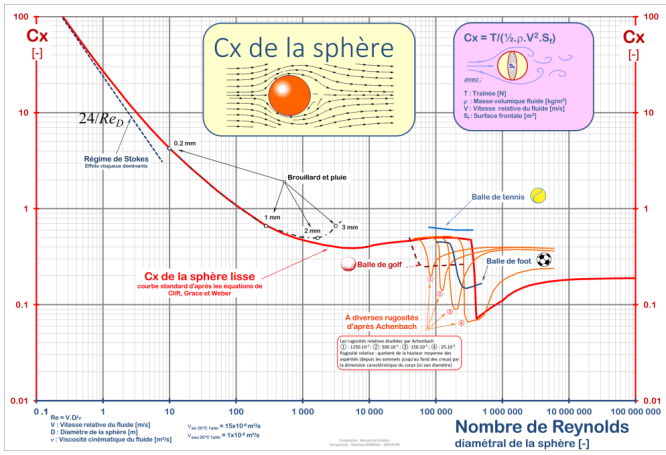

Figure 2.3: Drag coefficient C_D (equivalent C_X in y-axis label) versus particle Reynolds number Re_p (x-axis label). Red solid curve represents a smooth sphere; red dashed and orange curves denote golf ball and football ball with different relative roughness, respectively. (Source: wikimedia commons by Bernard de Go Mars, 2016)

is more applicable to manifest the local inertial effect. The present study prefers to use primary/spanwise vorticity to introduce the *effective Stokes number*, i.e. $Sk_e = \tau_p/\tau_{fe}$, $\tau_{fe} = 1/|\omega_z|$. For turbulent flows, the strengths of streamwise/crossflow vortices are relatively comparable to the spanwise vortices that are bulky and prominent in laminar flows. Alternatives of τ_{fe} can also be $1/|\omega_{x/y}|$ to investigate the effect of different components on particle clustering. This physically meaningful definition of Sk_e, however, has barely been considered in previous articles of particle-laden cylinder wake flow.

2.4 Numerical methods and computational details

Fluid phase

Once the spatial discretization of N-S equations by second-order FVM has been conducted, a third-order low-storage explicit Runge-Kutta scheme time integration (RK3) is used for time-advancing (Williamson 1980). Time step Δt is estimated by local maximum Courant-Friedrichs-Lewy (CFL) measured at the finest cell. Despite that RK3 allows for a larger CFL up to $\sqrt{3}$, a conservative criterion $\lesssim 0.5$ is complied to assure the convergence in second-order accuracy over space. An advantage of low-storage scheme is the relatively low demanding for large memory enforced by DNS if turbu-

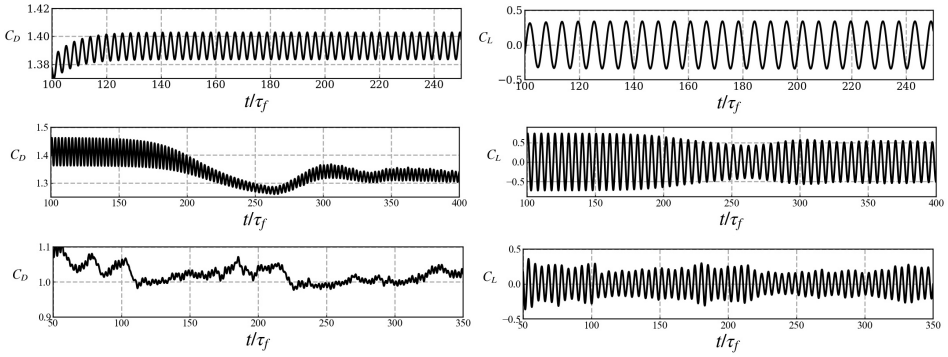

Figure 2.4: Time history of instantaneous drag (C_D) and lift (C_L) coefficients at $Re = 100$, 200 and 3900 (top to bottom). No constant sinusoidal oscillation can be found as $Re > Re_c = 194$.

lence involved, with a allocation of $3N$ storage locations (N the number of degrees-of-freedom in discrete space). The explicit form requires a pressure correction to fulfill continuity equation at each three substeps in RK3. The updated pressure $p_{new} = p_{old} + \delta p$ at each time step increases the memory storage by saving the solution of Poisson equation for pressure correction δp and the calculation of a divergence-free velocity field. The discretized Poisson equation is iteratively solved by Stone's strongly implicit scheme (SIP) (Stone 1968).

By monitoring the variations of drag (C_D) and lift (C_L) coefficients[16], one can inspect the state of transient flow. An illustration Figure 2.4 compares the coefficients at three considered Res. For two-dimensional vortex shedding, both coefficients vary sinusoidal after the initial numerical oscillation. As $Re > Re_c$ within the transitional regime, the time variation deviates from sinusoidal behavior once the vortex dislocation occurs and detaches from the cylinder surface. A drop of C_D and C_L is observed representing this intermittency, therefore no regular oscillation exists after the onset of three-dimensionality. The Strouhal number ($St = fD/U_0$) can be calculated by either Fast Fourier transform (FFT) or power spectral density (PSD) based on lift force[17]. The primary frequency can be estimated given either lift

[16] $C_i = 2F_i/\rho_f U_0^2 LD$, $i = D, L$ drag and lift force, respectively; L cylinder span length.

[17] Two approaches make no difference to obtain the dominant frequency for transitional or turbulent flows. Welch method (Welch 1967) and Lomb-Scargle periodogram (Scargle 1982) are often used to calculate PSD. The resultant amplitude values of PSD are real numbers by multiply its conjugate. The normalization to frequency bin width gets rid of the bin-width dependency, which works as an advantage than FFT for random signals.

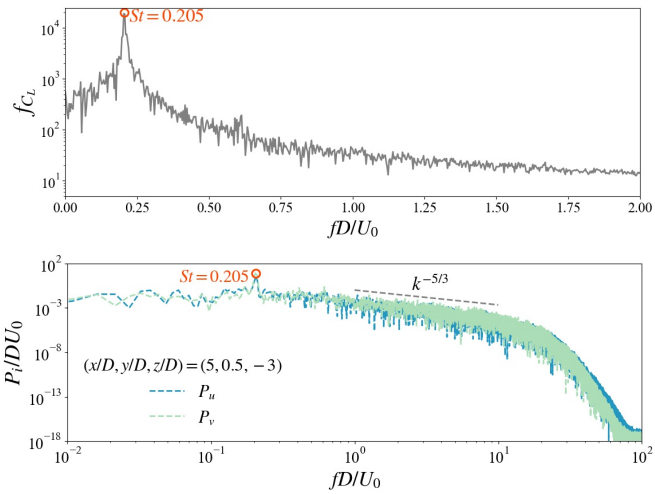

Figure 2.5: Top: frequency components at $Re = 3900$ measured from lift force via FFT. Bottom: power spectral density of streamwise/crossflow velocity components at a sampling point. The -5/3 scaling law is often added in spectral analysis, despite of its applicability for HIT.

force or velocity signal at sampling point in the near wake, for instance of $Re = 3900$ case shown in Figure 2.5. The root-mean-square of lift coefficient $C_{L,rms}$ principally can also be a candidate. However, one should note that it is quite sensitive as a result of being heavily influenced by intermittent dislocation, spanwise length and sampling time window. Time-averaged C_D and St work sufficiently for validation purposes to assure a fully-developed flow field at transitional and turbulent regimes. Boundary conditions imposed in present simulations can be found in paper collection.

Here, the turbulent case is presented as a demonstration of such complex wake flow resolved by preceding numerical algorithms. Figure 2.6(a) visualizes an instantaneous wake topology of the properly developed turbulent flow, wherein the finest scale with high enstrophy in recirculation region are well-resolved. Unlike the transitional wake, those large bulky vortex tubes are barely existent at turbulent flows. A spatial periodicity is perceptually observed from the velocity contour in crossflow direction at centerplane $y = 0$ in Figure 2.6(b). Figure 2.6(c) depicts the distributions of instantaneous and mean spanwise velocity at one (y, z)-plane, in which a visible variation of $\bar{w}$ can still be observed in spite of the damped intensity by time averaging. In Figure 2.7, the variation of mean velocity components in Z-direction is insignificant in contrast with instantaneous counterparts.

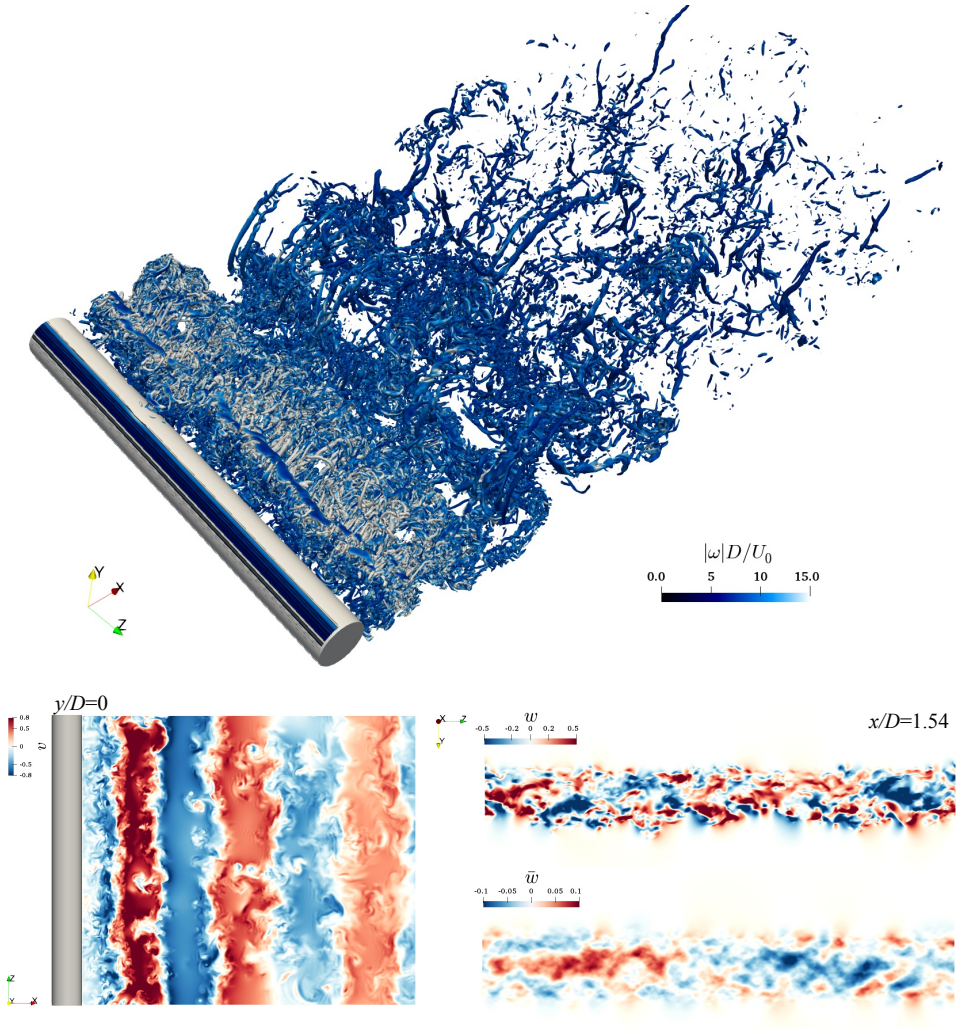

Figure 2.6: Instantaneous wake topology represented by iso-surfaces of $\lambda_2 = -12$ color-coded by vorticity magnitude $|\boldsymbol{\omega}|$. A close-up view of finer vortices in the near wake can be well observed in centerplane $y = 0$ (bottom left). A comparison of instantaneous (w) and mean ($\bar{w}$) spanwise velocity is given at a (y, z)-plane in recirculation region.

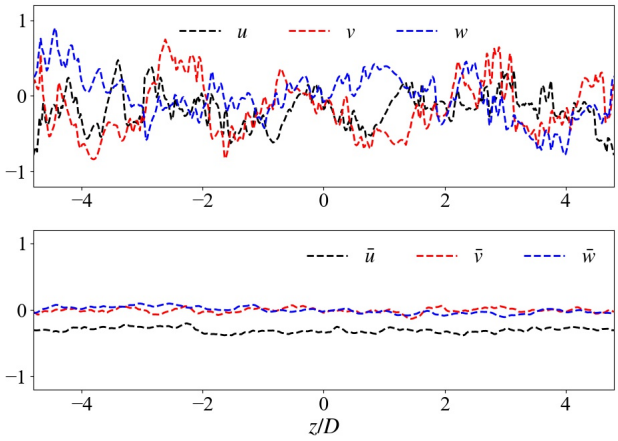

Figure 2.7: Variations in spanwise of instantaneous (upper) and mean (low) velocity of all three components at centerline $(x/D, y/D) = (1.54, 0)$.

Spanwise direction is commonly considered as homogeneous in terms of mean flow quantities, from a statistical view.

Particle phase

Once the single-phase flow has been fully established, particles are seeded from the central part of inlet surface, where vortices are still influential to the boundaries[18]. M-R equation (2.6) is thereafter solved simultaneously with the N-S equation with the same time step Δt. Particle-wall collision model is defined by a kinetic reduction of tangential and normal components.

The particle velocity $\boldsymbol{u}_p$ is time marched by an adaptive fourth-order Rosenbrock-Wanner scheme with a third-order error estimator (Hairer and Wanner 1990). For small Stokes numbers, viscous force becomes a stiff term, which requires critical small time step by explicit scheme and solving a series of non-linear equations by implicit scheme. A hybrid of explicit and implicit form was implemented to reduce the computational cost (see detailed formulation in Gobert (2010)). The particle position $\boldsymbol{x}_p$ is updated by explicit Euler scheme. The local fluid velocity $\boldsymbol{u}_{f@p}$ is linearly interpolated in each direction, for which a high-order scheme is believed to be unnecessary since the overall spatial accuracy is limited by the second-order FVM. Nevertheless, a verification is provided in the following section 2.5.

[18] A flexible seeding approach has been updated in *MGLET* recently that enables to select the domain of interest to inject particles instead of the whole computational domain.

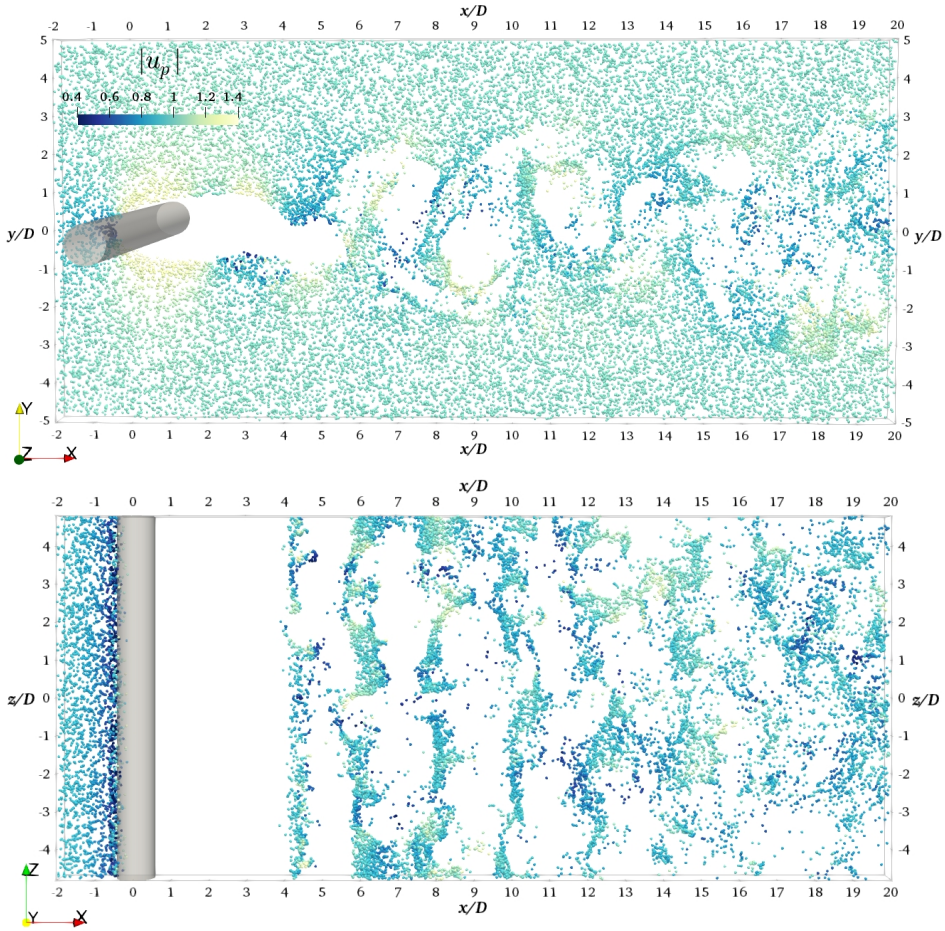

Figure 2.8: Instantaneous distribution of $Sk = 1$ particles within a $0.8D$-thickness slice from a vertical view at $z/D = \pm 0.4$ (top) and a horizontal view at $y/D = \pm 0.4$ (bottom), color-coded by particle velocity magnitude $|\boldsymbol{u}_p|$. A visual comparison of different clustering topologies in two directions is presented.

Figure 2.8 presents the topologies of dissected particle distributions from two views, of which $Sk = 1$ particles are selected within a range of $0.8D$ in Z/Y-direction. The distribution of particle velocity indicates the acceleration and deceleration processes for individual particles along their history paths, as a consequence of constant involvement with local vortices. The depleted regions (voids) and local clusters manifest the preferential concentration subjected to the centrifugal mechanism.

2.5 Verification of conditioned fluid velocity

In this section, we aim to demonstrate that the linearly interpolated local fluid velocity $\boldsymbol{u}_{f@p}$ seen at the particle position $\boldsymbol{x}_p$ is sufficiently accurate. A low-order scheme generally indeed is uncertain to support a trustworthy numerical result. However, the discretization by second-order finite volume method in present solver *MGLET* constrains the spatial resolution all over the computational domain at 2nd-order accuracy. It is thus theoretically reasonable to use a linear scheme to interpolate at scattered spatial point, i.e. particle position. One should also be aware that the numerical accuracy, first and foremost, heavily depends on mesh resolution, as the basis of interpolation stencil. Bearing this in mind, the effect of mesh resolution should be taken into account to evaluate the significance of interpolation scheme.

Two evaluation processes are implemented in the following verification, i.e. errors along particle trajectory and effects on clustering pattern. By doing so, we track inertial particles in a 2D steady Taylor-Green vortex (TGV) by using the linear and cubic schemes to obtain $\boldsymbol{u}_{f@p}(\boldsymbol{x}_p, t)$. The analytical solution of such 2D frozen flow field

$$\begin{aligned} u &= U_0 sin(x) * cos(y) \\ v &= -U_0 cos(x) * sin(y) \\ \omega_z &= 2U_0 * sin(x) * sin(y) \end{aligned} \tag{2.7}$$

enables a computationally cheap verification and a reliable evaluation of simulated results. Herein, reference velocity U_0 is unity and (x, y) is uniform mesh point in a periodic square domain of size $L_x = L_y = 2\pi$. Two pairs of Taylor-Green rollers display in Figure 2.9 where one TGV size is roughly π. The flow time scale is defined as $\tau_f = L_{x(y)}/U_0 = 2\pi$ and mesh resolution Δ is estimated as $2\pi/N$ (N the number of equidistant grid points in either direction). A simplified Maxey-Riley approximation for heavy particles is implemented to sufficiently serve the verification purpose.

$$\mathrm{d}\boldsymbol{u}_p/\mathrm{d}t = 1/Sk(\boldsymbol{u}_{f@p} - \boldsymbol{u}_p), \quad \mathrm{d}\boldsymbol{x}_p/\mathrm{d}t = \boldsymbol{u}_p \tag{2.8}$$

We separate the procedure into two parts to examine the effect of interpolation accuracy on both **particle trajectory** and **clustering pattern**.

Part I: Errors along particle trajectory

The workflow in present TGV-flow test is as follows:
i) A discrete flow field (u, v) at the grid points (x, y) is exactly given by the aforesaid analytical formulas. The flow field is steady and no need of time advancing.
ii) $(u, v)_{f@p}$ is computed by either linear and 3rd-order scheme using the discrete flow field obtained in step i).
iii) The interpolated $(u, v)_{f@p}$ from step ii) is compared with the exact analytical velocity at $(x, y)_p$ to measure the interpolation error, i.e. $\varepsilon = u_{interp} - u_{analy}$.
iv) The new particle velocity $(u, v)_p$ and position $(x, y)_p$ are obtained from MR equation using a hybrid Adams/BDF scheme with adaptive time stepping. The conditioned fluid velocity $(u, v)_{f@p}$ is taken as the interpolated value from step ii).
v) Go back to ii) to interpolate the fluid velocity at the new particle position from step iv).
Four particles at $Sk = 0.005, 1, 5, 10$ are released at a fixed position on an outside orbit with initial conditions $(u_0, v_0, x_0, y_0) = (0.5, 0.5, 0.7, 0.7)$. The simulation is terminated when inertial particles first hit arbitrary walls, where only $Sk = 1$ particle collides within the whole simulation period $t = 2.5\tau_f$, as shown in Figure 2.9. A similar expelling tendency can also be found in a more complex scenario (Fukada et al. 2018).

Figure 2.10 presents the interpolated fluid velocity components $(u, v)_{f@p}$ and the accompanying errors at $Sk = 1$ in six cases with different combinations of three mesh resolutions and two interpolation schemes. The size of a single Kármán cell is roughly $1D$, thus the equivalent uniform grid number is 25 at the second finest grid cell in our simulations. In TGV flow, $N = 50$ grid cells in each direction is correspondingly used to resolve a pair of rollers. We only observe the evident errors at a coarse mesh $N = 10$ using linear interpolation while the cubic scheme clearly reduces the errors (see the first column). In contrast, there is only little difference made by interpolation schemes at a higher resolution even at $N = 25$ case. We also can observe a clear improvement of accuracy as discretization gets finer, despite of using linear interpolation (see the first row). A similar observation is expected at $Sk = 5$ shown in Figure 2.11, where the errors at the coarsest mesh using linear interpolation seems even smaller than $Sk = 1$.

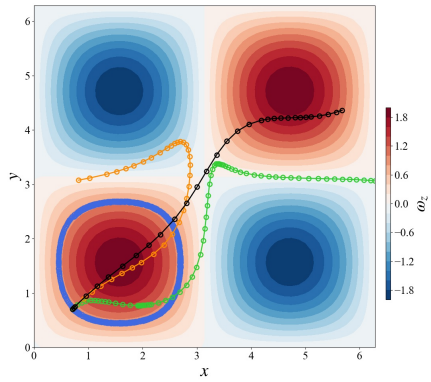

Figure 2.9: Two pairs of Taylor-Green rollers and particle trajectories in a 2D periodic domain (blue: $Sk = 0.005$, green: $Sk = 1$, orange: $Sk = 5$, black: $Sk = 10$).

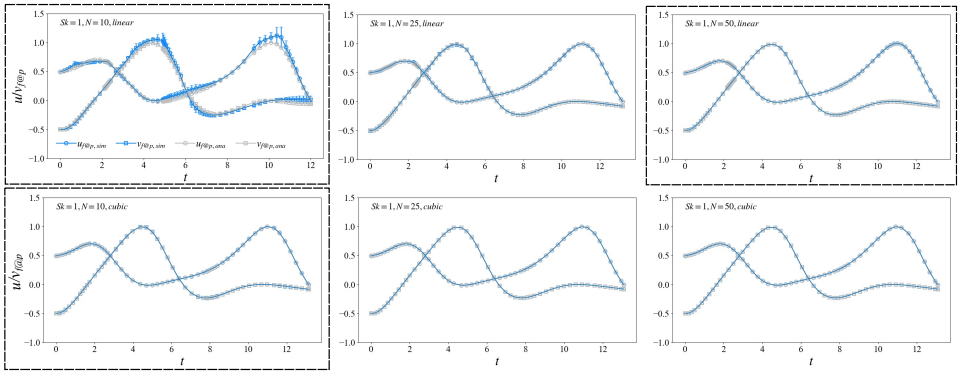

Figure 2.10: A comparison of interpolated and analytical local fluid velocity components accompanying by errors at $Sk = 1$ for six cases using different combination of interpolation schemes and mesh grid numbers.

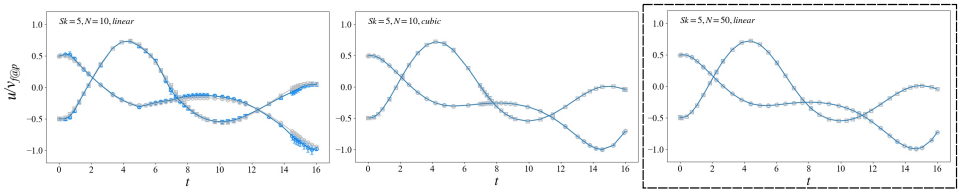

Figure 2.11: Same above at $Sk = 5$.

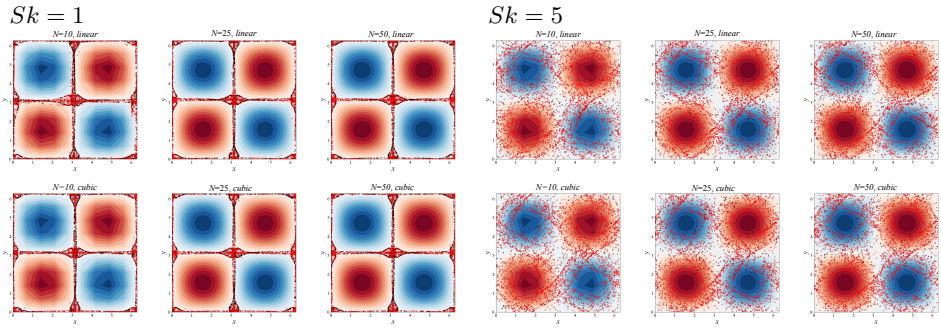

Figure 2.12: A comparison of instantaneous particle clustering corresponding to the above-stated six cases at $Sk = 1$ (left) and $Sk = 5$ (right).

Part II: Effect on clustering

In this part, we also want to examine the effect of interpolation errors on particle clustering pattern. A total number of 4000 particles are randomly seeded into the periodic domain and the simulation runs for $5\tau_f$. The centrifugal ejection expels inertial particles from the core regions to certain extent, which results in quite different clustering topology. In Figure 2.12, a stronger inertial effect at $Sk = 1$ shapes a larger squarish voids towards the wall boundaries while $Sk = 5$ particles are prone to form a smaller centric 'diamond' void. The peculiar squarish clustering pattern at $Sk = 1$ was also reported by Samant et al. (2021), wherein a movie of time-evolving clustering is also consistent with our result shown in Figure 2.13. Most importantly, we barely observe evident difference of clustering pattern for all cases at both $Sk = 1$ and 5. It demonstrates a negligible effect on a group of particles' residence, induced by either interpolation scheme or mesh resolution.

An interpretation of interpolation error

As we solve the stripped-down M-R Eq.(2.8), the ideal solution of $\boldsymbol{u}_{f@p}$ is obtained exactly from the discrete velocity field at the grid nodes. However, a certain error ε always exists in the practical interpolation in the discrete field. Instead, the particle algorithm solves:

$$\mathrm{d}\boldsymbol{u}_p/\mathrm{d}t = 1/Sk(\boldsymbol{u}_{f@p,exa} + \varepsilon - \boldsymbol{u}_p) \tag{2.9}$$

where $\boldsymbol{u}_{f@p,exa}$ stands for exact fluid velocity at the particle position. We can reform the above equation in the same form as Eq.(2.8) by introducing

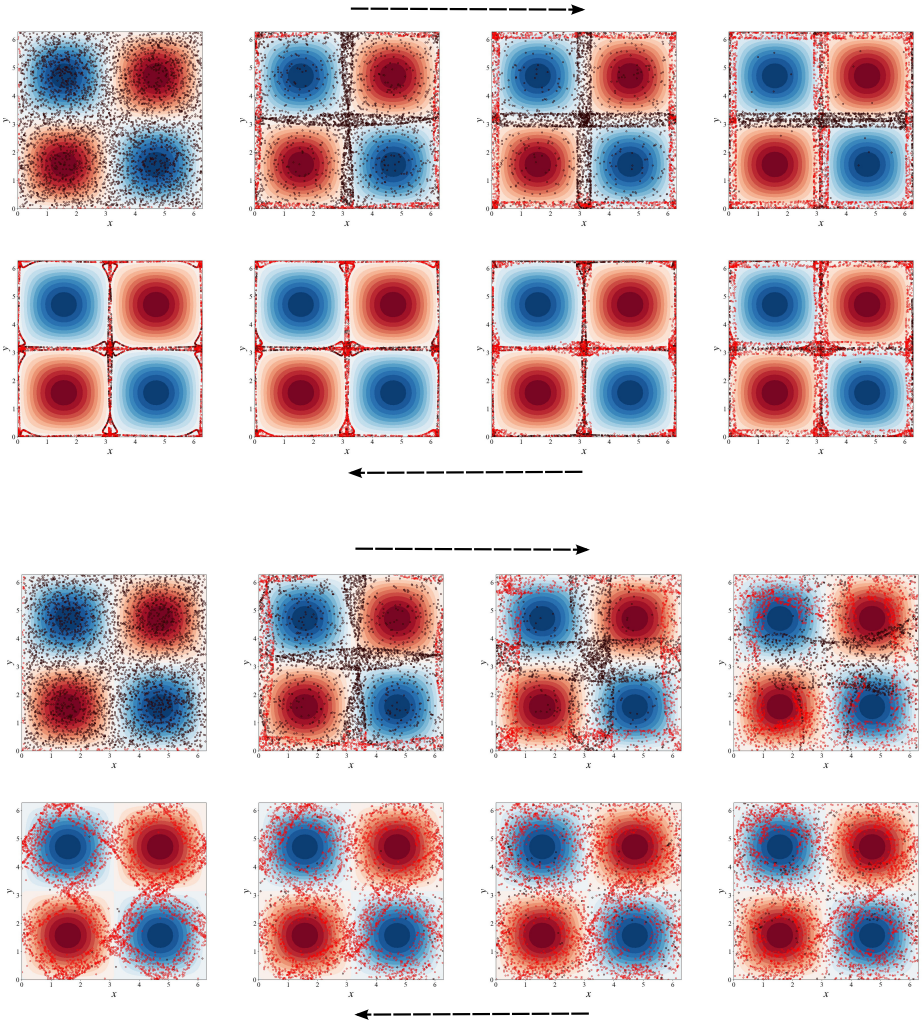

Figure 2.13: A time-sequence snapshot of clustering pattern evolving till a steady state. The total simulation time is $10\tau_f$. Upper: $Sk = 1$; Lower: $Sk = 5$.

a *modified* Stokes number Sk_+:

$$\mathrm{d}\boldsymbol{u}_p/\mathrm{d}t = 1/Sk_+(\boldsymbol{u}_{f@p,exa} - \boldsymbol{u}_p) \tag{2.10}$$

Doing so, the interpolation error ε can be interpreted as a modification of the Stokes number. If we believe the right-hand sides of Eqs. (2.9) and (2.10) are approximately equal, a further derivation shows that:

$$\frac{Sk_+}{Sk} = \frac{\boldsymbol{u}_{f@p,exa} - \boldsymbol{u}_p}{\boldsymbol{u}_{f@p,exa} + \varepsilon - \boldsymbol{u}_p} = \frac{1}{1+\varepsilon_r} \tag{2.11}$$

herein, $\varepsilon_r = \varepsilon/(\boldsymbol{u}_{f@p,exa} - \boldsymbol{u}_p)$ is the relative error. Assuming that $\varepsilon_r \ll 1$, we can apply Taylor series expansion to further obtain:

$$\frac{Sk_+}{Sk} \approx 1 - \varepsilon_r \tag{2.12}$$

Equation (2.12) indicates that the interpolation error has the similar effect as a modification of the nominal Stokes number Sk.

In an experimental practice, there inevitably exists a size distribution of the suspended particles around a mean value, thus a corresponding Sk-distribution around a mean Sk. The interpolation error ε in computational particle tracking varies in space, i.e. depending on the local smoothness of discrete flow field. The regions with large velocity gradient tend to generate large errors. Despite of the different interpretations, a Sk-distribution around a desired Sk in both situations are likely to result in a more indistinct clustering pattern than that the with single-Sk particles, or analogously, negligible interpolation errors.

As of now, we can conclude that the low accuracy of the linear interpolation can be compensated by using a finer mesh. If the mesh is sufficiently fine, the order of interpolation plays only a modest or perhaps negligible influence on the results of particle tracking and cluste ring. A higher-order interpolation is not so important in the laminar wake flow as in HIT since the vortex structures in the $Re = 200$ wake is relatively large and without sharp gradients.

2.6 Identification of particle clustering

The density inhomogeneity in particle field observed in Figure 2.8 needs to be quantified so as for a rigorous statistical analysis. A wide extension of measurements have been proposed and applied to characterize preferential concentration. The perceptive box-counting method (Fessler et al. 1994)

uses uniform boxes to measure the probability density function (PDF) at a given size, thereby leads to a bias due to the size choice. Two Lagrangian tracking-based methods, i.e. fractal correlation dimension (Bec et al. 2007, Tang et al. 1992) and radial distribution functions (RDF) (Bec 2003, Bragg and Collins 2014, Bragg et al. 2015a) can measure a global concentration tendency by space-averaging, particularly the later can provide a scale-by-scale analysis. The divergence of the particle velocity field (Bec et al. 2007, IJzermans et al. 2009) and dynamical finite-time Lyapunov exponents (FTLE) (Daitche and Tél 2014, Haller and Sapsis 2008, Sapsis and Haller 2009), are other alternatives to quantify concentrations. A detailed introduction of many other available approaches can be found in the review by Monchaux et al. (2012) for readers' interest.

The present work adopts a versatile technique, i.e. Voronoï diagram, to quantify the instantaneous clustering without *a priori*. The spatial resolution of decomposed field is self-adaptive/intrinsic based on the relative position of particle pairs. Given its computational efficiency and objectivity[19], Voronoï analysis has risen to a standard approach to characterize particle clustering. It perfectly serves our purpose to study individual clusters, which can not be detected by abovementioned spatial-averaged methods. A Voronoï tessellation is an ensemble of polyhedron cells, of which the connected vertices of adjacent cells form a continuous particle field. A sensitivity of the number of samples and the sampling regions should be considered to obtain a sample-independent result. A dependency analysis on particle numbers and subsets at $Re = 200$ is given at the end of this section. The standard deviation is commonly regarded as the indicator of clustering level.

A few recent work on extending Voronoï analysis should be mentioned here regardless of being investigated only in HIT. Oujia et al. (2020) tracked the volume change rate of the Voronoï volumes within a finite period. A non-trivial relation between particle divergence and local concentration has been reported, where divergence is most substantial in cluster regions but also in voids. Momenifar and Bragg (2020) thoroughly studied the parameter-dependence of clustering at different Voronoï-scales. Of particular attention is that authors reported the inconsistent tendency between PDF and standard deviation of Voronoï volumes. This observation is also found in thesis author's work 4.2 despite the carrier flow being quite different. It brought

[19]The calculation of Voronoï volumes with $N_p \sim O(10^5)$ is definitely manageable. Two Python libraries, i.e. Voronoï and ConvexHull, are called to calculate polygon area and polyhedron volume for 2D and 3D cases, respectively.

up the question of the objectivity for standard deviation to be counted as the only measure of clustering since it mainly reveals the contribution of large Voronoï volumes.

Provided with PDF of Voronoï volumes, the scale thresholds for clusters and voids can be defined by the corresponding normalized Voronoï of intersection points with either Poisson (Monchaux et al. 2010) or Gamma distribution (Tagawa et al. 2012)[20]. Despite being non-ambiguous, PDF-based criterion do not bear physical significance. In thesis author's article 4.2, the density distribution is found to be unreasonably biased given the PDF-derived thresholds. Therefore, a physics-based identification approach is proposed in this piece of work. The conditioned flow quantities on particle position, such as local Q-invariant, are associated with Voronoï volumes. Figure 2.14 compares the topology of 2D Voronoï diagram for tracer and inertial particles at (x, y)- and (x, z)-slice. The centrifugal ejection for inertial particles results in larger Voronoï volumes within vortex core-ish regions (b), while the smaller volumes are accompanied along the cusps of vortices (d). The well-mixed passive particles, by contrast, present a relatively even-size distribution of Voronoï cells (see (a)(c)). The sampled local Q-field at $Sk = 1$ by clustering can be taken as a subset of the one for tracers.

It is noteworthy that PDF- and physics-based criteria both have merits and limitations. For a general application, the usual PDF-based approach can be used to identify clusters and voids in such scenario where clustering is not characterized by preferential sampling of velocity gradient (e.g. Q-field) that is believed to reflect the small scales of flow field. For instance of particle settling, Tom and Bragg (2019) suggested that particles do strongly cluster at small scale of turbulence yet attributes to the reduced correlation time scale of the conditioned flow. The thresholds introduced by Monchaux et al. (2010), however, can quantify clustering in this case. In short, both methods should be accordingly and critically applied to explain the disparate mechanisms of particle clustering.

Voronoï analysis: Dependency on particle numbers and subsets

Principally, sufficient number of particles can improve the accuracy and possibility to detect a wide scale of local particle concentrations. Figure 2.15(a) shows the kernal density estimations (kdes) of the normalized Voronoï vol-

[20]Here, the only fitting parameter is the standard deviation of Voronoï volumes; a two-parameter distribution is also close fit with shape factor $k = 5$ and scale factor $b = 0.2$ (Ferenc and Néda 2007).

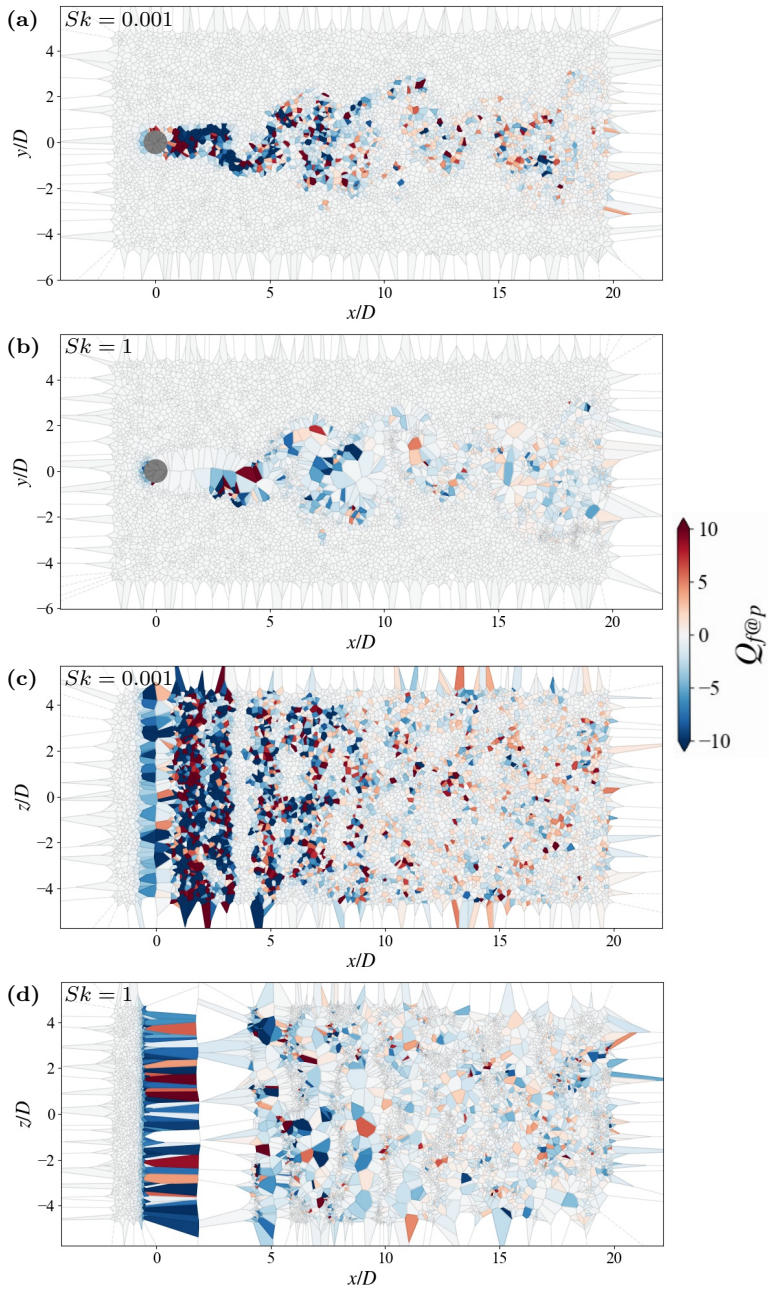

Figure 2.14: Examples of 2D Voronoï cell diagram for $Sk = 0.001$ and 1 particles, with the number of particles $6 \sim 7 \times 10^3$ projected onto (x, y)- and (x, z)-centerplane, color-coded by local Q-values. Clusters and voids at $Sk = 1$ are clearly more evident than $Sk = 0.001$, indicating a strong clustering.

umes calculated from the collection of particles within x/D=[-2, 41.6] spanning all over Y- and Z-direction at $Sk = 1$. Four cases $N_{pi}(i$=1-4) are considered as increasing the particle injection rate, of which the particle number N_{pi} for the first three cases increases proportionally while the last case is limited by computational cost. A denser set of samples creates both smaller and larger scales of Voronoï volumes, although cases N_{p1} and N_{p2} are comparably insufficient in contrast with cases N_{p3} and N_{p4}. The probability of identifying clusters notably increases, as also implied by an increasing standard deviation (std) of normalized Voronoï volumes $\mathcal{V}/\langle\mathcal{V}\rangle$. The increasing fraction of the clusters decreases the mean value $\langle\mathcal{V}\rangle$.

In addition, since the particle field of interest is truncated at x/D=22, one may question the dependency of subsamples in terms of the $\mathcal{V}$-scale and probability of Voronoï volumes. In Figure 2.15(b), we compare the kdes of three sample collections, of which case No2 is the subset of case No1. The discrepancy lies in the small scale of Voronoï volumes, where the probability for the subset is lower than that for the fullset. It is reasonable since the particles residing in more downstream wake are more mixed than in the near wake, therefore the exclusion of the downstream fraction at case No2 decreases the probability of small scales.

The scale of normalized Voronoï volumes for case No3 is narrower than the other two cases, which is likely to result from the less divergent relative size between larger and smaller Voronoï cells. Mean Voronoï volumes $\langle\mathcal{V}\rangle$ is nevertheless indistinct while the standard deviation for case no3 is noticeably smaller than the bother two cases. For the sake of a manageable data load and objective clustering identification, the combination of N_{p4} and No2 is sufficient as a data base of the Voronoï analysis. The intersection points are, however, independent of the truncation and portion, observed also in HIT (Baker et al. 2017).

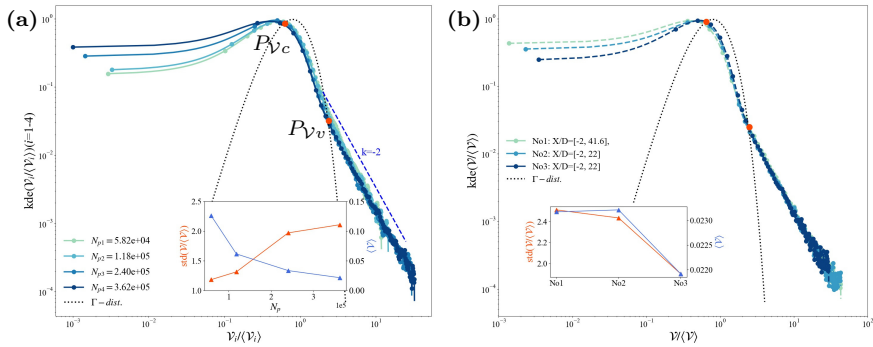

Figure 2.15: (a) Kernel density estimations (kdes) of the normalized Voronoï volumes with increasing particle numbers $N_{pi}(i$=1-4), superimposed by random Γ distribution. (b) kdes of Voronoï volumes calculated based on three sets of samples. Case No1 represents the fullset (x/D=[-2, 41.6]) identical to case N_{p4} in (a). Case No2 is the subset of case No1 and the samples are truncated at x/D=22. Voronoï volumes in case No3 are calculated from the selective particles within x/D=[-2, 22].

Simplicity is the final achievement. After one has played a vast quantity of notes and more notes, it is simplicity that emerges as the crowning reward of art.

— *Fryderyk Chopin*

3 Overview of the articles

The main contributions to the present dissertation, to this point, include six manuscripts with a weighty emphasis on preferential concentration in circular cylinder wake flow. Of all manuscripts, the first five all addressed particle clustering in different flow regimes and configurations. The last one is a side product of the fourth paper, concerning the relationship between oblique shedding and natural vortex dislocation in the single-phase transitional wake flow. A brief description of the systematic work is listed in this chapter.

3.1 List of papers

Article I

On simulation of particle-laden wake flow
Zhaoyu Shi, Fengjian Jiang, Håkon Strandenes, Lihao Zhao, Helge I. Andersson

Published in MekIT'19: 10th National Conference on Computational Mechanics; 2019, Trondheim, Norway. Ed. by Skallerud, Bjørn and Andersson, Helge, I., pp. 407-418.

Authors' contribution: The initial intention for this piece of work carried out by Zhaoyu Shi is a test of *MGLET*. Since the 2D laminar cylinder wake

is economical to achieve even integrated with the computation of particle movement, the results output by *MGLET* can be well compared and thus verified. In addition to the consistent particle distributions, we observed some interesting phenomenon from these preliminary results that were also found in other literature yet somehow overlooked. The subsequent two journal papers were inspired from here. In this beginning period, Fengjian Jiang and Håkon Strandenes provided the very helpful *MGLET* training and guidance.

Article II

Bow shock clustering in particle-laden wetted cylinder flow
Zhaoyu Shi, Fengjian Jiang, Lihao Zhao, Helge I. Andersson
Published in International Journal of Multiphase Flow 130, 103332, 2020

Authors' contribution: Zhaoyu Shi performed the supplementary simulations to further investigate the peculiar phenomenon observed in the vicinity of the cylinder. Helge I. Andersson initiated this topic for an in-detail study by mean of Voronoï diagram. Zhaoyu Shi conducted the programming for post-processing, analysis, visualisation and wrote this paper. Fengjian Jiang and Lihao Zhao came up with many useful discussions and contributed to the internal review. Helge I. Andersson supervised and evaluated the manuscript.

Article III

Clusters and coherent voids in particle-laden wake flow
Zhaoyu Shi, Fengjian Jiang, Lihao Zhao, Helge I. Andersson
Published in International Journal of Multiphase Flow 141, 103678, 2021

Authors' contribution: Zhaoyu Shi used the same dataset with the last published paper, yet focused on addressing the preferential concentration in the near wake. We chose to separate the observations so as to better report the detailed observations and mechanisms. The analysis, visualisation and paper writing were completed by Zhaoyu Shi, during which other authors provided valuable suggestions and revised the manuscript.

Article IV

Scale-dependent particle clustering in transitional wake flow
Zhaoyu Shi, Fengjian Jiang, Lihao Zhao, Helge I. Andersson

Submitted to Journal of Fluid Mechanics (2021), some revisions made after submission.

Authors' contribution: Zhaoyu Shi carried out the simulations and verified the sufficiency of the interpolation scheme used in *MGLET* (see section 2.5). This work has been finished during the last PhD phase as the most important finding by far. The first author conducted the post-processing, statistical analysis, visualisation and prepared the paper draft. The manuscript was modified mainly by Helge I. Andersson and Fengjian Jiang. The discussions with Lihao Zhao are much appreciated. It is currently under the second review.

Article V

Particle concentration in turbulent cylinder wake flow
Zhaoyu Shi, Fengjian Jiang, Lihao Zhao, Helge I. Andersson
Under consideration for publication in Physical Review Fluids

Authors' contribution: Zhaoyu Shi performed the DNSs of the particle-laden turbulent flows at benchmarking $Re = 3900$. The draft of the manuscript has been made but some analysis need to be evaluated furthermore. Some new ideas on statistical turbulence analysis are inspired by the recent reviewer's comments for Article IV.

Article VI

The role of natural vortex dislocation in oblique shedding with mode A instability
Cai Tian, Zhaoyu Shi, Fengjian Jiang, Helge I. Andersson
Under consideration for publication in Physics of Fluids Letter

Authors' contribution: This work is irrelevant to particle but stimulated from the interesting observation in the single-phase simulations for Article IV. The present investigation was initiated by Zhaoyu Shi based on the available dataset. The first author further performed supplementary simulations, analysis and wrote this letter. The process was mainly supervised by Cai Tian and Zhaoyu Shi. Fengjian and Helge discussed on many occasions.

3.2 Summary of papers

Paper I

This work was motivated by previous numerical observations of particle dis-

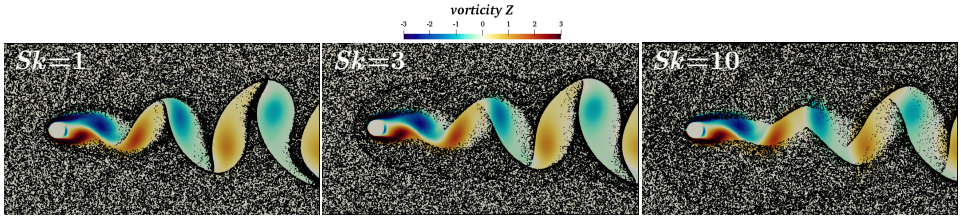

Figure 3.1: Instantaneous particle distribution at Sk=1, 3 and 10, superimposed by the contour of spanwise vorticity.

tributions in 2D unsteady laminar Kármán vortex street at $Re = 100$. We performed the simulations by means of the solver *MGLET* as a validation of its implemented particle library. This work presents the overall qualitative description of how local vortices influence inertial particle's fate at one snapshot by centrifugal ejection (see Figure 3.1). The tracer-like particles are observed to be well-mixed in the near wake while inertial particles are swept away from the vortex cores towards the outer bounds at low vorticity. The ejection process forms the voids encompassing each local Kármán roller. Another striking observation is the appearance of a thin-layer aggregation originated from the front-end of cylinder and extends downstream. The topology of particle clustering in either the vicinity of the cylinder or vortex-shedding regions, clearly shows a Sk-dependency. These interesting preliminary visual results deserve separate attentions to explore, which are summarized in Paper II and III.

Part II

In this paper, we focus on studying the formation of *bow shock clustering* originated from the front-side particle-cylinder impaction. First we deployed Voronoï diagram (see Figure 3.2(a)) to measure the topology of bow shock clusters in terms of width (w) and thickness (t) in the vicinity of cylinder. The increase of w and t is evident at low and medium Sk while less varied at high Sk especially at further streamwise positions to the cylinder. The shape at each Sk is found to be persistent without being affected by vortex shedding.

The bow shock clustering is explicitly aroused by the deceleration process due to particle-cylinder collision. In addition to the collision mechanism, we tend to explore the role of laminar shear layer on the concentration. We first tracked a group of $Sk = 0.1$ particles in potential flow, where a convergence of trajectories near the *inflection point* (IP) of *streamlines* without hitting the cylinder so as to exclude the effect of a collision model. Bypassing the

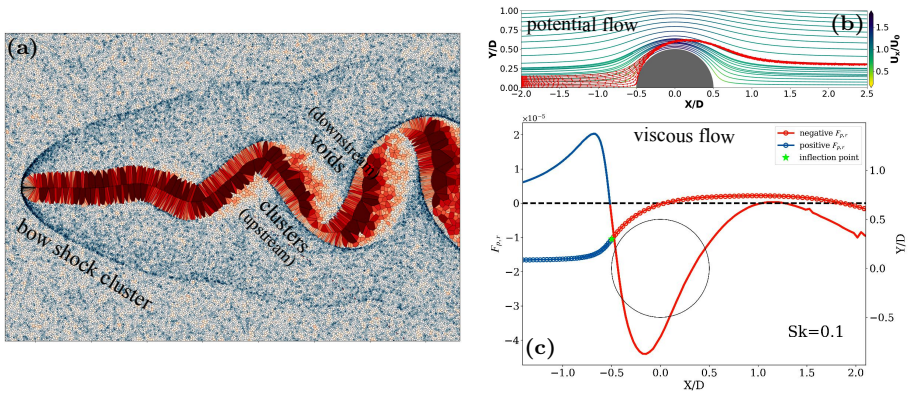

Figure 3.2: (a) An illustration of 2D Voronoï diagram; a clear bow shock cluster is detected and convected downstream. (b) The trajectories of a group of $Sk = 0.1$ particles seeded into the potential flow past a cylinder, superimposed with the streamlines. (c) Particle trajectory at $Sk = 0.1$ and the corresponding radial component of viscous drag force $F_{r,p}$. The direction-change point from $+F_{r,p}$ to $-F_{r,p}$ approximates IP of trajectory (marked by a green star).

IP, the trajectories start to depart from streamlines but are clustered within a thin layer (see Figure 3.2(b)). Inspired by this finding, we also tracked a $Sk = 0.1$ particle in our simulated viscous flow, where the streamlines are similar with potential flow in the lee side of the cylinder. The pressure force is believed to be dominant than viscous flow on a fluid particle at $Re = 100$ so as to counter balance the centrifugal force. A trajectory of $Sk = 0.1$ particle resembles a streamline of fluid element. The real physical force, i.e. the radial component of viscous Stokes drag force, balances the opposite-direction centrifugal force which depletes inertial particle from vortical flow structures. The direction-alteration of radial force from outwards to inwards at IP of particle *trajectory* indicates a focusing effect. Thereby, we can propose that the bow shock formation is likely to associate with convergence of particle trajectories by centrifugal mechanism. The less curved trajectories at higher Sk can be interpreted as the insufficient viscous drag force to attenuate the larger centrifugal effect, which results in a wider bow shock cluster.

Part III

As a sequel of Paper II, we switch the focus on investigating the clustering topology and the causal mechanism in the vortex shedding regions. The inertial particles at $Sk = 1$ are expelled towards the circumference of each Kámán cell thus emerging *coherent voids*. An interesting observation is

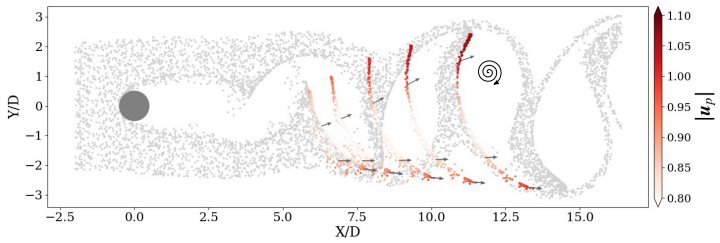

Figure 3.3: Backtraces of the $Sk = 1$ particles that compose the smooth edge of the void encompassing the clockwise rotating local vortex. The backtracked particles are colored by their velocity magnitude.

that the particles aggregating at the upstream side of each void form a *smooth edge* while the particles at the other side are more dispersed from the downstream edge. As reflected in Figure 3.2(a) by Voronoï diagram, the thin needle-shaped cells represent the smoothness and the polygon cells indicate the dispersion. We tend to explore how such pattern forms as particles encountering the local vortices.

First of all, by tracking the particles residing at one smooth edge backward in one shedding period (see Figure 3.3), we found the present edge originating from the earlier edge encompassing the vortex in same rotation. It suggests the coherence of these subsequent smooth edges. A non-monotonic velocity variation along one smooth edge indicates a substantial deceleration process in the middle part of the smooth edge. The vertical translation requires a larger velocity with the aid of Kámán rollers. This finding further drives us to examine the velocity variation along the individual trajectories, shown in Figure 3.4.

The continuous trajectories of particles ejecting from the opposite sides of the cylinder eventually settle in two sides of the same void (see panel (a) in Figure 3.4). The evidently lower velocity magnitude of particles making up the smooth edge reflects the different dynamics from those originating oppositely affected by the same vortices. Particularly shown in panel (b), we observe the substantial deceleration starting around the first detached shear layer for all particles corresponding to the smooth coherent clusters. The particles have trajectories deflected by a vortex cell shed from the other side. We therefore propose the *path history effect* collected along the trajectories. This study indicates a consideration of the objectivity of aerosol-type experimental visualization due to the integrated effects of particle inertia and path memory.

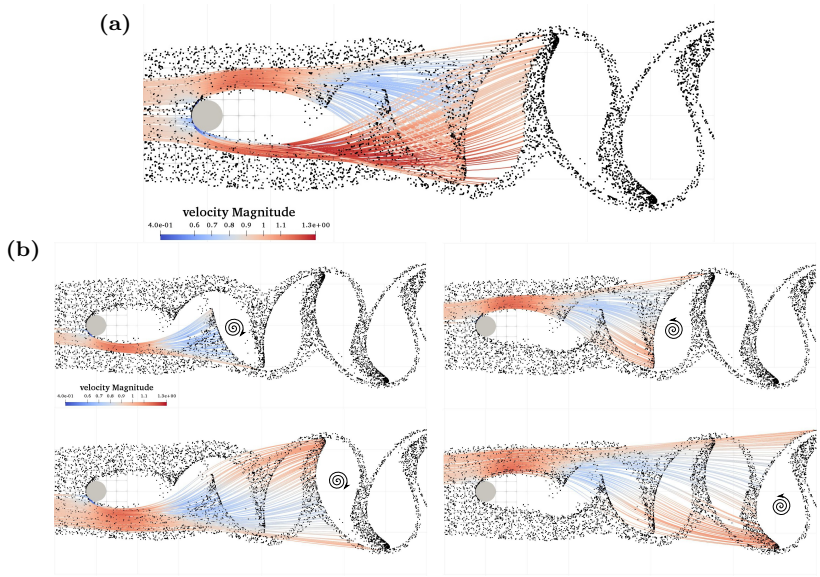

Figure 3.4: Panel (a): Trajectories of particles landing on smooth (upstream) and blurred (downstream) edges of one void at the last timestep (t^*). Panel (b): Trajectories of particles settling in each upstream smooth edge of each coherent void at t^*. Color represents instantaneous velocity magnitude along trajectories.

To this point, it is worth noting that the neglected inter-particle collision at present study is, however, likely to play a prominent role as mass loading is larger. We may expect a modification of such peculiar clustering patterns both reported in Paper II and III with the inclusion of particle-particle collision.

Part IV

The transition-in-wake gives rise to the streamwise vortical braids induced by mode A instability at the presence of three-dimensionality. We performed one-way coupled Eulerian-Lagrangian numerical simulations at $Re = 200$ with $O(10^5)$ number of particles seeded in to the domain of interest in the near wake. We investigated the role of streamwise vortices on particle dynamics and preferential concentration by two approaches: volume-averaged and in-plane analysis.

In the first part, we continue to use 3D Voronoï volumes to statistically study the Sk-dependency of the scales of clusters and voids. The distinct Sk-effect is observed at cluster scale in kernal density estimation of the normalized Voronoï volume ($\mathcal{V}/\langle\mathcal{V}\rangle$) while the voids exhibit self-similarity.

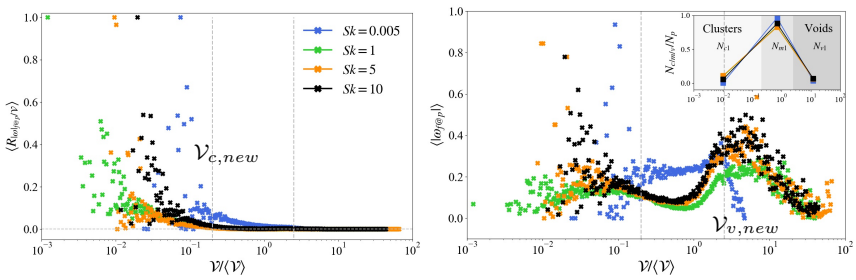

Figure 3.5: Voronoï-bin-averages $\langle\cdot\rangle$ versus normalized Voronoï volumes $\mathcal{V}/\langle\mathcal{V}\rangle$. Left: correlation between the conditioned vorticity magnitude $|\omega_{f@p}|$ and reciprocal of Voronoï volume, $R_{|\omega|/\mathcal{V}}$. Right: mean local vorticity magnitude, $\langle|\omega_{f@p}|\rangle$. Two vertical lines denote new thresholds for clusters $\mathcal{V}_{c,new} \approx 0.2 < \mathcal{V}_{c,old} \approx 0.6$ and voids $\mathcal{V}_{v,new} \approx \mathcal{V}_{c,old} \approx 2.5$.

The association of local flow quantities and Voronoï volumes indicates the preferential concentration in low-vorticity/high-strain regions subjected to the centrifugal mechanism. Additionally, the space-averaged variations of conditioned flow quantities and the corresponding correlation with $\mathcal{V}$ suggest a physics-based identification criterion of clusters and voids; see Figure 3.5 for instance of local vorticity magnitude. We compared the new thresholds with the traditional PDF-based ones, of which the cluster scale is evidently smaller whereas the void scale remains close. This finding is more prudent in present cylinder wake. One may note that the applicability of different criteria should be examined as other mechanisms taken account into the scenario. The variation of the joint distributions of local flow quantities and $\mathcal{V}$ is non-monotonic in Sk, where $Sk = 1$ presents the optimal clustering in the considered cases. Increasing Sk tends to inhibit the acceleration more than deceleration observed from the volume-averaged distribution of particle velocity.

The planar analysis in the second part, enables us to observe the disparate effects of Kármán rollers and streamwise-oriented braids on the topology of preferential concentration. As illustrated in Figure 3.6, the presence of streamwise vortices lead to some interesting clustering patterns, such as the *inner layer* concentration, *ribbon-clump* structure and the tubular void circles, which are non-existent in 2D laminar wake. The variation of slice-averaged particle velocity in spanwise direction indicates an attenuation of the streamwise vortices on particle dynamics.

Part V

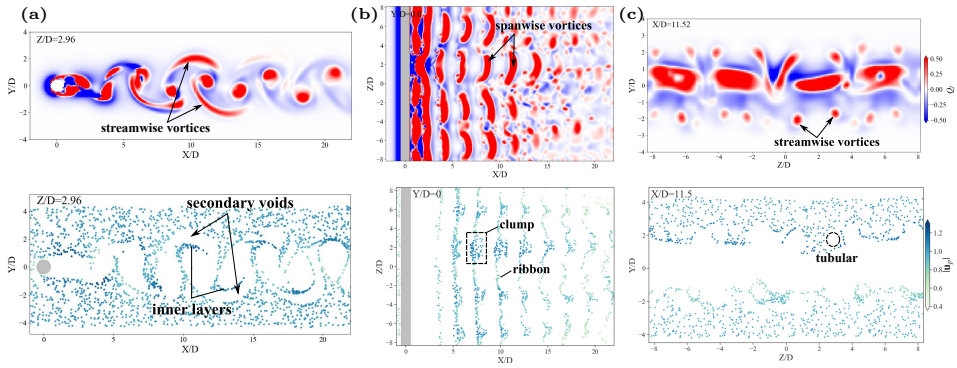

Figure 3.6: Planar Q-field (upper) versus topology of particle clustering in a $0.2D$ thick slice at a specific position in (a) streamwise X- (b) cross-section Y- (c) spanwise Z-direction. Particles are colored by their velocity magnitude.

As Re further increases, the transition to turbulence is firstly induced by the shear layer instability. We carried out the benchmarking $Re = 3900$ DNSs within the transition-to-turbulent regime. Four Sk cases from tracers to heavy particles are considered. The motivation is to statistically investigate how the presence of multi-scale vortices in the near wake modifies the preferential concentration. In volume-averaged analysis, the asymmetry of joint distribution of Voronoï volumes and local Q field (see Figure 3.7) generally indicates the strength of preferential sampling by centrifugal ejection. The weak asymmetry at $Sk = 1$, in contrast with the notably asymmetry at $Re = 200$, is likely to imply another physical mechanism other than the leading centrifugal mechanism in turbulent wake. A plausible conjecture is that the finer scales dominant by velocity gradients perhaps bring an impact on clustering. A coarse-graining approach filtered at appropriate scales will be applied later to discover the role of smaller scales via a scale-by-scale analysis. The smaller physics-based threshold for void manifests the effect of small scales, which seems to enhance the particle mixing in the vortex shedding regions.

The minor variation of mean particle velocity and acceleration in spanwise direction suggests a statistical homogeneity in the turbulent wake. In streamwise (see Figure 3.8), the spatial periodicity of mean particle velocity in streamwise component $\langle u_p \rangle$ is half than that in cross-section direction $\langle v_p \rangle$. An interesting observation is that the well-overlapped $\langle v_p \rangle$-variation for tracers and medium inertial particles. The collapse can be explained by introducing the vorticity-based effective Stokes number $Sk_e = \tau_p/\tau_{fe} = |\boldsymbol{\omega}|\tau_f$. The inertial effect characterized by Sk_e decreases as vorticity strength

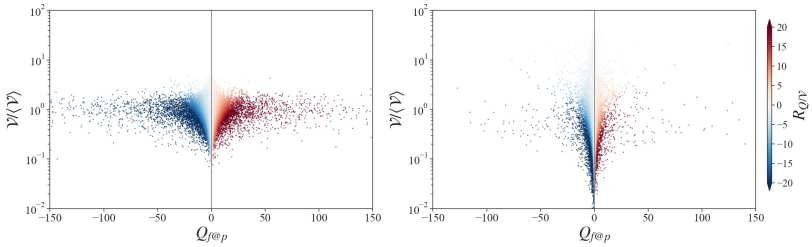

Figure 3.7: Jointplots of normalized Voronoï volumes $\mathcal{V}/\langle\mathcal{V}\rangle$ versus conditioned Q-field on particle position $Q_{f@p}$, color-coded by the correlation $R_{Q/\mathcal{V}} = \langle\mathcal{V}\rangle Q_{f@p}/\mathcal{V}$. Left: $Sk = 0.001$ Right: $Sk = 1$.

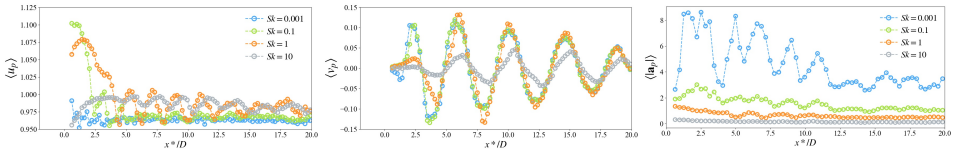

Figure 3.8: The variations in X-direction of the slice-averaged particle velocity of streamwise component (left); cross-sectional component (middle); particle acceleration magnitude (right).

decays downstream, thus resulting in the negligible discrepancy. In contrast, the inertial effect at $Sk = 10$ is still influential that a phase difference is observed at both $\langle u_p\rangle$- and $\langle v_p\rangle$-variation. In crossflow direction, the mean streamwise velocity deficit monotonically decreases with increasing Sk while the cross-section mean velocity decreases as further away from the mid-plane except at $Sk = 10$. Two peaks of mean acceleration about the mid-plane are displayed for inertial particles, despite that the variation amplitude is also insignificant. The mean acceleration variation for inertial particles, however, are less significant than mean velocity. A monotonically decrease in particle acceleration magnitude is observed as particles become more inertial.

Part VI

This additional work was motivated by the appearance of oblique shedding with mode A instability, as a by-product of particle-laden simulations in Paper IV. A further investigation on the causality with natural vortex dislocation was reported in this paper, with an emphasis of the dislocation topology. Two major types were identified, i.e. one-side and two-side dislocation, of which each presents two sub-types. The process of vortex dislocation can be divided into three vortex cells corresponding to the upper (U), middle (M) and lower (L) flow regions along spanwise direction. A

detailed schematic presentation and λ_2-isosurface of vortex loops can refer to Figures 1-4 in Paper VI.

Despite of the difference on topology, the physical mechanism responsible for their formation was discovered to be the increased phase difference between the dislocated vortex cells. The lower shedding frequency in M-cell results in the phase difference for both parent dislocations. What separates the one-side from two-side type was found to be the evident initial phase difference due to the unsynchronized variation of shedding frequency in U-, M- and L-cells. To the best of our knowledge, the topological characterization of natural vortex dislocations are barely covered in-detail.

If you thought that science was certain – well, that is just an error on your part.

— Richard P. Feynman

4

Conclusions and Outlook

4.1 Concluding remarks

This thesis has presented a systematic computational study of particle clustering in circular cylinder wake flow, spanning three major flow regimes. The intent of all included work is mainly to contribute useful physical characterizations and understandings to this important particle problem. Despite of the simplicity of point particle model and one-way coupling approach, the complex vortex structures give rise to many interesting phenomena of clustering. Only the tip of an iceberg was displayed here.

The starting point of investigating the particle-laden cylinder wake flow is the paradigmatic Kármán cells at 2D unsteady laminar regime. Some striking clustering observations, such as bow shock clusters, coherent smooth concentrations and voids, were reported in detail. The centrifugal expelling plays a prominent role as particles encountering the shed vortices in the near wake. Other relevant mechanisms were also found at play to account for those particular clustering patterns, for instance of the inflection point of radial force and path history effect collected along individual trajectories.

As Reynolds number increases, the transition to 3D wake with mode A instability induces the streamwise vortical braids. The presence of the secondary vortices shape the interesting clustering topology. An overall attenuation

on particle velocity by both Kármán rollers and streamwise vortices. The increase on Sk suppresses particle acceleration to a larger extent than deceleration. In the volume-averaged Voronoï analysis, the PDF-based thresholds for clusters and voids expose a statistical drawback in present vortical flow, where inertial particles are preferentially sampled by velocity gradient field. The new physics-based thresholds are proposed in association with local flow quantities. The in-plane averaged velocity variations present the spatial periodicity and the reduction of particle dynamics by streamwise vortices. All statistical analysis is consistent in the non-monotonic variation in Sk and the optimal preferential concentration at $Sk = 1$.

The presence of turbulence complexes the wake flow as the smaller scales come into play. The clustering topology is expected to be different from the ones formed in the wake dominant by large-scale vortices (i.e. rollers). The asymmetry of joint distribution of Voronoï scale and local Q is much weaker compared with that at transitional wake. It indicates another mechanisms co-existent yet unknown. We expect that the coarse grained flow quantities filtered at proper scales could provide some clues. It is plausible to believe that the small-scale vortices that dominantly contribute the velocity gradients are at play. This part of investigation will be complete in the final manuscript. The current statistics present some concrete characterizations of preferential concentration in the presence of turbulence, but the exploration of the responsible mechanism is still ongoing.

4.2 Future outlook

In the journey of exploring the conducted research in this doctoral dissertation, the constraints by current numerical tool or particle model are fully aware. Nevertheless, those existent obstacles motivate the further development on the current DNS solver and modeling, which can greatly extend the research scope and prompt the possibilities in many directions. Some new ideas are stimulated from reviewers' constructive comments on our available output.

Short-term objectives:

1) **particle settling**

The present thesis focused on the particle mixing and dispersion by excluding gravity force in M-R equation. In an experimental or real-life scenario, inertial particles inevitably deposit as entrained by coherent vortices. The inclusion of gravity effect, parameterized by Froude number (Fr), can give rise to the interesting phenomenon on particle settling. It is worth exploring

the particle clustering with the collective effects of preferential sampling by velocity gradient field and particle settling. A wall-mounted cylinder should replace the infinitely long one by imposing the no-slip boundary condition at the end wall. In turbulent wake, the hairpin/horseshoe vortices appearing at the boundary layer can be expected to result in interesting clustering topology. The particle settling has been investigated actively in pragmatic HIT and the relevant mechanisms have been scrutinized, such as preferential sweeping (Tom and Bragg 2019). There leaves an ample research gap to fill in such vortical wake flow at different transition regimes.

2) **parameter-dependency**
In present analysis of particle inertial effect, the Sk-effect is examined at a fixed density ratio $\rho_p/\rho_f = 10^3$, which essentially represents heavy particles. The role of density ratio and particle diameter embedded in Stokes number are also independent parameters to characterize particle inertia. The preferential concentration at various parameter combinations is worth being reported. The evaluation of other forces in M-R equation should be accordingly taken into consideration since a smaller density ratio may increase their significance.

3) **inflow condition**
The uniform incoming flow is an ideal condition to obtain the coherent vortex structures in the wake. A modification of inflow, such as enforcing oscillation or turbulence, makes the flow field better mimicking a more complex scenario. Previous studies (Aarnes et al. 2019) has studied the impact of turbulent incoming flow on particle-cylinder collision efficiency. We could be curious about its effect on particle clustering in the near wake since the presence of turbulence modifies the transition in wake. An oscillatory pressure force can bring the effect of free-surface wave into particle clustering.

Long-term goals:

1) **two-way coupling**
The present *MGLET* can only support one-way coupled simulations, despite that this thesis has provided some perspectives on this problem. The two-way coupled particle-laden simulations can certainly be expected to provide more interesting observations and better approximate the real-life particle-laden flows. The modulation of inertial particles on carrier flow, particularly turbulent statistics, is in particular important to explore. Liu et al. (2015) reported the modulation on representative mean velocity profiles but clearly more information could be further discovered. The interaction between

vortex structures and self-organized particle is perhaps a promising direction to embark on.

2) **inter-particle collision**
The significance of particle-particle collision is quite commonly asked in one-way coupled simulations as clusters are detected in a dilute suspension. One usually argue that the effect on clustering is minor as a $O(10^{-6})$ volume fraction can be guaranteed. As the mass loading increases, however, it could be interesting and necessary to investigate how the inter-particle collision modifies the clustering topology compared with the counterparts in the absence of this effect.

3) **experimental comparison**
A comparison with available experimental data is often a beneficial approach to examine the numerical results. However, the relevant experimental outcomes on similar cylinder wake flow suspended with inertial particles are indeed somehow lacking. It would be a contribution of this thesis to inspire more experimental insights particularly on this particle problem.

Bibliography

J. R. Aarnes, H. I. Andersson, and N.E.L. Haugen. Numerical investigation of free-stream turbulence effects on the transition-in-wake state of flow past a circular cylinder. *J. Turbul.*, 19:252–273, 2018.

J. R. Aarnes, N.E.L. Haugen, and H. I. Andersson. Inertial particle impaction on a cylinder in turbulent cross-flow at modest Reynolds numbers. *Int. J. Multiphase Flow*, 111:53–61, 2019.

M. Bagheri and M. Sabzpooshani. On the importance of the history force in dispersion of particles in von Kármán vortex street. *Adv. Powd. Tech.*, 31:3897–3909, 2020.

L. Baker, A. Frankel, A. Mani, and F. Coletti. Coherent clusters of inertial particles in homogeneous turbulence. *J. Fluid Mech.*, 833:364–398, 2017.

S. Balachandar. A scaling analysis for point-particle approaches to turbulent multiphase flows. *Int. J. Multiphase Flow*, 35:801–810, 2009.

S. Balachandar and P. Bagchi. Inertial and viscous forces on a rigid sphere in straining flows at moderate Reynolds numbers. *J. Fluid Mech.*, 481: 105–148, 2003.

S. Balachandar and J. K. Eaton. Turbulent dispersed multiphase flow. *Annu. Rev. Fluid Mech.*, 42:111–133, 2010.

J. Bec. Fractal clustering of inertial particles in random flows. *Phys. Fluids*, 15:L81, 2003.

J. Bec, L. Biferal, M. Cencini, A. Lanotte, S. Musacchio, and F. Toshi. Heavy particle concentration in turbulence at dissipative and inertial scales. *Phys. Rev. Lett.*, 98:084502, 2007.

G. Bellani and E. A. Variano. Slip velocity of large neutrally buoyant particles in turbulent flows. *New J. Phys.*, 14:125009, 2012.

I. J. Benczik, Z. Toroczkai, and T. Tél. Advection of finite-size particles in open flows. *Phys. Rev. E*, 67:036303, 2003.

T. Bhowmick, Y. Wang, M. Iovieno, G. Bagheri, and E. Bodenschatz. Population distribution in the wake of a sphere. *Symmetry*, 12:1498, 2020a.

T. Bhowmick, Y. Wang, M. Iovieno, G. Bagheri, and E. Bodenschatz. Supersaturation in the wake of a precipitating hydrometeor and its impact on aerosol activation. *Geophys. Res. Lett.*, 47:e2020GL091179, 2020b.

L. Bourouiba. The fluid dynamics of disease transmission. *Annu. Rev. Fluid Mech.*, 53:473–508, 2020.

A. D. Bragg and L. R. Collins. New insights from comparing statistical theories for inertial particles in turbulence. Part I: spatial distribution of particles. *New J. Phys.*, 16:055013, 2014.

A. D. Bragg, P. J. Ireland, and L. R. Collins. On the relationship between the non-local clustering mechanism and preferential concentration. *J. Fluid Mech.*, 780:327–343, 2015a.

A. D. Bragg, P. J. Ireland, and L. R. Collins. Mechanisms for the clustering of inertial particles in the inertial range of isotropic turbulence. *Phys. Rev. E*, 92:023029, 2015b.

L. Brandt and F. Coletti. Particle-laden turbulence: Progress and perspectives. *Annu. Rev. Fluid Mech.*, 54:159–189, 2022.

M. Burger, R. Schmehl, R. Koch, S. Wittig, and H.-J. Bauer. DNS of droplet-vortex interaction with a Kármán vortex street. *Int. J. Heat Fluid Flow*, 27:181–191, 2006.

T. J. Burns, R. W. Davis, and E. F. Moore. A perturbation study of particle dynamics in a plane wake flow. *J. Fluid Mech.*, 384:1–26, 1999.

T. Cai, F. Jiang, B. Pettersen, and H. I. Andersson. Vortex dislocation mechanisms in the near wake of a step cylinder. *J. Fluid Mech.*, 891:A24, 2020.

A. Chouippe, M. Krayer, M. Uhlmann, J. Dušek, A. Kiselev, and T. Leisner. Heat and water vapor transfer in the wake of a falling ice sphere and its implication for secondary ice formation in clouds. *New J. Phys.*, 21: 043043, 2019.

R. Cliff, J. Grace, and M. E. Weber. *Bubbles, Drops, and Particles.* Academic Press, New York, 1978.

S. W. Coleman and J. C. Vassilicos. A unified sweep-stick mechanism to explain particle clustering in two- and three-dimensional homogeneous, isotropic turbulence. *Phys. Fluids*, 21:113301, 2009.

A. Daitche. On the role of the history force for inertial particles in turbulence. *J. Fluid Mech.*, 782:567–593, 2015.

A. Daitche and T. Tél. Memory effects in chaotic advection of inertial particles. *New J. Phys.*, 16:073008, 2014.

S. Dong, G. Karniadakis, A. Ekmekci, and D. Rockwell. A combined direct numerical simulation-particle image velocimetry study of the turbulent near wake. *J.Fluid Mech.*, 569:185–207, 2006.

J. K. Eaton and J. R. Fessler. Preferential concentration of particles by turbulence. *Int. J. Multiphase Flow*, 20:169–209, 1994.

S. Elghobashi. On predicting particle-laden turbulent flows. *Appl. Sci. Res.*, 52:309–329, 1994.

S. Elgobashi. An updated classification map of particle-laden turbulent flows. In S. Balachandar and A. Prosperetti, editors, *IUTAM Symposium on Computational Approaches to Multiphase Flow*, pages 3–10, Dordrecht, 2006. Springer Netherlands. ISBN 978-1-4020-4977-4.

A. Espinosa-Gayosso, M. Ghisalberti, J. N. Ivey, and N. L. Jones. Particle capture by a circular cylinder in the vortex-shedding regime. *J. Fluid Mech.*, 733:171–188, 2013.

J. S. Ferenc and Z. Néda. On the size distribution of Poisson Voronoï cells. *Physica A*, 385:518–526, 2007.

J.H. Ferziger and M. Perîc. *Computational Methods for Fluid Dynamics.* Springer-Verlag Berlin Heidelberg, New York, 2002.

J. R. Fessler, J. D. Kulick, and J. K. Eaton. Preferential concentration of heavy particles in a turbulent channel flow. *Phys. Fluids*, 6:3742–3749, 1994.

T. Fukada, W. Fornari, L. Brandt, S. Takeuchi, and T. Kajishima. A numerical approach for particle-vortex interactions based on volume-averaged equations. *Int. J. Multiphase Flow*, 104:188–205, 2018.

C. Gobert. *Large Eddy Simulation of Particle-Laden Flow*. PhD dissertation, Technical University of Munich, 2010.

W. W. Grabowski and L. P. Wang. Growth of cloud droplets in a turbulent environment. *Annu. Rev. Fluid Mech.*, 45:293–324, 2013.

N. Gui, J. Yan, J. Fan, and K. Cen. A DNS study of the effect of particle feedback in a gas-solid three dimensional plane jet. *Fuel*, 106:51–60, 2013.

E. Hairer and G. Wanner. *Solving Ordinary Differential Equations II. Stiff and Differential-Algebraic Problems*. Springer, New York, 1990. ISBN 978-3-642-05221-7.

G. Haller and T. Sapsis. Where do inertial particles go in fluid flows? *Physica D*, 237:573–583, 2008.

N.E.L. Haugen and S. Kragset. Particle impaction on a cylinder in a cross-flow as function of Stokes and Reynolds numbers. *J. Fluid Mech.*, 661: 239–261, 2010.

H. Homann and J. Bec. Concentrations of inertial particles in the turbulent wake of an immobile sphere. *Phys. Fluids*, 27:053301, 2015.

H. Homann, T. Guillot, J. Bec, C. W. Ormel, S. Ida, and T. Tanga. Effect of turbulence on collisions of dust particles with planetesimals in protoplanetary disks. *Astron. Astrophys.*, 589:A129, 2016.

A. A. Hunt, J.C.R and Wray and P. Moin. Eddies, streams, and convergence zones in turbulent flows. In *Studying Turbulence Using Numerical Simulation Databases, 2. Proceedings of the 1988 Summer Program*, 1988.

R.H.A. IJzermans, M. W. Reeks, E. Meneguz, M. Picciotto, and A. Soldati. The effect of the basset history force on particle clustering in homogeneous and isotropic turbulence. *Phys. Rev. E*, 80:015302, 2009.

F. Jiang, B. Pettersen, and H. I. Andersson. Turbulent wake behind a concave curved cylinder. *J. Fluid Mech.*, 878:663–699, 2019.

H. Jiang and L. Cheng. Large-eddy simulation of flow past a circular cylinder for Reynolds numbers 400 to 3900. *Phys. Fluids*, 33:034119, 2021.

R. A. Jørgen. *Simple geometry-Complex flow A computational study of turbulent particle-laden flows impinging on a cylinder*. PhD dissertation, Norwegian University of Science and Technology, 2018.

C. Jung, T. Tél, and E. Ziemniak. Application of scattering chaos to particle transport in a hydrodynamical flows. *Chaos*, 107:244501, 1993.

A. G. Kravchenko and P. Moin. Numerical studies of flow over a circular cylinder at Re_D=3900. *Phys. Fluids*, 12:403–417, 2000.

T.C.W. Lau and G. J. Nathan. Influence of stokes number on the velocity and concentration distributions in particle-laden jets. *J. Fluid Mech.*, 757: 432–457, 2014.

O. Lehmkuhl, I. Rodríguez, R. Borrell, and A. Oliva. Low-frequency unsteadiness in the vortex formation region of a circular cylinder. *Phys. Fluids*, 25:085109, 2013.

X. Liu, A. Wei, K. Luo, and J. Fan. Numerical study of the effects of particles on the near wake around a circular cylinder. *Int. J. Comput. Fluid Dyn.*, 29:150–160, 2015.

E. K. Longmire and J. K. Eaton. Structure of a particle-laden round jet. *J. Fluid Mech.*, 236:217–257, 1992.

F. Lucci, A. Ferrante, and S. Elghobashi. Modulation of isotropic turbulence by particles of Taylor length-scale size. *J. Fluid Mech.*, 650:5–55, 2010.

K. Luo, J. Fan, W. Li, and K. Cen. Transient, three-dimensional simulation of particle dispersion in flows around a circular cylinder Re = 140-260. *Fuel*, 88:1294–1301, 2009.

M. Manhart. A zonal grid algorithm for DNS of turbulent boundary layers. *Computers & Fluids*, 33:435–461, 2004.

B. Marcu, E. Meiburg, and P. K. Newton. Dynamics of heavy particles in a Burgers vortex. *Phys. Fluids*, 7:400–410, 1995.

M. R. Maxey. The gravitational settling of aerosol particles in homogeneous turbulence and random flow fields. *J. Fluid Mech.*, 174:441–465, 1987.

M. R. Maxey and J. J. Riley. Equation of motion for a small rigid sphere in a nonuniform flow. *Phys. Fluids*, 26:883–889, 1983.

M. R. Maxey, E. J. Chang, and L. P. Wang. Interactions of particles and microbubbles with turbulence. *Exp. Therm. Fluid Sci.*, 12:417–425, 1996.

R. Mittal and G. Iaccarino. Immersed boundary methods. *Annu. Rev. Fluid Mech.*, 37:239–261, 2005.

R. Mittal, R. Ni, and J.-H. Seo. The flow physics of COVID-19. *J. Fluid Mech.*, 894:F2, 2020.

M. Momenifar and A. D. Bragg. Local analysis of the clustering, velocities, and accelerations of particles settling in turbulence. *Phys. Rev. Fluids*, 5: 034306, 2020.

R. Monchaux, M. Bourgoin, and A. Cartellier. Preferential concentration of heavy particles: A Voronoï analysis. *Phys. Fluids*, 22:103304, 2010.

R. Monchaux, M. Bourgoin, and A. Cartellier. Analyzing preferential concentration and clustering of inertial particles in turbulence. *Int. J. Multiphase Flow*, 40:1–18, 2012.

C. S. Ng, K. L. Chong, R. Yang, M. Li, R. Verzicco, and D. Lohse. Growth of respiratory droplets in cold and humid air. *Phys. Rev. Fluids*, 6:054303, 2021.

S. Olivieri, F. Picano, G. Sardina, D. Iudicone, and L. Brandt. The effect of the basset history force on particle clustering in homogeneous and isotropic turbulence. *Phys. Fluids*, 26:041704, 2014.

T. Oujia, K. Matsuda, and K. Schneider. Divergence and convergence of inertial particles in high-Reynolds-number turbulence. *J. Fluid Mech.*, 905:A14, 2020.

P. Parnaudeau, J. Carlier, D. Heitz, and E. Lamballais. Experimental and numerical studies of the flow over a circular cylinder at reynolds number 3900. *Phys. Fluids*, 20:085101, 2008.

N. Peller, A. Le Duc, F. Tremblay, and M. Manhart. High-order stable interpolations for immersed boundary methods. *Int. J. Numer. Meth. Fluids*, 52:1175–1193, 2006.

C. S. Peskin. Flow patterns around heart valves: a numerical method. *J. Comput. Phys.*, 10:252–271, 1972.

E. Roland and J. Kreuzinger. Hydrodynamic/acoustic splitting approach with flow-acoustic feedback for universal subsonic noise computation. *J. Comput. Phys.*, 444:110548, 2021.

O. Samant, J. Alageshan, S. Sharma, and A. Kuley. Dynamic mode decomposition of inertial particle caustics in Taylor-Green flow. *Sci. Rep*, 11: 10456, 2021.

T. Sapsis and G. Haller. Inertial particle dynamics in a hurricane. *J. Atmos. Sci.*, 66:2481–2492, 2009.

J. D. Scargle. Studies in astronomical time series analysis. II. Statistical aspects of spectral analysis of unevenly spaced data. *Astrophys J.*, 263: 835–853, 1982.

M. Schirber. Nobel Prize: Complexity, from atoms to atmospheres. *Physics Focus*, 2021.

R. A. Shaw. Particle-turbulence interactions in atmospheric clouds. *Annu. Rev. Fluid Mech.*, 35:183–227, 2003.

Z. Shi, F. Jiang, L. Zhao, and H. I. Andersson. Clusters and coherent voids in particle-laden wake flow. *Int. J. Multiphase Flow*, 141:103678, 2021a.

Z. Shi, F. Jiang, L. Zhao, and H. I. Andersson. Direct numerical simulation of a three-dimensional temporal mixing layer with particle dispersion (manuscript under review). *J. Fluid Mech.*, 2021b.

K. D. Squires and J. K. Eaton. Fractal clustering of inertial particles in random flows. *Phys. Fluids*, 3:1169–1178, 1991.

H. L. Stone. Iterative solution of implicit approximations of multidimensional partial differential equations. *SIAM J. Numer. Anal.*, 5:530–558, 1968.

H. Strandenes, B. Pettersen, H. I. Andersson, and M. Manhart. Influence of spanwise no-slip boundary conditions on the flow around a cylinder. *Computers & Fluids*, 156:48–57, 2017.

H. Strandenes, F. Jiang, B. Pettersen, and H. I. Andersson. Low-frequency oscillations in flow past an inclined prolate spheroid. *Int. J. Heat Fluid Flow*, 78:108421, 2019.

Y. Tagawa, J. M. Mercado, V.N. Prakash, E. Calzavarini, C. Sun, and D. Lohse. Three-dimensional Lagrangian Voronoï analysis for clustering of particles and bubbles in turbulence. *J. Fluid Mech.*, 693:201–215, 2012.

L. Tang, Y. Wen, Y. Yang, C. T. Crowe, J. N. Chung, and T. R. Troutt. Self-organizing particle dispersion mechanism in a plane wake. *Phys. Fluids*, 4:2244–2251, 1992.

J. Tom and A. D. Bragg. Multiscale preferential sweeping of particles settling in turbulence. *J. Fluid Mech.*, 871:244–270, 2019.

F. Toschi and E. Bodenschatz. Lagrangian properties of particles in turbulence. *Annu. Rev. Fluid Mech.*, 41:375–404, 2009.

R. Vallée, C. Henry, E. Hachem, and J. Bec. Inelastic accretion of inertial particles by a towed sphere. *Phys. Rev. Fluids*, 3:024303, 2018.

Z. Wan and T. Sapsis. Machine learning the kinematics of spherical particles in fluid flows. *J. Fluid Mech.*, 857:R2, 2018.

P. Welch. The use of fast fourier transform for the estimation of power spectra: a method based on time averaging over short, modified periodograms. *IEEE Trans. Audio Electroacoust.*, 15:70–73, 1967.

C.H.K. Williamson. The natural and forced formation of spot-like 'vortex dislocations' in the transition of a wake. *J. Fluid Mech.*, 243:393–441, 1992.

C.H.K. Williamson. Vortex dynamics in the cylinder wake. *Annu. Rev. Fluid Mech.*, 28:477–539, 1996.

J. H. Williamson. Low-storage Runge-Kutta schemes. *J. Comput. Phys.*, 35:48–56, 1980.

Y. Yang, C. T. Crowe, J. N. Chung, and T. R. Troutt. Experiments on particle dispersion in a plane wake. *Int. J. Multiphase Flow*, 26:1583–1607, 2000.

J. Yao, Y. Zhao, G. Hu, J. Fan, and K. Cen. Numerical simulation of particle dispersion in the wake of a circular cylinder. *Aerosol Sci. Technol.*, 43: 174–187, 2009.

H. Yoshimto and S. Goto. Self-similar clustering of inertial particles in homogeneous turbulence. *J. Fluid Mech.*, 577:275–286, 2007.

M. M. Zdravkovich. *Flow around circular cylinders: Volume I: Fundamentals*. Oxford Science Publications, 1997. ISBN 9780198563969.

H. Q. Zhang, U. Fey, and B. R. Noack. On the transition of the cylinder wake. *Phys. Fluids*, 7:779–794, 1995.

Article I

On simulation of particle-laden wake flow

Zhaoyu Shi, Fengjian Jiang, Håkon Strandenes, Lihao Zhao, Helge I. Andersson

In: MekIT'19: 10th National Conference on Computational Mechanics, Trondheim, Norway. International Center for Numerical Methods in Engineering (CIMNE), pp. 407-418, 2019

10. National Conference on Computational Mechanics
MekIT'19
B. Skallerud and H I Andersson (Eds)

ON SIMULATION OF PARTICLE-LADEN WAKE FLOW

ZHAOYU SHI[1], FENGJIAN JIANG[2,3], HELGE I. ANDERSSON[1] AND HÅKON STRANDENES[4]

[1]Department of Energy and Process Engineering, Norwegian University of Science and Technology (NTNU)
Campus Gløshaugen, 7491 Trondheim, Norway
e-mail: helge.i.andersson@ntnu.no, zhaoyu.shi@ntnu.no
Web pages: https://www.ntnu.edu/employees/helge.i.andersson
https://www.researchgate.net/profile/Shi_Zhaoyu

[2] Department of Marine Technology, NTNU
Campus Tyholt, 7491 Trondheim, Norway
e-mail: fengjian.jiang@ntnu.no

[3] Department of Ships and Ocean Structure, SINTEF Ocean
Marinteknisk senter Tyholt, 7052 Trondheim, Norway
e-mail: Fengjian.Jiang@sintef.no
Web page: https://www.sintef.no/en/all-employees/employee/?empId=7875

[4] Kreuzinger und Manhart Turbulenz GmbH
Kirchenstraße 34, 81675 Munich, Germany
e-mail: h.strandenes@km-turbulenz.no
Web page: http://www.km-turbulenz.de/index.php

Key words: numerical simulation, particle concentration, wake flow

Abstract. To preliminarily investigate the inertial particle distribution in the unsteady flow around a circular cylinder, we perform three-dimensional numerical simulations of particle-laden cylinder wake flow at $Re_D = 100$, defined based on cylinder diameter and uniform incoming flow velocity. A one-way coupling approach is utilized in the dilute suspensions. A strong correlation between local vortex structures and particle concentration is observed. Particle concentration presents different patterns at different Stokes numbers. Particles at very small Stokes numbers are distributed uniformly across the whole vortex cores. Particles at intermediate Stokes numbers aggregate mainly on the outer borders of vortex core regions and leave the vortex core a void region. The particles at large Stokes numbers are swept less away from the high vorticity region and even form a passage through the outer range of vorticity in the near wake. It is also observed that the detached particle bow shock appears when Sk is 3 and above. Moreover, some heavy particles are trapped inside the vortex cores close to the downstream border while particles align smoothly along the upstream border.

1 INTRODUCTION

The transportation and concentration of inertial particles in laminar and turbulent flows play an important role in many engineering and natural situations, i.e. sediments in rivers and scour around offshore wind-turbine foundations etc. Unlike tracer particles, inertial particles follow their own dynamics resulting from the interaction with local vortex structures, known as *preferential concentration*. Previous numerical work in different particle-laden flows has been well-established by using direct numerical simulation (DNS) for homogeneous isotropic turbulence [1] [2] and channel flows [3]. Many statistical measures, such as particle distribution PDF, correlation dimension [4] and Voronoï diagrams [5] etc., are employed to investigate the relationship between particle concentration and local flow structures. However, there is still a lack of research on particle-laden wake flow although pioneering work has been done for plane wake [4] and cylinder wakes [6] [7]. Most numerical and experimental results provided visualization results of particle distribution from light to heavy particles in wakes and showed a clear inertia-dependency of concentration. Some mechanisms have been proposed to account for particle concentration, such as centrifugal mechanism and the sweep-stick property for zero-acceleration points in the flow [1]. The underlying mechanism, unfortunately, is still not fully understood, especially not for the wake flow due to the lack of quantitative analysis.

The particle concentration pattern not only depends on particle inertia, but also vortex structures in the wake. The vortex shedding at different Reynolds numbers is comprehensively described in Williamson's review [8]. Considering the computational cost of tracking millions of particles, most previous direct numerical simulations stayed at low Reynolds numbers. In order to introduce turbulence in the particle-laden cylinder wake flow, the Reynolds-Averaged-Navier-Stokes (RANS) method is commonly utilized to study the particle concentration at high Reynolds numbers [9]. However, the significant streamwise vortices in a turbulent wake flow are wiped out in steady RANS, while unsteady RANS is still unable to properly account for turbulent fluctuations which makes the transient solution doubtful.

We aim at investigating particle concentration by DNS at higher Reynolds number. The particle library implemented in MGLET has been validated in homogeneous isotropic turbulence by Gobert [10] [11]. We consider two-dimensional unsteady laminar flow around a straight circular cylinder at $Re_D = 100$ in this paper as a preliminary study. The computational details of the flow configuration is given in section 2. The visualization results of particle distributions at different Stokes numbers are given in section 3. Finally, we conclude the observed concentration patterns in section 4.

2 COMPUTATIONAL DETAILS

2.1 Flow configuration

We set a straight circular cylinder with diameter D and length $5.12D$ in an incompressible flow of a Newtonian fluid. The flow configuration is illustrated in figure 1, which

is a box with lengths of L_x, L_y and L_z. We define the streamwise direction as x-direction, crossflow direction as y-direction and spanwise direction as z-direction. The Reynolds number $Re_D = U_0 D/\nu$ is given by the free-stream velocity U_0 and the cylinder diameter D (ν is kinematic viscosity of the incompressible fluid). Other quantities in our simulation are all measured by U_0 and D.

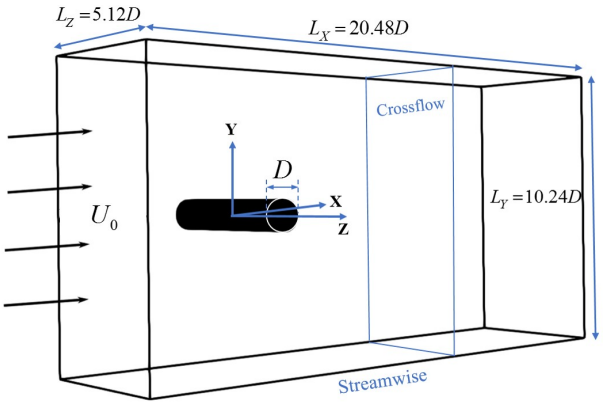

Figure 1: Three-dimensional computational domain for the flow around a straight circular cylinder. Note that the domain is not to scale.

As a preliminary test of inertial particle dispersion in the cylinder wake flow, we only choose a relatively short domain to avoid unnecessary computational cost. Figure 2 perceptually shows the domain size in our case compared with an experimental visualization from Zdravkovich [12], both at $Re_D = 100$. The lower plot in figure 2 is a snapshot of the vorticity field in spanwise direction in a fully developed flow obtained from our simulation. As depicted in figure 2, the computational domain only approximately includes three pairs of vortices in the near wake region. The flow around a circular cylinder at $Re_D = 100$ is often taken as a benchmark to validate a CFD solver, in which the wake flow stays two-dimensional but unsteady [8]. The boundary conditions used in the simulations are summarised below:

- Inlet: uniform free stream, $u_i = (U_0, 0, 0)$.
- Outlet: Neumann boundary conditions for the velocity components ($\partial u/\partial x = \partial v/\partial x = \partial w/\partial x = 0$) and zero pressure ($p = 0$).
- Two vertical sides normal to Z-direction: periodic condition.
- Two horizontal sides normal to Y-direction: free-slip boundary condition, i.e. $v = 0$ and $\partial u/\partial y = \partial w/\partial y = 0$.

- The surface of the cylinder is treated as a no-slip and impermeable wall.

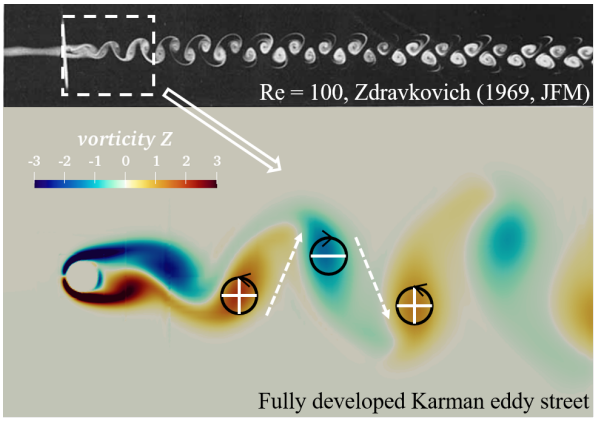

Figure 2: Sketch of the comparison of the domain sizes at $Re_D = 100$ between an experiment by Zdravkovich [12] and the simulation in this paper.

2.2 Numerical methods

In order to directly solve the incompressible three-dimensional transient flow around a cylinder, we utilize a second-order finite volume method to discretize the Navier-Stokes equation

$$\frac{\partial u_i}{\partial x_i} = 0, \tag{1}$$

$$\underbrace{\frac{\partial u_i}{\partial t}}_{\text{time change rate}} + \underbrace{u_j \frac{\partial u_i}{\partial x_j}}_{\text{convection}} = \underbrace{-\frac{1}{\rho_f}\frac{\partial p}{\partial x_i}}_{\text{pressure force}} + \underbrace{\nu \frac{\partial^2 u_i}{\partial x_j \partial x_j}}_{\text{viscous diffusion}} \tag{2}$$

The simulations are performed by the well-verified DNS/LES solver MGLET [13]. Fluid velocity and pressure information are stored in discretized 3D staggered equidistant Cartesian grids [14]. In equation (2), the viscous diffusion term is approximated by a central-difference scheme, and eq(2) is time advanced by an explicit low-storage third-order Runge-Kutta scheme. Meanwhile, a Poisson equation is iteratively solved by the combination of successive-over-relaxation (SOR) and Stone's strongly implicit procedure (SIP), and also is corrected to fulfill mass conservation equation. In order to handle the boundary condition of particle-wall interaction, the cut-cell finite-volume approach is implemented in MGLET to extract the normal vector, which is crucial when particles impinge the wall.

The cuboid Cartesian cells are intersected by the curved wall, and the cell shape is exactly computed from the intersection. This results in the formation of the finite volume with polyhedron shape. This process is enforced by employing the direct-forcing Immersed Boundary Method (IBM). A Ghost-cell methodology of IBM is enforced in the standard MGLET [15], while a cut-cell IBM approach implemented as a new feature in MGLET, for the first time, is applied in this study [16].

When the flow is statistically periodic, particles are seeded from the inlet boundary with uniform velocity U_0 and distributed randomly into the flow field. Considering the heavy computation of resolving the flow around finite-size particles, point-particles are the most commonly used model to track particles in an Euler-Lagrangian framework. The particles are assumed to be small, spherical and inertial ($\rho_p/\rho_f = 1000$, ρ_p, ρ_f are the particle and the surrounding fluid density). We also assume particle suspension here is dilute with volume fraction below 10^{-6}, so that particle collisions rarely occur, and particles are one-way coupled to the statistically periodic wake flow. The Maxey-Riley equation which describes the particle motion reduces to eq(3) with only Stokes drag force acting on particles:

$$\frac{du_{p,i}}{dt} = \frac{C_D Re_p}{24\tau_p}(u_{f@p,i} - u_{p,i}) \tag{3}$$

where $u_{p,i}$ is particle velocity component updated by an adaptive fourth-order RosenbrockWanner scheme with third-order error estimator, $u_{@p,i}(t) = u(t, x_{p,i}(t))$ is the fluid velocity component seen by the particle at position $x_{p,i}$ obtained by linear interpolation. An explicit Euler scheme is used to update particle position. $\tau_p = \frac{\rho_p d^2}{18\rho_f \nu}$ is particle relaxation time (d is particle diameter), and we define Stokes number $Sk = \tau_p/\tau_f$ as a non-dimensional parameter to measure the particle inertia ($\tau_f = D/U_0$). The Stokes drag coefficient C_D is a function of particle Reynolds number $Re_P = d \parallel \mathbf{u_p} - \mathbf{u_{f@p}} \parallel /\nu$, and we use a piecewise model to include five different Re_P-dependent Stokes drags referenced from Clift et al [17]:

$$C_D = \begin{cases} 3/16 + 24/Re_P & Re_p < 0.01, \\ 24/Re_p(1 + 0.15Re_P^{0.687}) + 0.42/(1 + 4.25 \times 10^4 Re_P^{-1.16}) & Re_P < 3 \times 10^5, \\ 29.78 - 5.3 \times \log_{10} Re_P & 3.5 \times 10^5 < Re_P \\ & < 4 \times 10^5, \\ 0.1 \log_{10} Re_P - 0.49 & 4 \times 10^5 < Re_P < 10^6, \\ 0.19 - 8 \times 10^4/Re_P & 10^6 < Re_P. \end{cases} \tag{4}$$

We set particles into three groups by Stokes number Sk ranging from light to heavy ones, and each group includes three different Sk cases with the corresponding Sk shown in table 1. The total number of particles in each group is around 410000. Particles in one grid are assigned to one CPU to proceed the parallelization. For the simplicity of the

problem, the interaction between a particle and the cylinder wall is taken as fully elastic bouncing.

Table 1: Particle conditions of simulation runs.

Group	Light			Medium			Heavy		
Sk	5.6e-5	1.7e-3	5.6e-3	0.1	0.55	1.0	3.0	6.5	10.0
Npart	413685			411755			419009		

2.3 Computational mesh

The computational domain is discretized by a multi-level structured Cartesian mesh, where the grids are constructed by cubic boxes with different grid spacings in an unstructured arrangement. Figure 3 gives an impression of four-level grids, where $N \times N \times N$ cells are uniformly filled in each grid box, regardless of the grid size. The region close to the cylinder needs the finest grid, and we define the minimum grid spacing as spatial resolution. The grid size increases by a factor of 2, i.e. the size of level-4 grid in figure 3 is $0.02D$ while $0.16D$ for level-1 grid.

In order to examine the sufficiency of the mesh for case $Re_D = 100$, we generate two additional meshes(case 2 and 3). Table 2 provides the details of the time-averaged drag-coefficient C_D, the root-mean-square of the lift force coefficient C_{L-rms} and the spanwise force C_Z calculated from all three cases. The difference of theses quantities between all cases is very modest while the Strouhal numbers $St = fD/U_0$ are slightly higher than the reference value 0.16, which could be caused by insufficient time windows. We also note that C_D and C_{L-rms} are higher than the commonly recognized approximate numbers 1.3 and 0.22 respectively. This is known to arise from the lack of crossflow domain size in our simulations. To ensure the accuracy of the interpolation to obtain particle velocity and a physical vorticity field, we prefer the finer mesh with 2.09million cells. Figure 4 presents three normalized forces around the cylinder including drag coefficient C_D, lift coefficient C_L and spanwise force coefficient C_Z. The regular waves of C_D and C_L indicate a fully developed unsteady laminar flow. Since the cylinder is almost independent of the spanwise force with C_Z being 10^{-6}, the flow can be trusted as two dimensional flow. The Strouhal number in case 1 can be approximately obtained as 0.176 from the average of 34 time periods of the lift coefficient.

3 PARTICLE CONCENTRATION

The occurrence of a Kármán vortex-street is the typical characteristic of flow around a circular cylinder in the laminar vortex shedding regime $49 < Re_D < 194$ [8], as figures 5 and 6 present. These large-scale vortical structures in the wake have a significant effect on

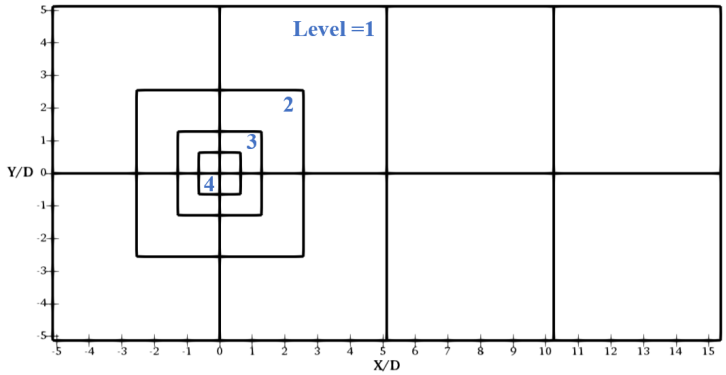

Figure 3: Sketch of the multigrids (4-level shown here). A slice of the multi-level grid box distribution in the (X,Y)- plane is shown. Each square represents a 3D grid box and contains the amount of $N \times N \times N$ grid cells. Grid resolution increases as the square size gets smaller.

Table 2: Grid independence study for $Re_D = 100$. Ngrid and Ncell represent the total number of grid boxes and cells, respectively.

Case	Resolution	C_D	C_{L-rms}	C_Z	St	Ngrid	Ncell
1	0.02D	1.932	0.483	-1.527e-6	0.176	64	2.09million
2	0.04D	1.965	0.507	-1.327e-6	0.177	32	1.05million
3	0.08D	2.061	0.542	8.509e-13	0.178	16	0.52million

the dispersion of inertial particle, known as preferentially concentration. Here we observe the particle distribution at various Stokes number Sk from 0.0056 to 10. Since the flow is two-dimentional at $Re_D = 100$, we only present the particle distribution and vorticity in an (X,Y)-plane.

For the very low-Sk particles shown in figure 5(a), they can be regarded as tracers following the flow evolution and thus uniformly scattered in the flow field. No accumulation is visually identifiable. In figure 5(b), however, periodic void regions appear in the vortex cores for both positive and negative vorticity. The particles are swept away from vortex cores indicating a slight effect of inertia. The void regions become larger with the shedding vortex growing along the streamwise direction, as marked in figure 5(b) with white curves.

Figure 6 presents instantaneous snapshots of particle distribution for medium and heavy particles. In the left panels, we observe the inertial particles of Sk=0.55 and 1 also cannot follow the fluid as particles of Sk=0.1, and continue to run away from the vortex

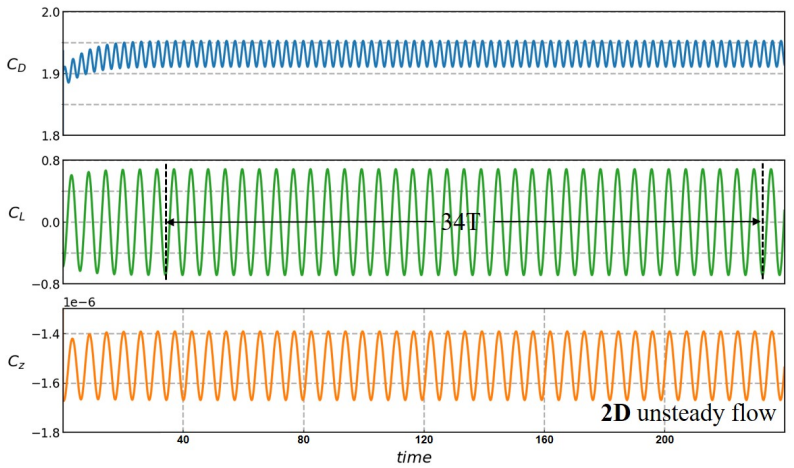

Figure 4: The drag coefficient C_D, lift coefficient C_L and normalized force C_Z in spanwise direction at $Re_D = 100$. Case 1 with spatial resolution 0.02D.

cores due to the centrifugal force. The edges of these void regions reach closer to the outer range of vorticity braids as particle inertia plays a more significant role in the distribution pattern. As we can compare in figure 6(a)∼(c), the void regions are getting wider and longer as Sk increases. However, figures 6(d) ∼(f) show quite opposite patterns when Sk continues increasing from 3 to 10, in which the length of void regions is decreasing. It is observed that particles get less and less driven to the outer border, and the heavy particles behave more like bullets. They tend to pass through the vortex center and form a connected passage in the near wake instead of the individual void regions shown in figure 6(a)∼(c).

Comparing the particle distribution at Sk=1.0 and 10 in figure 7(a), we observe that the particles accumulate along the upstream border which makes the border smooth. In contrast, a small portion of particles stay inside the vortex core near the downstream, and more particles are trapped inside the vortex core as Sk increases. The velocity of the particles located upstream is slightly smaller than the ones at downstream shown in figure 7(b). The observations in figure 5 and 6 indicate a strong Sk-dependency of particle concentration in the wake flow. Similar pattern of the particle distribution can also be found in Tang's experiments and DNS results in plane wake [4], and the numerical simulation work for cylinder wakes in [6] [7] at higher Re numbers with three-dimensional effect. The most interesting phenomenon for heavy particles is that a detached particle bow shock is clearly observed in front of the cylinder with a distance due to the fully elastic collision model. The shock angle is getting wider as Sk increases, and the shock wave is hardly influenced by the wake as Sk=6.5 and 10.

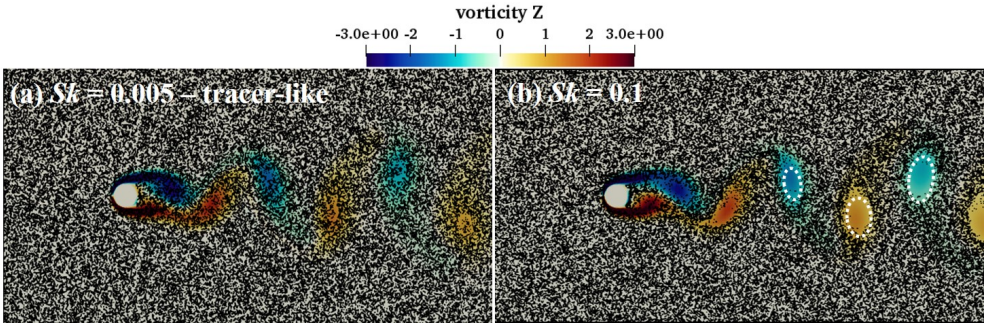

Figure 5: Instantaneous snapshots of particle distribution and Z-direction vorticity in the light particle simulations: (a) Sk=0.005 and (b) Sk=0.1.

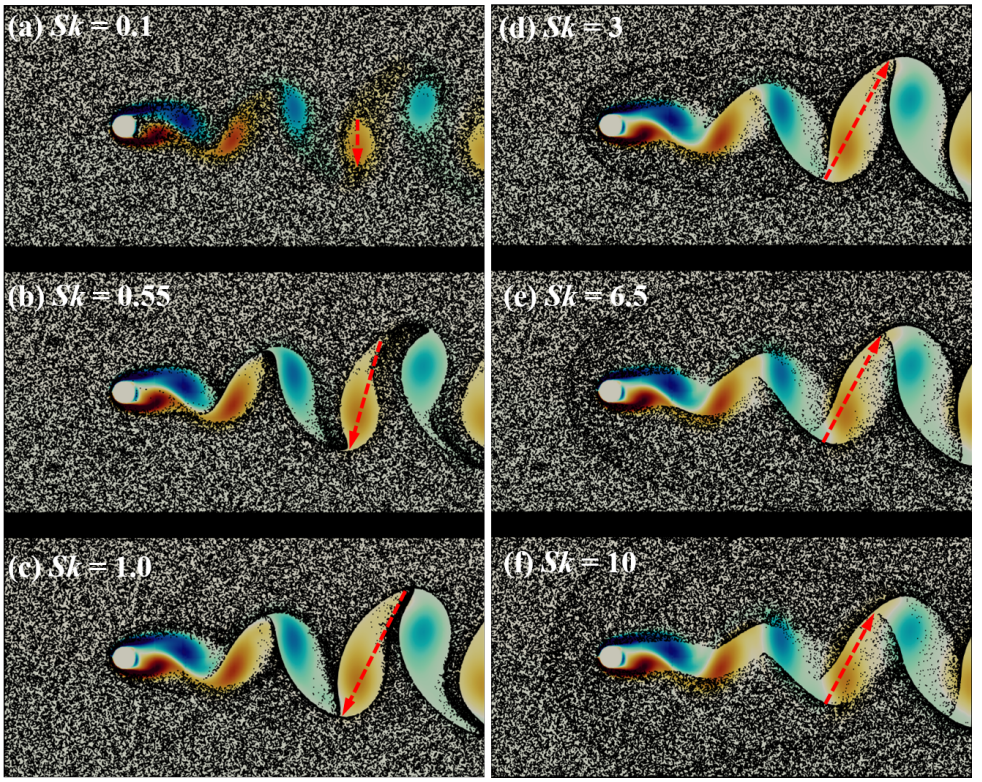

Figure 6: Instantaneous snapshots of particle distribution and Z-direction vorticity at different Sk. The left panel corresponds to the medium particles: (a)∼(c) Sk=0.1, 0.55, 1.0 and the right panel corresponds to the heavy particles: (b)∼(f) Sk=3.0, 6.5, 10.

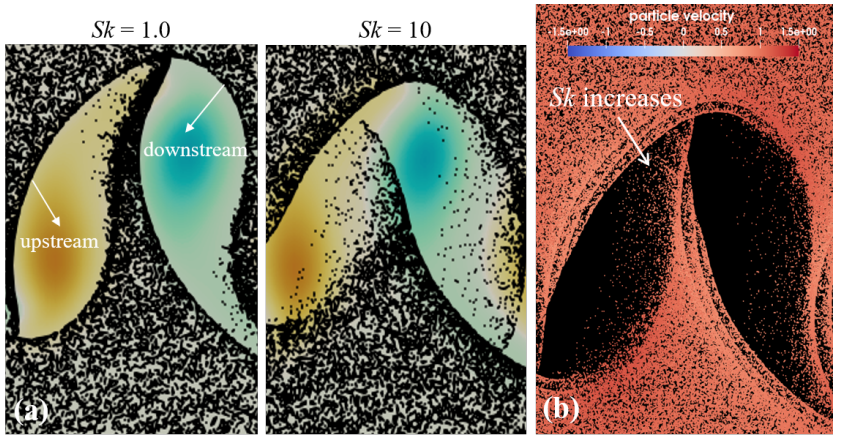

Figure 7: (a) Comparison of the instantaneous particle distribution in the same vortex pair at Sk=1.0 and 10. (b) Superimposed particle velocity distribution at Sk=3, 6.5, 10 in the l vortex pair.

4 CONCLUSIONS

In this preliminary study, we performed numerical simulation for particle-laden flow around a circular cylinder at $Re_D = 100$. We aim at studying the inertial particle distribution at different Stokes numbers Sk ranging from 0.0056 to 10. The Lagrangian method was used to track the trajectories of point particles with one-way coupling.

It is found that the particle distribution presents various patterns between light, intermediate and heavy particles. The particle concentration is strongly correlated to the vortex structure. The particles at extremely small Stokes numbers completely follow the fluid motion and disperse across the vortex cores without preferential concentration. The particles at intermediate Stokes numbers show different degrees of preferentially concentration at Sk=0.1, 0.55, 1. The common tendency is that particles concentrate on the outer boundaries of vortices due to the centrifugal force, and thus separate void zones appear. The empty regions expand larger as Stokes number increases but remain below 1. For the heavy particles, the void regions appear as a passage especially at Sk=10, which indicates that bullet-like particles get across the outer boundaries of vorticity and maintain their own motions. Also we find that particles would flow back towards the vortex core region but still pass smoothly around the front edge. Based on all simulation results, we clearly can see an inertial effect on the pattern of particle concentration.

5 ACKNOWLEDGEMENTS

The use of the Norwegian HPC **Fram** was granted by the Norwegian Research Council under project nn2649k and nn9191k. The work is financially supported by *NTNU Energy* for a research fellowship.

REFERENCES

[1] Monchaux, R,. Bourgoin, M., Cartellier, A. Analyzing preferential concentration and clustering of inertial particles in turbulence. *Int. J. Multiphase Flow* (2012) **40**:1-18

[2] Ireland, P. J., Bragg, A. D., Collins, L.R. The effect of Reynolds number on inertial particle dynamics in isotropic turbulence. Part 1. Simulations without gravitational effects. *J. Fluid Mech.* (2016) **796**:617-658

[3] Zhao, L. H., Challabotla, N. R., Andersson, H.I., Variano, E.A. Rotation of non-spherical particles in turbulent channel flow. *Phys. Rev. Lett.* (2015) **115**:244501

[4] Tang, L., Wen, F., Yang, Y., Crowe, C. T., Chung, J. N., Troutt, T. R. Self-organizing particle dispersion mechanism in a plane wake. *Phys. Fluids* (1992) **4**:2244-2251

[5] Garca-Villalba, M., Kidanemariam, A. G., Uhlmann, M. DNS of vertical plane channel flow with finite-size particles: Voronoi analysis, acceleration statistics and particle-conditioned averaging. *Int. J. Multiphase Flow* (2012) **46**:54-74

[6] Kun, L., Fan, J. R., Li, W.C., Cen, K. F. Transient, three-dimensional simulation of particle dispersion in flows around a circular cylinder (Re = 140-260) *Fuel* (2009) **88**:1294-1301

[7] Yao, J., Zhao, Y. L. , Hu, G. L., Fan, J. R., Cen, K. F. Numerical simulation of particle dispersion in the wake of a circular cylinder. *Aerosol Science and Technology* (2009) **43**:174-187

[8] Williamson, C. H. K. Vortex dynamics in the cylinder wake. *Annu. Rev. Fluid. Mech.* (1996) **28**:477-539

[9] Ong, M. C., Holmedal, L. E., Myrhaug, D. Numerical simulation of suspended particles around a circular cylinder close to a plane wall in the upper-transition flow regime. *Coastal Engineering* (2012) **61**:1-7

[10] Gobert, C., Analytical assessment of models for large eddy simulation of particle laden flow. *J. Turbul* (2010) **11**

[11] Gobert, C., Large Eddy Simulation of Particle-Laden Flow (Doctoral dissertation). Technical University of Munich, Munich, German (2009).

[12] Zdravkovich, M. Smoke observations of the formation of a Kármán vortex street. *J. Fluid Mech.* (1969) **37(3)**:491-496.

[13] Manhart, M., Friedrich, R. DNS of a turbulent boundary layer with separation. *Int. J. Heat Fluid Flow* (2002) **23**:572-781.

[14] Manhart, M. A zonal grid algorithm for DNS of turbulent boundary layers. *Comput. Fluids* (2004) **33**:435-461.

[15] Peller, N., Duc, A. L., Tremblay, F., Manhart, M. High-order stable interpolations for immersed boundary methods. *Int. J. Numer. Meth. Fluids* (2006) **52**:1175-1193.

[16] Mittal, R., Iaccarino G. Immersed boundary methods. *Annu. Rev. Fluid. Mech.* (2005) **37**:239-261.

[17] Clift, R., Grace, J. R., Weber, M. E. Bubbles, Drops and Particles. *Academic Press.* New York (1978)

[18] Eaton, J.K., Fessler, J.R. Preferential concentration of particles by turbulence. *Int. J. Multiphase Flow* (1994) **20**:169-209

Article II

Bow shock clustering in particle-laden wetted cylinder flow

Zhaoyu Shi, Fengjian Jiang, Lihao Zhao, Helge I. Andersson

International Journal of Multiphase Flow, Vol 130, 103332, 2020

International Journal of Multiphase Flow 130 (2020) 103332

Contents lists available at ScienceDirect

International Journal of Multiphase Flow

journal homepage: www.elsevier.com/locate/ijmulflow

Bow shock clustering in particle-laden wetted cylinder flow

Zhaoyu Shi [a], Fengjian Jiang [b,*], Håkon Strandenes [c], Lihao Zhao [d,a], Helge I Andersson [a]

[a] Department of Energy and Process Engineering, Norwegian University of Science and Technology, 7491 Trondheim, Norway
[b] Department of Ships and Ocean Structures, SINTEF Ocean, 7052 Trondheim, Norway
[c] Kreuzinger und Manhart Turbulenz GmbH, 7069 Trondheim, Norway
[d] AML, Department of Engineering Mechanics, Tsinghua University, 100084 Beijing, China

ARTICLE INFO

Article history:
Received 23 January 2020
Revised 24 April 2020
Accepted 2 May 2020
Available online 6 May 2020

Keywords:
Particle clustering
Cylinder wake flow
Bow shock
Numerical simulation

ABSTRACT

The inhomogeneous distributions of inertial particles in the unsteady flow around a wetted circular cylinder at $Re = 100$ were investigated in one-way coupled three-dimensional numerical simulations. The Kármán vortex cells determine the local patterns of particle clustering. In the vicinity of the cylinder, a bow shock-like clustering was explored via Voronoï diagrams. The shape of the bow shock in terms of width and thickness strongly depends on Stokes number, Sk. For high-Sk particles, the bow shock was wider and less affected by the vortex shedding in the near wake and thus extended further downstream. We tracked low-Sk particles in a steady potential flow aimed at mimicking the viscous flow field close to the cylindrical surface. The converging tendency of the particle trajectories at the upstream of the cylinder supported the appearance of a bow shock. Furthermore, we analysed the trajectory of a Sk=0.1 particle in viscous flow, wherein the direction of the perpendicular component of the Stokes drag force was altered from outwards to inwards at the inflection point of the trajectory. This observation suggests that the centrifugal mechanism makes particle trajectories converge and thereby contributes to the formation of the bow shock.

1. Introduction

Inertial particles suspended in fluid flows are commonly encountered in industrial and environmental settings, such as the scouring around near-shore wind turbine foundations, particle deposition and erosion in turbomachines, in combustion systems, and aerosol scavenging around buildings etc. Numerous experimental and numerical studies on particle-laden flows have been conducted in homogeneous isotropic turbulence (HIT) (Ireland et al. 2016; Sumbekova et al. 2017), and channel flows (Fessler et al. 1994; Marchioli and Soldati, 2002; Zhao et al. 2010), but to a lesser extent in wake flows. Pioneering research on a particle-laden wake behind a plane revealed that the large-scale vortical structures lead to distinctly inhomogeneous particle distributions even though the particles were uniformly seeded. A significant feature of this self-organized behaviour is known as particle *clustering*. Tang et al. (1992) simulated particle dispersion in the wake behind a thick plane and made comparisons with a plane mixing layer. It was shown that the evolution of large-scale vortices influenced the spatial clustering patterns. Their findings were subsequently supported by experimental results from Yang et al. (2000), which confirmed the strong dependency of the clustering on particle inertia, consistent with the numerical simulations by Tang et al. (1992).

Only a few studies focus on particle clustering in flow past a circular cylinder and in the wake behind the cylinder. This lack of investigations contrasts with the substantial focus on single-phase flow around circular cylinders, which has been thoroughly studied over several decades both in laminar and turbulent regimes; see e.g. Williamson (1996) and Zdravkovich (1997). Representative studies employing direct numerical simulations (DNS) by Luo et al. (2009) and a lattice-Boltzmann method (LBM) by Zhou et al. (2011) observed that inertial particles are mostly encountered in high-strain-rate regions at moderate Reynolds numbers. More recent papers by Homann and Bec, 2015 and Vallée et al. 2018 explored particle dispersion in the wake of a sphere, which can be regarded to share qualitative features with the cylinder wake flow. However, most investigations have provided only phenomenological descriptions of the clustering process, without the relevant physical insight in the phenomenon. This contrasts with the studies of particle clustering in HIT, in which alternative mechanisms have been proposed to explain the non-uniform particle distribution. The preferred explanations are the 'centrifugal' mechanism (Maxey 1987; Fessler et al. 1994) applicable for low-

* Corresponding author.
E-mail address: Fengjian.Jiang@sintef.no (F. Jiang).

https://doi.org/10.1016/j.ijmultiphaseflow.2020.103332

inertia particles strongly coupled with the carrier flow at relatively low Reynolds number, and the 'sweep-stick' mechanism suggested by Goto and Vassilicos, 2008 for heavier particles in flows at higher Reynolds number with broad-banded turbulence.

A few different approaches have been applied to quantitatively characterize the particle clustering. The box-counting method, adopted by Fessler et al. (1994), utilizes uniform boxes to measure the probability density function (PDF) and is simple to implement but sensitive to the chosen box size. Another direct method introduced by Melheim (2005) is to define a spherical or elliptical cutoff length of two colliding particles in order to detect particle clusters. Lagrangian statistics, i.e. time correlations (Uhlmann 2008) and radial distribution functions (RDF; Wood et al. 2005), are based on the particle velocity and distance along trajectories to provide the possibility of finding particles. A drawback is that Lagrangian statistics are unable to provide instantaneous particle clustering but only give global information. A relatively new technique, known as Voronoï analysis or tessellation, was introduced by Monchaux and Bourgoin, 2010 and successfully applied to estimate the instantaneous particle clustering in channel flows (Nilsen et al. 2013) and HIT (Tagawa et al. 2012) for both point-like and finite-size particles. An advantage of this diagnostic tool is its efficiency in dealing with numerous particles, e.g. of the order of 10^5. Monchaux et al. (2012) compared other common methods mentioned above and pointed out the challenge of tracking dynamical clusters. Voronoï analysis is likely to be an attractive diagnostic tool in bluff-body wake flows in general and in cylinder wakes in particular.

To realistically model particle dispersion in cylinder wake flows, particle-wall collisions are essential, whereas interparticle collisions are negligible as long as the suspension is sufficiently dilute. In industrial processes, such as filtration and coagulation of aerosols, slurry transport etc., the interstitial viscous fluid is no longer negligible, like in dry granular flow, but instead acts as a resistant or lubrication force which may lead to a certain particle kinetic energy loss. An elastic restitution coefficient may account for the energy loss. Joseph et al. (2001) experimentally studied the normal coefficient of restitution (ratio of the rebound to impact particle velocity), wherein the normal coefficient is close to zero within a certain critical range of particle inertia. This suggests that no rebound of particles appears below the threshold. Kantak and Davis (2004) extended the analysis to the tangential coefficient of restitution under oblique collisions and concluded that the tangential velocity is barely damped with the corresponding restitution coefficient close to unity over a wide range of particle inertia. Therefore, particle motion can be approximately modeled not as rebound but sliding along the wall. Kantak and Davis (2006) also provided comprehensive analytical expressions for the restitution coefficients, which supported the previous experimental results of Kantak and Davis (2004). Cylinders with wetted surfaces occur in two-phase flow reactors in oil refineries, during dip coating processes (Quéré, 1999; Scriven, 1988), and in so-called fog harvesting when liquid films are formed on the collecting wires, see Shi et al. (2018).

The majority of studies on particle-laden cylinder wake flow focus on the dynamic interaction between particles and coherent structures or vortex cells in the wake. There are only a few studies on particle movements in the vicinity of a cylindrical body, which is controlled by the particle-wall collision model. A striking phenomenon, known as a *bow shock*, was observed in front of a cylinder immersed in a dilute dry granular flow, see e.g. Wassgren et al. (2003) and Bharadwaj et al. (2006). They analyzed the dependency of the particle drag force constructed from the restitution coefficient on Mach and Knudsen numbers. Of particular interest is that a bow shock structure was not only formed in a supersonic flow (Boudet et al. 2008) but also in incompressible flows. To the best of our knowledge, a particulate bow shock structure has never been observed in dilute suspensions of inertial particles in continuous incompressible viscous flows.

This paper presents observations of a bow shock in a simulated wet cylinder flow, and quantitatively investigates how particle inertia effects change the shape of the bow shock via Voronoï diagrams. A sliding particle-wall collision model is adopted to mimic a wetted circular cylinder coated by a thin film layer. The details of the mathematical modeling as well as the computational methods and parameters are given in Section 2 of the paper. A discussion of Voronoï data and explanations based on a potential flow approach is given in Section 3. In Section 4, centrifuging is suggested as a mechanism responsible for the observed convergence of particle trajectories, which eventually leads to bow-shock formation. Finally, Section 5 summarizes the important observations and draws the conclusions.

2. Problem description

2.1. Governing equations and numerical methods

We perform three-dimensional numerical simulations by directly solving the transient flow around a circular cylinder at Reynolds number $Re = U_0 D/\nu = 100$ (U_0 is the free-stream velocity, D is cylinder diameter). The well-verified DNS/LES solver MGLET (Manhart et al. 2001; Manhart and Friedrich 2002) utilizes a second-order finite volume method to discretize the mass conservation and Navier-Stokes equation for incompressible flow

$$\frac{\partial u_i}{\partial x_i} = 0, \tag{1}$$

$$\underbrace{\frac{\partial u_i}{\partial t}}_{\text{acceleration}} + \underbrace{u_j \frac{\partial u_i}{\partial x_j}}_{\text{convection}} = \underbrace{-\frac{1}{\rho_f}\frac{\partial p}{\partial x_i}}_{\text{pressure force}} + \underbrace{\nu \frac{\partial^2 u_i}{\partial x_j \partial x_j}}_{\text{viscous diffusion}}. \tag{2}$$

The instantaneous fluid velocity components u_i and pressure p are stored in discrete staggered equidistant three-dimensional Cartesian grids. The solution is advanced in time by an explicit low-storage third-order Runge-Kutta scheme. The Poisson equation is iteratively solved by Stone's strongly implicit procedure (SIP). The cuboid Cartesian cells are intersected by the curved cylinder wall, and the shapes of those polyhedron cells are exactly computed from the intersection by an immersed boundary method (IBM) with cut-cell implementation. The *cut-cell* approach is employed to obtain the precise surface geometry and normal vector of the intersected cells to handle the particle-wall collision boundary condition, whereas the conventional ghost-cell approach in MGLET cannot (Peller et al. 2006).

We consider the movement of inertial point-like spheres ($\rho_p/\rho_f = 1000$, where ρ_p and ρ_f are the densities of the particles and the fluid, respectively). The particle loading is low with a volume fraction below 10^{-6}, such that the flow is unaffected by the presence of the particles and one-way coupling between the particle and fluid phases can be justified wherever the particles are not too densely clustered. The Maxey-Riley equation (Maxey and Riley 1983), which describes the individual particle motion in a Lagrangian framework, is simplified to:

$$\frac{\mathrm{d}u_{p,i}}{\mathrm{d}t} = \frac{C_D Re_p}{24\tau_p}(u_{f@p,i} - u_{p,i}), \tag{3}$$

$$\frac{\mathrm{d}x_{p,i}}{\mathrm{d}t} = u_{p,i}, \tag{4}$$

where only the Stokes drag force is acting on a particle and all other forces are assumed negligible in Eq. (3). The particle velocity $u_{p,i}$ is updated by an adaptive fourth-order Rosenbrock-Wanner

Table 1
Characteristics of the flow configuration and the corresponding force coefficients.

Flow configuration			Main flow coefficients		
$\Delta x_{\min}/D$	Domain size ($L_x/D \times L_y/D \times L_z/D$)	Cell number (million)	C_d	C_{l-rms}	St
0.016	32.768 × 16.384 × 4.096	14.42	1.3932	0.2401	0.1694

scheme with a third-order error estimator (Gobert 2010), while the fluid velocity component $u_{f@p,i}(t) = u(t, x_{p,i}(t))$ seen by the particle at position $x_{p,i}$ is obtained by linear interpolation. The particle position x_p is obtained from the kinematic relation in Eq. (4). An explicit Euler scheme is used to update particle position. The particle relaxation time $\tau_p = \rho_p d^2/18\rho_f \nu$ where d is particle diameter, is used to define the Stokes number $Sk = \tau_p/\tau_f$ as a non-dimensional parameter to measure the particle inertia. Here, $\tau_f = D/U_0$ is a nominal flow time scale. The drag coefficient C_D is taken as a function of particle Reynolds number $Re_p = d \parallel \boldsymbol{u}_p - \boldsymbol{u}_{f@p} \parallel /\nu$ in order to allow for finite-Re_p corrections to the Stokes limit $Re_p \to 0$. We adopt a piecewise model of C_D, covering different ranges of Re_p; see Cliff et al. (1978) and the recent paper by Shi et al. (2019). In practice, however, the Reynolds number Re_p is always lower than 3×10^5 in the present cases, for which the corresponding C_D formula

$$C_D = \frac{24}{Re_p}(1 + 0.15Re_p^{0.687}) + \frac{0.42}{1 + 4.25 \times 10^4 Re_p^{-1.16}} \tag{5}$$

is activated.

2.2. Computational set-up

The Eulerian PDEs (1,2) governing the fluid flow are integrated on a three-dimensional computational domain discretized by a multi-level structured Cartesian mesh, which is constructed by different sizes of grid boxes filled with the same number of grid cells. A local grid refinement is enforced by embedding zonal grids around the cylinder (Manhart 2004). The center of the cylinder is at (X = 0, Y = 0). The inlet boundary condition for all simulations is a constant free-stream velocity $(u, v, w) = (U_0, 0, 0)$ and a Neumann condition $\partial p/\partial x = 0$ on pressure. Zero pressure and Neumann conditions on the three velocity components, i.e. $\partial u/\partial x = \partial v/\partial x = \partial w/\partial x = 0$, are applied at outlet of the domain. Periodicity is imposed at the two vertical side-walls; i.e. normal to the spanwise Z-direction. Free-slip boundary conditions are used in the crossflow Y-direction, i.e. $v = 0$ and $\partial u/\partial y = \partial w/\partial y = 0$. The dimensions of the computational domain are provided in Table 1, which also reports the time-averaged drag coefficient $C_d = 2F_d/\rho_f U_0^2 LD$ (F_d : drag force, L: cylinder length), the standard deviation of the lift coefficient $C_{l-rms} = 2F_{l-rms}/\rho_f U_0^2 LD$ (F_{l-rms} : root-mean-square lift force) and Strouhal number $St = f\tau_f = fD/U_0$ (f : vortex shedding frequency). The present values are close to the reference ranges 1.32 ~ 1.42, 0.22 ~ 0.29 and 0.164 ~ 0.168 in Kim et al. (2001), Su et al. (2007) and Tseng and Ferziger (2003), respectively.

Inertial point-particles are seeded into the flow field with initial velocity $u_p(t_0) = U_0$ at the inlet. The particle seeding started when a strictly periodic vortex shedding had been established at $t_0 = 250\tau_f$. Nine different nominal Stokes numbers Sk are considered. These different particles can be classified, according to their mass, into three categories; see Table 2. Depending on the particle inertia, parameterized by Sk, particles may or may not collide with the cylinder. During collisions between particles and the wet cylinder surface, the energy loss is associated with the wall-normal and wall-tangential velocity components. According to the previous conclusion concerning the restitution coefficients (Joseph et al. 2001; Kantak and Davis 2006), the normal restitution coefficient is zero at low Stokes numbers while the tangential one is approximately unity. Therefore, we adopt the *sliding motion* collision model as the boundary condition for impacting particles, wherein the ratios of normal and tangential momentum losses are unity and zero, respectively.

Table 2
Particle information for different simulations.

Particle class	Light	Medium	Heavy
Sk	1 3 5	8 12 16	24 40 56
Particles per Sk		~ 10^5	

3. Bow shock particle clustering

3.1. Density inhomogeneities

It is well-known that the flow past a straight circular cylinder at $Re = 100$ remains two-dimensional and laminar although it becomes unsteady. Fig. 1 presents the snapshots of inertial particle distributions over the whole domain for Sk = 1, 5, 16, 56, superimposed on the instantaneous spanwise vorticity (ω_z), which reflects the typical Kármán vortex street in the wake behind the cylinder. Since the flow is two-dimensional and two-componential, i.e. the two velocity components u and v are independent of Z, all particles can be projected into a single XY-plane to increase the statistical samples. Density inhomogeneities are noticeable both in the near and far wake in Fig. 1. For the low-Sk case shown in Fig. 1(a), particles accumulate locally close to the front of the cylinder as they approach the wall and are therefore convected downstream by the surrounding fluid. Owing to the relatively low Stokes number, the particles tend to follow the carrier flow. These particles are expelled away from the vortex cores and tend to align along the vortex cell boundaries. The higher particle concentration in the front of the cylinder and around the cylinder surface resembles a *bow shock* (more easily seen in Fig. 1(b, c, d)). The shape of the bow shock in the near wake at X ≈ 3D for Sk = 1 is clearly affected by the shed vortices. At higher Stokes numbers, the heavier particles are less coupled to the underlying flow and move almost ballistically towards the cylinder. Therefore, we can observe a clear appearance of a thin particle layer where the darkness reflects the dense particle concentration. This curved high-particle-concentration layer is referred to as *bow shock* in the present study. A similar phenomenon of particle clustering was reported in dilute *granular* flow, see Bharadwaj et al. (2006), in which a wider and thicker bow shock was formed upstream of the cylinder. The present bow shock, however, forms in a fundamentally different flow, namely in a viscous continuum. Moreover, the shock becomes wider for higher Stokes number in Fig. 1(b) ~ (c). We observe, at Sk = 56, that the high-concentration layer extends well into the intermediate wake, i.e. downstream of X ≈ 10D. The various patterns of particle concentration in the near-cylinder region exhibit substantial effects of inertia.

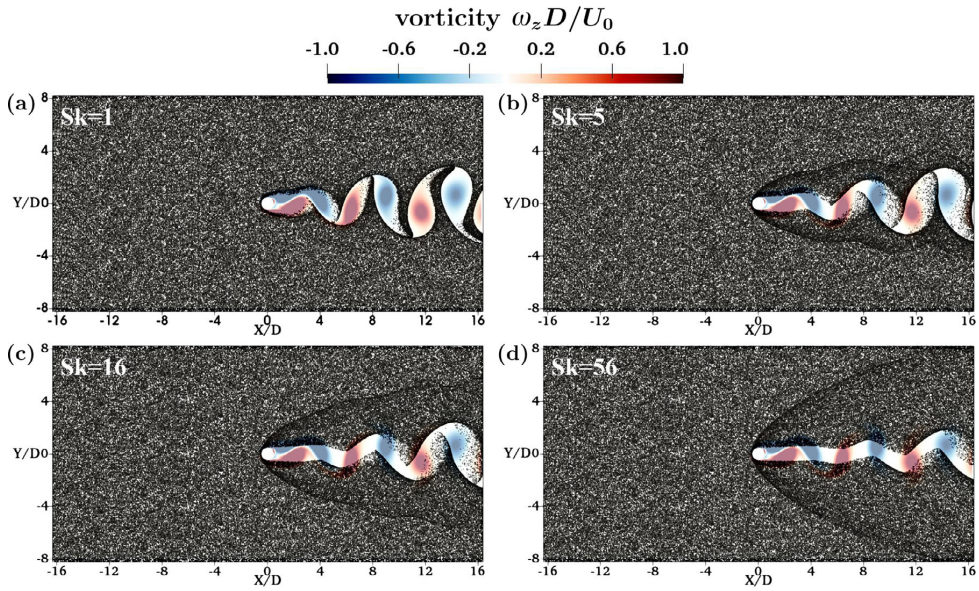

Fig. 1. Instantaneous particle distribution (black dots) projected on an XY-plane. (a)Sk = 1; (b)Sk = 5; (c)Sk = 16; (d)Sk = 56. The background (color) is the spanwise vorticity $\omega_z D/U_0$. (For interpretation of the references to color in this figure legend, the reader is referred to the web version of this article.)

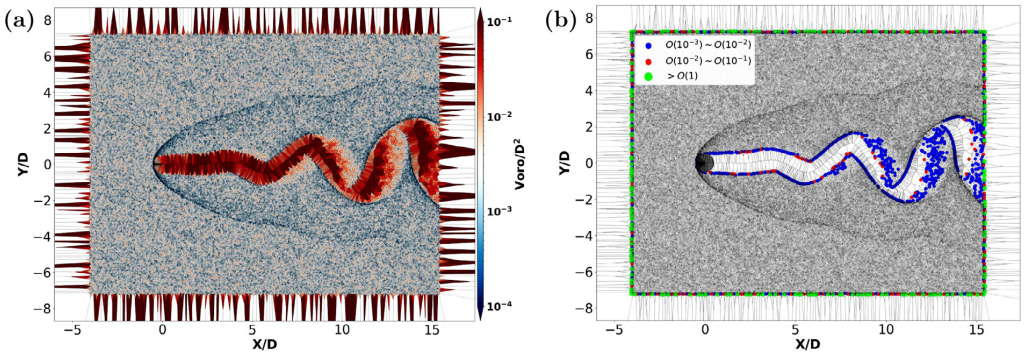

Fig. 2. (a) Example of Voronoï diagrams at Sk = 12. The bow shock (dark dense path) is detected by the smallest Voronoï cells. (b) Abnormal particles with Voronoï area over 1 (green dots) lying along the boundaries of the domain. Particles with Voronoï area between $O(10^{-3})$ and $O(10^{-1})$ (red and blue dots) are located within the vortex structures. (For interpretation of the references to color in this figure legend, the reader is referred to the web version of this article.)

3.2. Voronoï analysis

Voronoï diagrams have been mostly used to quantify particle clustering in HIT and channel flows, but can also be computationally efficient in detecting the bow shock in the cylinder wake. We employed two intrinsic libraries called Voronoï and ConvexHull in Python to calculate the Voronoï cell areas and plot the diagram. Fig. 2(a) shows an example of Voronoï cells in two dimensions at Sk = 12 for illustration, where the domain is divided into polygon cells, each corresponding to one given particle ('site'). All vertices in each Voronoï cell are closer to the site than to any other cell's site. This property, free of any cell-size effects, indicates that the inverse of a Voronoï cell area is a measure of the local particle concentration. The average Voronoï cell area is approximately $O(10^{-3})$ and is given as A_d/N_p, where N_p is the total number of particles and $A_d = L_x \times L_y$ is the area of the two-dimensional plane. The average Voronoï cell area is used only as a reference value and not for normalization. The bow shock in the vicinity of the cylinder is identified by the substantially smaller Voronoï cell areas of order $O(10^{-6} \sim 10^{-5})$. The Voronoï cells within the vortex cores in the wake are much larger than those identifying the bow shock with areas ranging from $O(10^{-3})$ to $O(10^{-1})$. Thus, inertial particles are rarely observed within the vortex cores. It should be noted that the Voronoï cell areas along the borders of the computational domain are abnormally large. All such ill particles with a cell area value larger than 1 shown in Fig. 2(b) are disregarded in the further post-processing.

A statistical analysis of the Voronoï areas at X = -0.3D, i.e. 0.2D downstream of the stagnation point, is exhibited in Fig. 3. This figure is composed of a scatter plot of the density distribution, a histogram and the kernel density estimation (KDE) curve across the flow. The histogram and KDE plots depicted in Fig. 3 are based on 1.5×10^4 scatter points from an ensemble of 13 different time steps. For each sample point x_i, a Gaussian kernel func-

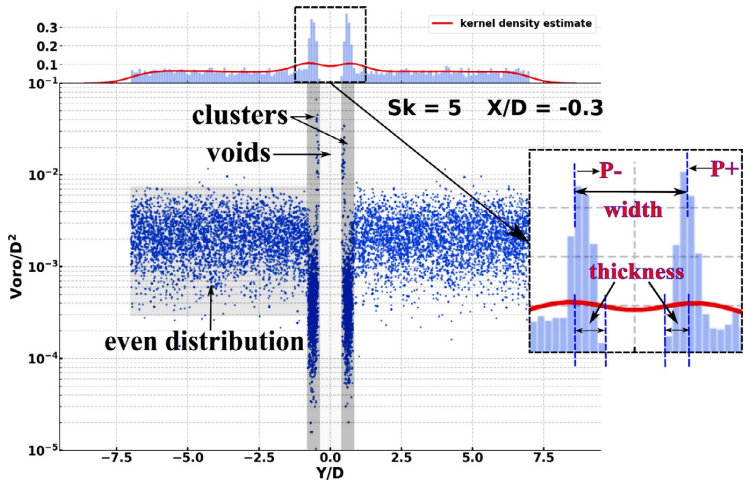

Fig. 3. Illustration of cluster identification at X/D = −0.3 of case Sk = 5. The scatter plot jointly with a histogram and kernel density estimate describe the Voronoï area distribution in the crossflow (Y) direction at both sides of the cylinder. Colored shading regions visualize the clusters (dark gray), voids (light gray) and evenly distributed region (medium gray). P-/+ in the zoom-in plot marks the left/right bin edge corresponding to the outside border of lower/upper bow shock, respectively. The bow shock width and thickness are indicated in the inset. (For interpretation of the references to color in this figure legend, the reader is referred to the web version of this article.)

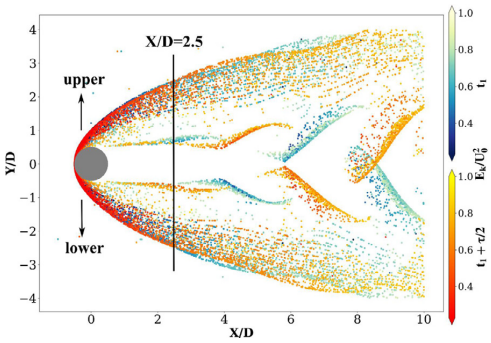

Fig. 4. Instantaneous particle distributions for Sk = 12 at two different time steps t_1 and $t_1 + \tau/2$, where τ is the period of vortex shedding. Particles with velocity magnitude $\leq 0.9U_0$ are not shown. The particles are color-coded according to their normalized kinetic energy. Notice the different color-bars used to distinguish between the two different time steps. The vertical line at X/D = 2.5 indicates the particular location X_c, downstream of which the particle distributions are time dependent. (For interpretation of the references to color in this figure legend, the reader is referred to the web version of this article.)

tion $K(x_i, h)$ is used at its centre to ensure symmetry about this point. The probability density estimation (pdf) is then estimated by adding all of the individual kernel functions corresponding to each sample, and dividing by the number of points. A kernel is controlled by a smoothing parameter known as binwidth, see further and more detailed descriptions of the applied Gaussian KDE in Python. In Fig. 4, we superimpose two particle distribution snapshots, separated in time by half of the shedding period τ. Notice that different colorbars are used for the two different distributions. In the upstream part of the plot, i.e. X/D $<$ 2.5, the two distributions almost perfectly collapse. This demonstrates that the vortex shedding in the wake plays a negligible role on the upstream particle concentration at Stokes number Sk = 12, although the particle concentration downstream of $X_c/D = 2.5$ is distinctly time dependent. We believe that the particular position X_c, upstream of which the unsteadiness can be ignored, shifts further downstream with increasing Stokes number. This finding justifies that the particle distributions can be considered as statistically steady and that Voronoï data can be gathered from several different time instants, disregarding the potential need for phase-averaging, in the shedding-unaffected area.

We can define clusters, voids and evenly-distributed regions according to the Voronoï area distribution illustrated in Fig. 3. Of particular interest is the perceptually symmetric clusters where particles accumulate densely within a thin layer at both sides of the cylinder. The left interface (Y/D $<$ 0) corresponds to the outside border of the lower bow shock seen in Fig. 4, while the right interface (Y/D $>$ 0) corresponds to the outside border of the upper bow shock. Fig. 5 presents such Voronoï plots for particles with three different representative Stokes numbers Sk = 5, 16, and 56, one from each of the three different categories in Table 2. We consider two streamwise positions for each Sk, namely X/D = −0.3 and $X/D = X_c/D$, where the X_c/D is the position upstream of which the particle concentration can be considered to be unaffected by the vortex shedding and therefore time independent. For the three Stokes number shown in Fig. 5, $X_c/D \approx$ 1.1, 2.5 and 5.5, respectively.

It is observed from Fig. 5(a, b, c) that the sharp interfaces on both sides extend further away from the centerline, reflecting that the bow shock widens with downstream distance. In the first row of Fig. 5 for X/D = −0.3, the particles are aggregated densely within a short crossflow range, which is understandable since the outside border is close to the cylinder wall at this upstream position. In comparison with the shapes of the interfaces at downstream positions, shown in the bottom row of Fig. 5, they are less dense and the scatter points become more evenly distributed on both sides of the sharp interface, especially for large Sk. Additionally, the interfaces are getting thinner and shorter downstream, which means that Voronoï cells become larger than the ones upstream of the center of the cylinder. This tendency can also be seen in Fig. 4, namely that the particles are spread away in the cross stream direction and this leads to the less converged distribution downstream. Therefore, it only makes sense to measure the thickness of the bow shock at relatively upstream position due to

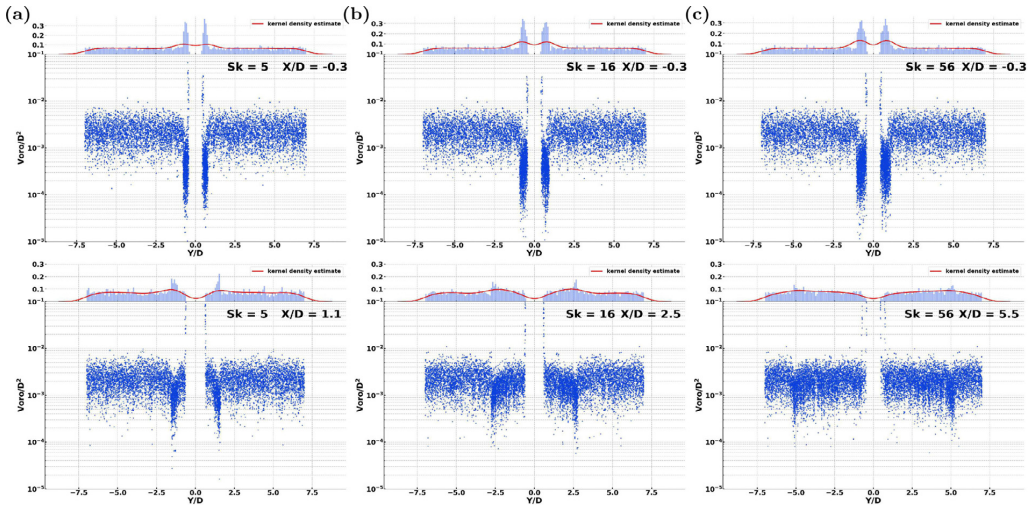

Fig. 5. Voronoï area distributions for three different Stokes numbers are plotted. For each Sk, two downstream positions (X/D) are chosen. (a) Sk = 5, (b) Sk = 16, (c) Sk = 56.

the blurred distributions inside the border of the bow shock in the downstream wake.

In order to quantify the variation of the Voronoï data, we focus on how the *thickness* and *width* of the bow shock change with downstream position and Stokes number. Doing so, we extract the left and right edges of the highest bins on both sides, marked as P−/+, respectively, in Fig. 3. The width W of the bow shock is defined as the distance between P+ and P−. The thickness T is also illustrated in the inset in Fig. 3, which is obtained by subtracting P−/+ and the right/left bin edge of the first non-zero bin on the left/right side. Fig. 6(a) shows how the width of the bow shock varies with increasing downstream positions based on the absolute values of P−/+. This variation is consistent with the observation of the bow shock shape in Fig. 1. We are now in a position to plot the variation of the width W and thickness T as a function of Sk at some downstream positions X/D. The data in Fig. 6(b, c) both show a pronounced increase of the width and thickness for low Sk, while only a modest dependence on Sk is observed for intermediate and high Stokes numbers, particularly so at the downstream position X/D = 0.3.

3.3. Potential flow comparison

In order to explore a possible mechanism for the formation of a bow shock, we examine trajectories of inertial particles in steady potential flow around the circular cylinder. Streamlines of the potential flow are shown in the lower half of Fig. 7(a) and compared with the streamlines of the time-averaged viscous flow field at $Re = 100$ in the upper half. The two streamline topologies are strikingly different in the wake of the cylinder, as one should expect. Nevertheless, the streamline patterns in the stagnation zone and around the shoulders of the cylinder are rather similar. This close resemblance suggests that the potential flow field can be adopted as a simplified model to explore the behavior of the inertial particles. In this semi-theoretical analysis, the Stokes number is restricted to $Sk \leq 0.14$ so that the light particles will not hit the wall, but pass around the cylinder without impacting. A collision model is therefore not required. Ten $Sk = 0.1$ particles were seeded at the inlet and tracked through the potential flow, without colliding with the cylinder. As the particles approach the cylinder, their trajectories are deflected upwards in Fig. 7(b) and they tend to converge at about 45°. The convergence of trajectories seem to start near the *inflection point* of the streamlines, from where the inertial spheres gradually depart from the streamlines. Eventually, unlike the streamlines, the particle trajectories gather in a fairly thin layer around the shoulder of the cylinder. The clustered trajectories are only partially following the curvature of the streamlines towards the lee side of the cylinder. A similar pattern of particle trajectories was recently reported by Vallée et al. 2018 for particles moving around a sphere in a potential flow. Also their particles had Stokes number below a certain threshold.

The role played by the inflection point is due to the alteration of the direction of the centrifugal force which tends to make inertial particles move away from the center of curvature. The centrifugal force points in one direction upstream of the inflection point and in the opposite direction downstream of the inflection point. This is believed to have a focusing effect on the trajectories of inertial particles. The centrifuging mechanism will be further explored in Section 4.

Based on an assumption of a low Stokes number, it is possible to derive a first-order approximation for the particle velocity $\boldsymbol{u_p}$ if Sk is taken as a small perturbation parameter. According to Maxey (1987), Goto and Vassilicos, 2008 and Tom and Bragg (2019)

$$\boldsymbol{u_p}(\boldsymbol{x_p}, t) = \boldsymbol{u}(\boldsymbol{x}, t) - Sk\frac{\mathrm{D}\boldsymbol{u}(\boldsymbol{x}, t)}{\mathrm{D}t}|_{\boldsymbol{x}=\boldsymbol{x_p}} + O(Sk^2) \tag{6}$$

where $\boldsymbol{x}$ is an arbitrary Euler point in the discretized space covering the particle position $\boldsymbol{x_p}$ and $\mathrm{D}\boldsymbol{u}(\boldsymbol{x}, t)/\mathrm{D}t$ is the fluid acceleration field. By taking the divergence of this simplified particle velocity in Eq. (6), one obtains:

$$\nabla \cdot \boldsymbol{u}_p(\boldsymbol{x_p}, t) = -Sk\nabla \cdot ((\boldsymbol{u}(\boldsymbol{x}, t) \cdot \nabla)\boldsymbol{u}(\boldsymbol{x}, t)|_{\boldsymbol{x}=\boldsymbol{x_p}} \tag{7}$$

Eq. 7 implies that the particle velocity is compressible even if the flow field is incompressible. In particular, the particles are compressed when $\nabla \cdot \boldsymbol{u_p} < 0$.

The divergence of the particle velocity field can now be found from the potential fluid flow field. It turns out that the divergence field shown in Fig. 7(c) only varies with the radial distance from the cylinder surface. The divergence is everywhere large negative and approaches zero at large distances from the cylinder. Large

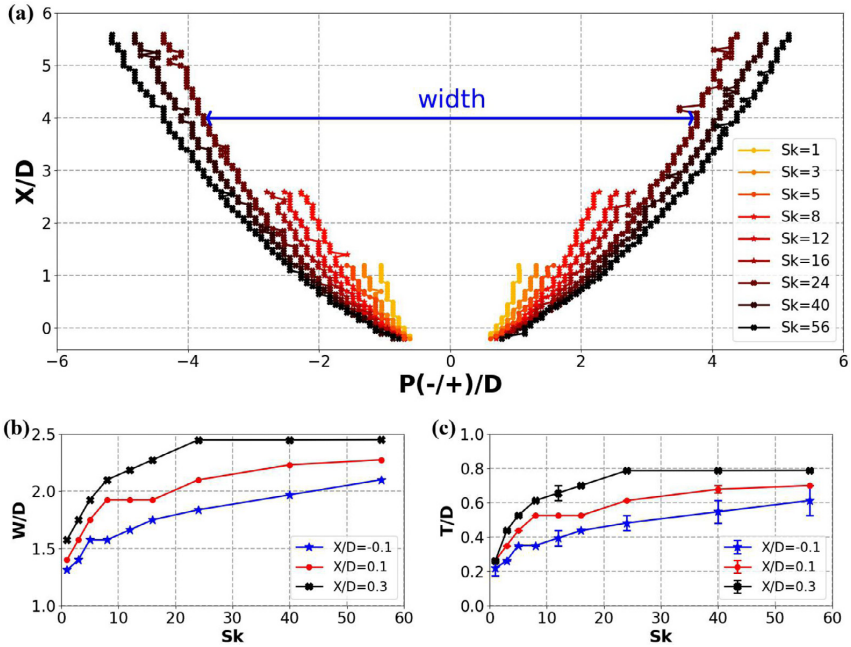

Fig. 6. (a) The location of the bow shock as a function of downstream position X/D for different Stokes numbers (the blue arrow line indicates the bow shock width W). P−/P+ measures the local distance from the symmetry plane ($Y = 0$). The width W (b) and thickness T (c) vary with Sk. The thickness T in (c) is the average of the bow shock thickness on the two sides of the cylinder. The error bars represent deviations between the two thicknesses. (For interpretation of the references to color in this figure legend, the reader is referred to the web version of this article.)

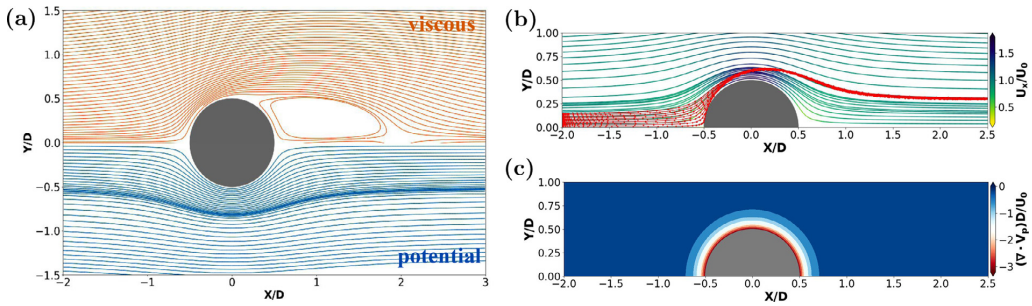

Fig. 7. (a) Comparison of the streamlines between potential flow (blue) and time-averaged viscous flow from numerical simulation (orange). (b) The trajectories of seeded particles with Sk = 0.1 (red dots and lines) in potential flow superimposed with the streamlines. (c) The same trajectories as the ones in (b) superimposed with the first-order approximation of particle divergence in Eq. (7). (For interpretation of the references to color in this figure legend, the reader is referred to the web version of this article.)

negative values are seen in an annular ring around the cylinder. This suggests that the particle field is compressed, i.e. clustered. It is therefore convincing to see that this is the region in which the particle trajectories are converging. The clustering of the trajectories is likely associated with the bow shock formation seen at $Re = 100$.

4. Centrifuging by alternating streamline curvature

The potential flow field and the viscous flow field in Fig. 7(a) are quite similar around the front part of the cylinder (X/D $<$ 0) when it comes to the streamline pattern. A common feature of both is that a streamline with Y/D $>$ 0 first curves upwards and thereafter bends downwards. The center of curvature is first above the streamline and thereafter below the streamline, which means that the center of curvature switches from above to below at the so-called inflection point (IP) defined mathematically as where the second derivative of the streamline is zero. A fluid element which follows a curved streamline is affected by a force acting in the direction towards the center of curvature. This force is needed to provide the centripetal acceleration towards the center of curvature. In our case, the pressure force is likely to dominate over the viscous force. The pressure force on a fluid element $-dp/dr$, where r for convenience is the radial distance from the center of the cylinder, is first acting outwards until the IP and thereafter inwards. This is indeed plausible since the highest pressure is found in the frontal stagnation point area and a much lower pressure is seen around the shoulders of the cylinder, as shown in Fig. 8(a).

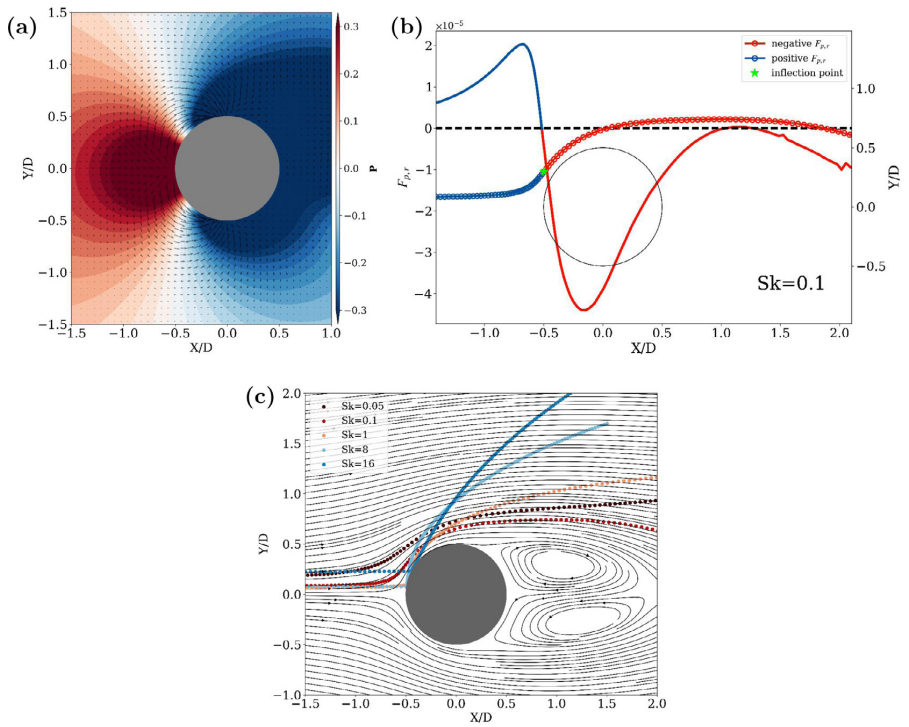

Fig. 8. (a) Pressure distribution (contours) and pressure gradient force (arrows) around the cylinder. (b) Particle trajectory of Sk = 0.1 (line-dot) and the radial component of particle Stokes drag force $F_{r,p}$ (line) at the corresponding position. Blue and orangered colors represent positive and negative $F_{r,p}$, respectively. The inflection point of the particle trajectory is marked with a green star, and well overlapped with the point where $F_{r,p}$ changes the sign along the trajectory. (c) Particle trajectories at Sk = 0.05, 0.1, 1, 8, 16 superimposed with the streamlines of the time-averaged viscous flow. (For interpretation of the references to color in this figure legend, the reader is referred to the web version of this article.)

Analogously, the trajectory of the Sk = 0.1 particle in Fig. 8(b) resembles a streamline. This particle first experiences a positive radial force $F_{p,r}$, which eventually switches to become negative. The switching position, indicated by change of color, is closely related to the IP of the particle trajectory. It should be recalled that the particles are not explicitly affected by the pressure field, but only by the viscous Stokes drag force according to Eq.(3). Along the first stretch of the curved trajectory where the radial force $F_{p,r}$ is positive, the radial fluid velocity is larger than the radial particle velocity. In this region the streamlines divert further away from the circular surface of the cylinder than does the particle trajectory. This situation is reverted when the radial force $F_{p,r}$ changes sign from positive to negative. This happens when the radial particle velocity exceeds the radial fluid velocity and coincides with the IP of the particle trajectory, as indicated in Fig. 8(b).

The centrifugal mechanism is often used to explain why vortical flow structures are depleted of particles. As seen from the curved trajectory of an inertial particle, one usually argues that the real physical radial force (here: the radial component of Stokes drag) is balanced by an oppositely directed fictitious centrifugal force required to make the sum of forces normal to the trajectory equal to zero. In the present case, the centrifugal force inevitably changes sign at the inflection point IP where also the radial drag force changes sign. This physical mechanism is present not only in potential flows but also in viscous flows.

The same arguments apply also for more inertial particles. Trajectories for particles with some different inertia are shown in Fig. 8(c) and superimposed on the time-averaged streamlines at $Re = 100$. The trajectories of the more inertial particles (Sk $\geq$ 1) are strongly affected by their impaction on the cylinder surface. After impaction, the trajectory of the Sk = 16 particle is only modestly curved. This is so because the radial component of the Stokes drag is insufficient to balance a substantially larger centrifugal force.

5. Conclusions

In this work, we have conducted three-dimensional numerical simulations of flow around a wetted circular cylinder at $Re = 100$. Particle-fluid (two-way) and particle-particle (four-way) couplings have been neglected in the present study, although these effects may be of some importance in the most densely populated areas, e.g. in the bow shock. We anyhow believe that the novel observations reported herein are qualitatively correct. The unsteady flow was laden with spherical particles whose inertia was parameterized by a Stokes number, Sk. A strong Sk-dependence of the particle distribution was observed both in the vicinity of the cylinder and in the Kámán vortex street. Attention was devoted to the striking and unexpected clustering appearing in front of the cylinder. The width W and thickness T of this particle *bow shock*, which describes how the bow shock developed in the streamwise X-direction, were quantified by means of Voronoï diagrams. At a given streamwise X-location, the width as well as the thickness of the bow shock increased with particle inertia, i.e. with Sk. The further downstream parts of the bow shock are remarkably affected by the periodic shedding at lower Stokes numbers, whereas the

wider bow shock at high Sk is only modestly influenced by the wake dynamics. We also observed that the unexpectedly dense particle accumulation in the upstream part of the shock became more diluted further downstream, most likely as a consequence of the thickening of the bow shock.

To further explore this peculiar phenomenon, we first tracked light particles with Sk = 0.1 in a time-independent potential flow around the cylinder. Such light particles are closely coupled to the carrier fluid and pass around the cylinder. These semi-analytical results do therefore not depend on any collision model. The Lagrangian particle trajectories show a clear tendency to converge at about the same position as the bow shock was formed in the viscous flow simulations. Inspired by the alteration of the direction of the component of the pressure gradient force perpendicular to a curved streamline, we proposed that the change of curvature of the particle trajectories at their inflection point (IP) may enforce a focusing of the trajectories. We therefore tracked a Sk = 0.1 particle through the viscous flow field. The IP of the particle trajectory coincided with the position where the radial component of Stokes drag force changed direction from inwards to outwards, thereby supporting our assumption that the bow shock formation is associated with the focusing of the particle trajectories caused by the centrifugal mechanism.

Acknowledgments

The use of Fram and Stallo, parts of the Norwegian HPC infrastructure, was granted by the Norwegian Research Council under projects nn2649k and nn9191k. The first author is financially supported by 'NTNU Energy' through a research fellowship. L.Z. acknowledges the Natural Science Foundation of China (Grant Nos: 11702158, 91752205, and 11911530141).

References

Bharadwaj, R., Wassgren, C.R., Zenit, R., 2006. The unsteady drag force on a cylinder immersed in a dilute granular flow. Phys. Fluids 18, 043301. doi:10.1063/1.2191907.

Boudet, J.F., Amarouchene, Y., Kellay, H., 2008. Shock front width and structure in supersonic granular flows. Phys. Rev. Lett. 101, 254503. doi:10.1103/PhysRevLett.101.254503.

Cliff, R., Grace, J., Weber, M.E., 1978. Spheres at higher Reynolds numbers. Bubbles, Drops and Particles. Academic Press, New York, pp. 111–112. Chapter 5

Fessler, J.R., Kulick, J.D., Eaton, J.K., 1994. Preferential concentration of heavy particles in a turbulent channel flow. Phys. Fluids 6, 3742–3749. doi:10.1063/1.868445.

Gobert, C., 2010. Large Eddy Simulation of Particle-Laden Flow. Fakultät für Bauingenieur- und Vermessungswesen PhD dissertation.

Goto, S., Vassilicos, J.C., 2008. Sweep-stick mechanism of heavy particle clustering in fluid turbulence. Phys. Rev. Lett. 100, 054503. doi:10.1103/PhysRevLett.100.054503.

Homann, H., Bec, J., 2015. Concentrations of inertial particles in the turbulent wake of an immobile sphere. Phys. Fluids 27, 053301. doi:10.1063/1.4919723.

Ireland, P.J., Bragg, A.D., Collins, L.R., 2016. The effect of Reynolds number on inertial particle dynamics in isotropic turbulence. Part 1. Simulations without gravitational effects. J. Fluid Mech. 796, 617–658. doi:10.1017/jfm.2016.238.

Joseph, G.G., Zenit, R., Hunt, M.L., Rosenwinkel, A.M., 2001. Particle-wall collisions in a viscous fluid. J. Fluid Mech. 433, 329–346. doi:10.1017/S0022112001003470.

Kantak, A.A., Davis, R.H., 2004. Oblique collisions and rebound of spheres from a wetted surface. J. Fluid Mech. 509, 63–81. doi:10.1017/S0022112004008900.

Kantak, A.A., Davis, R.H., 2006. Elastohydrodynamic theory for wet oblique collisions. Powder Technol. 168, 42–52. doi:10.1016/j.powtec.2006.07.006.

Kim, J., Kim, D., Choi, H., 2001. An immersed-boundary finite-volume method for simulations of flow in complex geometries. J. Comput. Phys. 171, 132–150. doi:10.1006/jcph.2001.6778.

Luo, K., Fan, J., Cen, K., 2009. Transient, three-dimensional simulation of particle dispersion in flows around a circular cylinder Re = 140–260. Fuel 88, 1294–1301. doi:10.1016/j.fuel.2008.12.026.

Manhart, M., 2004. A zonal grid algorithm for DNS of turbulent boundary layers. Comput. Fluids 33, 435–461. doi:10.1016/S0045-7930(03)00061-6.

Manhart, M., Friedrich, R., 2002. DNS of a turbulent boundary layer with separation. Int. J. Heat Fluid Flow 23, 572–581. doi:10.1016/S0142-727X(02)00153-4.

Manhart, M., Tremblay, F., Friedrich, R., 2001. MGLET: a parallel code for efficient DNS and LES of complex geometries. In: Parallel Computational Fluid Dynamics-Trends and Applications. Elsevier Scinece B.V., Amsterdam, pp. 449–456.

Marchioli, C., Soldati, A., 2002. Mechanisms for particle transfer and segregation in a turbulent boundary layer. J. Fluid Mech. 468, 283–315. doi:10.1017/S0022112002001738.

Maxey, M.R., 1987. The gravitational settling of aerosol particles in homogeneous turbulence and random flow fields. J. Fluid Mech. 174, 441–465. doi:10.1017/S0022112087000193.

Maxey, M.R., Riley, J.J., 1983. Equation of motion for a small rigid sphere in a nonuniform flow. Phys. Fluids 26, 883–889. doi:10.1063/1.864230.

Melheim, J.A., 2005. Cluster integration method in Lagrangian particle dynamics. Comput. Phys. Comm. 171, 155–161. doi:10.1016/j.cpc.2005.05.003.

Monchaux, R., Bourgoin, M., 2010. Preferential concentration of heavy particles: A Voronoï analysis. Phys. Fluids 22, 103304. doi:10.1063/1.3489987.

Monchaux, R., Bourgoin, M., Cartellier, A., 2012. Analyzing preferential concentration and clustering of inertial particles in turbulence. Int. J. Multiph. Flow 40, 1–18. doi:10.1016/j.ijmultiphaseflow.2011.12.001.

Nilsen, C., Andersson, H.I., Zhao, L., 2013. A Voronoï analysis of preferential concentration in a vertical channel flow. Phys. Fluids 25, 115108. doi:10.1063/1.4830435.

Peller, N., Duc, A.L., Tremblay, F., Manhart, M., 2006. High-order stable interpolations for immersed boundary methods. Int. J. Numer. Meth. Fluids 52, 1175–1193. doi:10.1002/fld.1227.

Quéré, D., 1999. Fluid coating on a fiber. Annu. Rev. Fluid Mech. 31, 347–384. doi:10.1146/annurev.fluid.31.1.347.

Scriven, L.E., 1988. Physics and applications of dip coating and spin coating. MRS Online Proc. Library Arch. 121, 717–729. doi:10.1557/PROC-121-717.

Shi, W., Anderson, M.J., Tulkoff, J.B., Kennedy, B.S., Boreyko, J.B., 2018. Flow harvesting with harps. ACS Appl. Mater. Interfaces 10, 11979–11986. doi:10.1021/acsami.7b17488.

Shi, Z., Jiang, F., Andersson, H.I., Strandenes, H., 2019. On simulation of particle-laden wake flow. In: MekIT19 Tenth National Conference on Computational Mechanics. International Center for Numerical Methods in Engineering (CIMNE), pp. 407–418.

Su, S.-W., Lai, M.-C., Lin, C.-A., 2007. An immersed boundary technique for simulating complex flows with rigid boundary. Comput. Fluids 36, 313–324. doi:10.1016/j.compfluid.2005.09.004.

Sumbekova, S., Cartellier, A., Aliseda, A., Bourgoin, M., 2017. Preferential concentration of inertial sub-Kolmogorov particles: the roles of mass loading of particles, Stokes numbers, and Reynolds numbers. Phys. Rev. Fluids 2, 024302. doi:10.1103/PhysRevFluids.2.024302.

Tagawa, Y., Mercado, J.M., Prakash, V., Calzavarini, E., Sun, C., Lohse, D., 2012. Three-dimensional Lagrangian Voronoï analysis for clustering of particles and bubbles in turbulence. J. Fluid Mech. 693, 201–215. doi:10.1017/jfm.2011.510.

Tang, L., Wen, F., Yang, Y., Crowe, C.T., Chung, J.N., Troutt, T.R., 1992. Self-organizing particle dispersion mechanism in a plane wake. Phys. Fluids 4, 2244–2251. doi:10.1063/1.858465.

Tom, J., Bragg, A.D., 2019. Multiscale preferential sweeping of particles settling in turbulence. J. Fluid Mech. 871, 244–270. doi:10.1017/jfm.2019.337.

Tseng, Y.-H., Ferziger, J.H., 2003. A ghost-cell immersed boundary method for flow in complex geometry. J. Comput. Phys. 192, 593–623. doi:10.1016/j.jcp.2003.07.024.

Uhlmann, M., 2008. Interface-resolved direct numerical simulation of vertical particulate channel flow in the turbulent regime. Phys. Fluids 20, 053305. doi:10.1063/1.2912459.

Vallée, R., Henry, C., Hachem, E., Bec, J., 2018. Inelastic accretion of inertial particles by a towed sphere. Phys. Rev. Fluids 3, 024303. doi:10.1103/PhysRevFluids.3.024303.

Wassgren, C.R., Cordova, J.A., Zenit, R., Karion, A., 2003. Dilute granular flow around an immersed cylinder. Phys. Fluids 15, 3318–3330. doi:10.1063/1.1608937.

Williamson, C.H.K., 1996. Vortex dynamics in the cylinder wake. Annu. Rev. Fluid. Mech. 28, 477–539. doi:10.1146/annurev.fl.28.010196.002401.

Wood, A.M., Hwang, W., Eaton, J.K., 2005. Preferential concentration of particles in homogeneous and isotropic turbulence. Int. J. Multiph. Flow 31, 1220–1230. doi:10.1016/j.ijmultiphaseflow.2005.07.001.

Yang, Y., Crowe, C.T., Chung, J.N., Troutt, T.R., 2000. Experiments on particle dispersion in a plane wake. Int. J. Multiph.. Flow 26, 1583–1607. doi:10.1016/S0301-9322(99)00105-6.

Zdravkovich, M.M., 1997. Flow Around Circular Cylinders. Volume I: Fundamentals. Oxford University Press, Oxford.

Zhao, L., Andersson, H.I., Gillissen, J.J.J., 2010. Turbulence modulation and drag reduction by spherical particles. Phys. Fluids 22, 081702. doi:10.1063/1.3478308.

Zhou, H., Mo, G., Cen, K., 2011. Numerical investigation of dispersed gas-solid two-phase flow around a circular cylinder using lattice Boltzmann method. Comput. Fluids 52, 130–138. doi:10.1016/j.compfluid.2011.09.007.

Article III

Clusters and coherent voids in particle-laden wake flow

Zhaoyu Shi, Fengjian Jiang, Lihao Zhao, Helge I. Andersson

International Journal of Multiphase Flow, Vol 141, 103678, 2021

International Journal of Multiphase Flow 141 (2021) 103678

Contents lists available at ScienceDirect

International Journal of Multiphase Flow

journal homepage: www.elsevier.com/locate/ijmulflow

Clusters and coherent voids in particle-laden wake flow

Zhaoyu Shi [a], Fengjian Jiang [b,*], Lihao Zhao [c,a], Helge I Andersson [a]

[a] Department of Energy and Process Engineering, Norwegian University of Science and Technology, 7491 Trondheim, Norway
[b] Department of Ships and Ocean Structures, SINTEF Ocean, 7052 Trondheim, Norway
[c] AML, Department of Engineering Mechanics, Tsinghua University, 100084 Beijing, China

ARTICLE INFO

Article history:
Received 25 January 2021
Revised 10 April 2021
Accepted 26 April 2021
Available online 3 May 2021

Keywords:
Coherent voids
Smooth edges
Cylinder wake flow
Numerical simulation

ABSTRACT

Inertial point particles suspended in a two-dimensional unsteady circular cylinder flow at $Re = 100$ are studied by one-way coupled three-dimensional numerical simulations. The striking clustering pattern in the near-wake is strongly correlated with the periodically shed Kármán vortex cells. The particles are expelled from the vortex cores due to the centrifugal mechanism and coherent voids encompassing the local Kármán cells are therefore observed. The particle clustering at the upstream side of each void hole form a smooth edge, where the particle velocity magnitude is consistently lower than at the downstream edge of the voids. The trajectories of these particles originate from the side of the cylinder where the sign of vorticity is opposite to that of the vortex encompassed by the corresponding void hole. The particles are seen to decelerate along a substantial part of their trajectories. Particle inertia is parameterized by means of a Stokes number Sk and smooth edges around the void holes still exist when Sk is increased, although their formation is delayed due to larger inertia. Increasing inertia contributes to a decoupling of the particle acceleration from the slip velocity, which almost coincided at $Sk = 1$.

1. Introduction

Particle-laden flows around natural obstacles and man-made bluff bodies are frequently encountered in nature and industry. Even though the entering flow is regular and smooth, the fluid motion in the wake of the obstacle becomes more complex and comprises a variety of characteristic length and time scales. Insight in particle transportation and dispersion mechanisms in common bluff-body wakes may promote mitigation of industrial pollution and a better understanding of natural phenomena, such as scouring around offshore wind turbine foundations and clogging of steam generators in nuclear power plants at large scales, as well as enhancing the mixing performance of microfluidic reactors at small scales. Particularly, microfluidic systems are commonly applied in the lab-on-a-chip biological devices, wherein the flows are almost always laminar defined by a tiny pore scale. A number of experimental and numerical studies investigated the microparticle suspensions, e.g. particle migration and trapping in microchannels (Lee et al., 2010; Gijs et al., 2010; Dressaire and Sauret, 2017). The mixing or demixing processes can be manipulated with the fundamental insights of general particle-laden laminar vortex flows. The current understanding of the behavior of inertial particles even in the simplest bluff-body wakes is incomplete and no clue exists to how the remarkable particle clustering patterns arise.

Besides the occurrence of particle-laden wake flows in a variety of different settings, particle additives play a crucial role in dye and smoke flow visualizations. Cimbala et al. (1988) utilized a smoke-wire visualization technique to explore the wake formed behind a circular cylinder at relatively low Reynolds numbers. They aimed to investigate the far-wake behavior but realized that particles released from a smoke-wire retained a cellular pattern long after the characteristic Kármán vortices have largely diffused. This observation was interpreted as an inertia effect of particles since smoke in air is composed of tiny aerosol-type particles whose mass is significantly greater than the mass of the surrounding air molecules. The persistent smoke pattern showed that diffusion of smoke aerosols is extremely slow and the effective Schmidt number, i.e. the ratio of viscous diffusivity to the diffusivity of smoke particles in air, is orders of magnitude larger than unity. The tiny smoke particles do therefore not act as passive tracers and we believe that the effect of particle inertia can be understood in terms of a particle Stokes number rather than being lumped into an effective Schmidt number. The Stokes number (Sk) is adopted as a measure of particle inertia, typically defined as the ratio between the particle relaxation time τ_p and a characteristic time scale τ_f of the flow.

* Corresponding author.
E-mail address: Fengjian.Jiang@sintef.no (F. Jiang).

https://doi.org/10.1016/j.ijmultiphaseflow.2021.103678

The pioneering work by Jung et al. (1993) traced infinitesimal passive particles in an analytical two-dimensional (2D) wake flow behind a circular cylinder and analytically studied the importance of boundary conditions (BCs) to the particles' periodic orbits in the recirculation region. The follow-up study by Benczik et al., (2002) considered the motion of finite-size particles and manifested a sensitivity of inertia for particle trapping in a laminar cylinder wake flow. The seminal work by Tang et al. (1992) demonstrated patterns of rigid particle dispersion in a simulated mixing-layer and a plane wake. The behavior of these highly-organized particles, i.e. *particle clustering*, manifested a strong dependence on Stokes number and the large-scale flow structures (LSS) in a variety of configurations.

Experiments by Yang et al. (2000) showed snapshots of particle distributions for two different particle sizes, for which particles with *Sk* of order unity were observed to present the most distinctive pattern. In another perturbation study with the Stokes drag force parameterized as a small disturbance, Burns et al. (1999) discussed the presence of a periodic attractor in a Kármán vortex street modeled as point vortices. The so-called dynamical attractor appeared as an indicator of particle focusing. Haller and Sapsis (2008) extended the scope to finite-size particles and constructed a slow manifold to describe the asymptotic attraction along trajectories of low-*Sk* particles. Burger et al., (2006) compared the one-way and two-way coupled results in an oscillating hot-air circular cylinder wake flow at laminar condition by direct numerical simulations (DNSs). Afterwards, Yao et al. (2009) and Luo et al. (2009) also performed DNSs of a circular cylinder wake flow and presented clustering patterns in a better-resolved wake. The flow field exhibited vortices of different scales, determined by Reynolds number *Re*, which significantly affected the way of instantaneous particle clustering. A subsequent work (Zhou et al., 2011) additionally showed the temporal development of the particle distributions at a benchmarking $Re = 100$. Although the focus of Haugen and Kragset (2010) and more recent work by Aarnes et al. (2019) was on particle-cylinder impaction, glimpses of particle dispersion patterns in the near wake at $Re = 100$ were also presented.

Numerous efforts have been made in explorations of the underlying physical mechanisms of particle clustering, for instance in the paradigmatic homogeneous isotropic turbulence (HIT) and wall-bounded flows. The centrifugal effect induced by local vortices was recognized to interpret the tendency of particle clustering in strain-dominant regions (Squires and Eaton, 1991). This *strain-vorticity-selection* mechanism also applies in mixing-layers and shear flows (Eaton and Fessler, 1994). Previous numerical and experimental observations in HIT showed that the maximum clustering appeared at a Stokes number (Sk_η) based on the Kolmogorov time scale τ_η close to unity (Wang and Maxey, 1993; Aliseda et al., 2002; Salazar et al., 2008; Petersen et al., 2019).

The same optimal Stokes number for the maximum clustering was also reported for channel flow (Kulick et al., 1994) and wake flow behind a thick plane (Tang et al., 1992; Yang et al., 2000). The explanation of vortex ejection at the dissipative scales can also be extended to the inertial range and affected by self-similar multi-scale eddies (Yoshimoto and Goto, 2007; Bec et al., 2007). However, the centrifugal mechanism as the only effect fails for Sk_η substantially larger than unity. Goto and Vassilicos (2008) proposed an alternative explanation for particles with moderate Stokes number, i.e. the *sweep-stick* mechanism. This process suggests that particles preferentially concentrate in regions with low fluid acceleration instead of low vorticity both in 2D and 3D (Coleman and Vassilicos, 2009). Additionally, Bragg and Collins, (2014) carefully compared other potential factors accounting for the cluster formation at a broad-scale spectrum, in which a statistical model (Zaichik and Alipchenkov, 2007) based on radial distribution functions (RDFs) in phase space emphasized the history effect of particle inertia along the trajectories. Bagheri and Sabzpooshani, (2020) recently investigated the role of history force on particle clustering in a 2D von Kármán flow and found the enhanced clustering at high *Sk*. Today it is commonly acknowledged that the centrifugal mechanism correlated to local flow structures is dominant up to $Sk \approx 1$, while other non-centrifugal mechanisms also have to be taken into account at higher Stokes numbers.

In contrast to the systematic investigations of particle clustering in HIT, little is known about the clustering mechanisms in *laminar* vortex-dominated flows, like for example the time-periodic Kármán vortex street and the time-evolving Taylor-Green vortex (TGV) flow. One may wonder whether the abovementioned mechanisms are acting also in these and other non-turbulent flows. Tang et al. (1992) proposed a stretching-folding mechanism, but only for mixing-layer flows, in which particles tend to aggregate in the thin regions outlining the boundaries of the LSS, regarded as stretching process. The folding process is related to the vortex pairing (Wen et al., 1992). This interpretation is still ambiguous and not applicable to cylinder wake flows. Raju and Meiburg (1997) indicated the action of centrifugal ejection in analytical models of a 2D solid-body vortex and a point vortex. The centrifugal force pointing outwards from the vortex core opposes other forces until an optimal ejection rate is reached. Candelier et al. (2004) highlighted another dissipative effect of the history force on particle trajectories which influenced the ejection rate in simple flows. Daitche and Tél (2011, 2014) improved the analysis in a modeled Kármán vortex flow and explicitly pointed out the suppression of concentration or attraction due to the history force for finite-size inertial particles (e.g. bubbles, oil droplets). However, these studies on clustering mechanisms are based on simplified and 2D flows, the explorations on real-life 3D vortex flows are still scarce. Recently, Jayaram et al. (2020) studied particle clustering in an evolving TGV flow and observed clustering in strain-rate dominated areas after the LSSs had been broken down to small-scale eddies so that an effective Stokes number, based on the viscous dissipation time scale, became of order unity.

To objectively characterize particle clustering, quantitative measurements of clustering have been escalated from box counting (Aliseda et al., 2002), correlation dimension (Tang et al., 1992; Bec et al., 2007), RDFs (Zaichik and Alipchenkov, 2007; Ireland et al., 2016) to Voronoï diagrams (Monchaux et al., 2010). The two latter ones are currently the most widely used approaches, of which a RDF is spatially-averaged for each manually selected length-scale and thus fails to provide information of individual clusters. By contrast, information about instantaneous local clustering is accessible via Voronoï diagrams for which the number of particles should be carefully chosen in terms of statistical analysis. A recent experimental HIT study by Petersen et al. (2019) found high consistency between the two approaches. Mohammadreza and Bragg (2020) extensively applied Voronoï cells to investigate the effects of *Re* and gravity on clustering in HIT using DNS. Moreover, Shi et al. (2020) applied Voronoï diagrams to analyze a striking bow-shock clustering in the vicinity of a circular cylinder. Alternative dynamical techniques, such as finite-time Lyapunov exponents (Bec et al., 2006a; Jacobs and Armstrong, 2009; Daitche and Tél, 2014) and acceleration analysis (Bec et al., 2006b), which rely on particle trajectories, are mainly effective for particles with modest inertia, i.e. small Sk. Another approach is based on the application of an Eulerian velocity-acceleration structure function (Gibert et al., 2012), showing the tendency of clustering in high-strain regions. The review article by Monchaux et al. (2012) provides a comprehensive overview of the different techniques used to characterize particle clustering.

The motivation of the present study is to investigate clustering of heavy inertial particles in the near wake of a circular cylinder

flow at $Re = 100$. Of particular interest is to provide an in-depth exploration of a striking phenomenon, namely the formation of *coherent voids*, and how and why these voids are bounded by a *smooth edge* consisting of densely concentrated particles. This phenomenon is not a numerical artifact but a reality of practical interest, for instance with respect to homogenization of particle additives. The phenomenon has been observed before in some numerical simulation studies (Yao et al., 2009; Haugen and Kragset, 2010; Aarnes et al., 2019), but been left almost unnoticed and without being scrutinized. Therefore a couple of questions remain to be answered: why and how do particle clustering appear in a laminar Kármán vortex street? How do the characteristic coherent voids form and evolve in space and time? How are the particle structures correlated with the local vortices? These questions will be addressed in the present paper which can be considered as a sequel to the differently focused paper by Shi et al. (2020).

The paper is organized as follows: the mathematical problem, the simulation method and numerical details are first described in Section 2. Results for $Sk = 1$ particles are presented and discussed in three sub-sections. The traveling features of the coherent voids and their smooth edges are considered in sub-sections 3.1 and 3.2, respectively, whereas the key observations made from particle trajectories are addressed in 3.3, in terms of both group and individual trajectories. Finally, in order to elucidate the crucial role of particle inertia, comparisons of results obtained for some different Stokes numbers are made in Section 4, before conclusions are drawn in Section 5.

2. Problem formulation and numerical methods

2.1. Equations of motions

Three-dimensional numerical simulations of flow around a circular cylinder at Reynolds number $Re = U_0 D/\nu = 100$ (free stream velocity U_0, cylinder diameter D, kinematic viscosity ν) are conducted using a well-verified DNS/LES solver called MGLET (Manhart et al., 2001; Manhart and Friedrich, 2002). We utilize a second-order finite-volume method to discretize the incompressible continuity and Navier-Stokes (N-S) equations. The transient flow is time-advanced by an explicit low-storage third-order Runge-Kutta scheme. The instantaneous fluid velocity components and pressure are preserved in discrete staggered equidistant cubic Cartesian grids. One-way coupling is deployed, i.e. the particle movement does not affect the underlying fluid velocity and particle-particle collision is neglected. The Poisson equation is iteratively solved by Stone's strongly implicit procedure. We exploit a cut-cell immersed boundary method (CCIBM) to exactly compute the shapes of polyhedron cells intersected by the curved cylinder wall. The normal vector of the intersected cells is obtained to define the particle-wall collision boundary condition.

The inertial particles laden in the unsteady laminar wake flow are modeled as point-like spheres with radius a in a dilute suspension. The density ratio ρ_p/ρ_f is taken as 10^3 (ρ_p, ρ_f are the densities of particle and fluid, respectively), and gravity is neglected since we only intend to investigate the inertial effect in this work. The individual particles are only under the effect of drag force

$$\boldsymbol{F} = 6\pi\,\mu a\beta[\boldsymbol{u}_{f@p} - \boldsymbol{u}_p(\boldsymbol{x}_p, t)], \tag{1}$$

which results from the *slip velocity* $\boldsymbol{U}_s = \boldsymbol{u}_{f@p} - \boldsymbol{u}_p(\boldsymbol{x}_p, t)$. Herein, $\boldsymbol{u}_{f@p}$ is the local fluid velocity at particle position $\boldsymbol{x}_p$. The empirical correction factor $\beta = C_D Re_p/24$ is unity in the Stokesian limit $Re_p = 0$, where $Re_p = 2a||\boldsymbol{u}_p - \boldsymbol{u}_{f@p}||/\nu$ is the particle Reynolds number. The modified finite-Re_p drag coefficient C_D is a function of Re_p estimated as

$$C_D = \frac{24}{Re_p}(1 + 0.15Re_p^{0.687}) + \frac{0.42}{1 + 4.25\times 10^4 Re_p^{-1.16}} \tag{2}$$

Table 1
The average particle Reynolds number $\langle Re_p\rangle$ and peak value $Re_{p,m}$ for each Sk at time t^*.

Sk	1	3	5	8	12	16
Average $\langle Re_p\rangle$	0.092	0.258	0.472	0.718	1.001	1.323
Maximum $Re_{p,m}$	0.833	1.859	2.834	3.796	4.797	5.798

for $Re_p < 3\times 10^5$ (Cliff et al., 1978, Chapter 5). The empirical drag law Eq. (2) is well-justified under a steady uniform flow at moderate Re_p (from 1 up to 10^3) (Bagchi and Balachandar, 2003). From a practical perspective, Eq. (1) is also widespread in most known studies. The simplified Maxey-Riley (M-R) equations (Maxey and Riley, 1983) give us the Lagrangian particle information as such,

$$\boldsymbol{a}_p = \frac{d\boldsymbol{u}_p}{dt} = \frac{C_D Re_p}{24\tau_p}(\boldsymbol{u}_{f@p} - \boldsymbol{u}_p), \quad \frac{d\boldsymbol{x}_p}{dt} = \boldsymbol{u}_p. \tag{3}$$

where $\boldsymbol{a}_p$ is the particle acceleration. The particle velocity $\boldsymbol{u}_p$ is updated by an adaptive fourth-order Rosenbrock-Wanner scheme with a third-order error estimator (Gobert, 2010) and an explicit Euler scheme is used to update particle position $\boldsymbol{x}_p$. The particle equations are integrated forward in time with the same time step used in solving the N-S equations. The local fluid velocity components are obtained by a linear interpolation. A measure of particle inertia is defined as $Sk = \tau_p/\tau_f$, where $\tau_p = 2\rho_p a^2/9\rho_f\nu$ is the particle response time to changes in the local fluid velocity and $\tau_f = D/U_0$ denotes the nominal time scale of the flow field. An alternative timescale of the fluid field associated with Kármán vortices can be defined as the inverse of the maximum absolute spanwise vorticity, i.e. $\tau_{f\nu} = 1/|\omega_z|$. We believe that this vorticity-based time scale is physically more relevant than the time scale of the vortex shedding. An 'effective Stokes number' based on this vorticity-time scale is thus defined as $Sk_e = \tau_p/\tau_{f\nu} = |\omega_z|\tau_p$, where $|\omega_z|$ decays downstream. In other words, for such single dominating timescale flow, it is only a scaling matter whether to present the results with an effective or the nominal Sk number and the observed physics are not going to be affected by the choice of timescale. Table 1 shows both the average and peak value of Re_p obtained from samples within $[-0.5D, 15.8D]$ along streamwise X-direction. Nevertheless Re_p increases as Sk is larger, the maximum Re_p is only 5.8 for all considered Sk-numbers computed from the relatively small slip velocity $\boldsymbol{U}_s$. This indicates the applicability of the finite-Re_p correction in Eq. (2). Note that we adopt a 'sliding motion' collision model at the surface of the cylinder, wherein the particle wall-normal velocity reduces to zero while the wall-tangential velocity component preserves, details of which are reported in the recent work by Shi et al. (2020).

2.2. Computational details

We consider a cuboid box discretized by a multi-level structured Cartesian mesh, in each of which N^3 cubic cells are uniformly distributed. The range of the computational domain is $[-16.384D, 16.384D]$ in the streamwise X-direction, $[-8.192D, 8.192D]$ in the crossflow Y-direction and $[0, 4.096D]$ in the spanwise Z-direction. The center of the cylinder sits at (X=0, Y=0). A local grid refinement is enforced in the vicinity of the cylinder and the total number of grid points are around 1.65×10^7 with a resolution of $\Delta_{\min}/D = 0.016$. The discrete N-S equations are integrated in time and space on this grid configuration. A periodic boundary condition is imposed in the homogeneous Z-direction. A constant free-stream velocity condition and Neumann condition on pressure $\partial p/\partial x = 0$ are applied at the inlet plane. The outlet BC contains zero pressure and $\partial u/\partial x = \partial v/\partial x = \partial w/\partial x = 0$. Free-slip BCs are enforced at the two side-walls normal to Y-direction, i.e. $v = 0$ and $\partial u/\partial y = \partial w/\partial y = 0$.

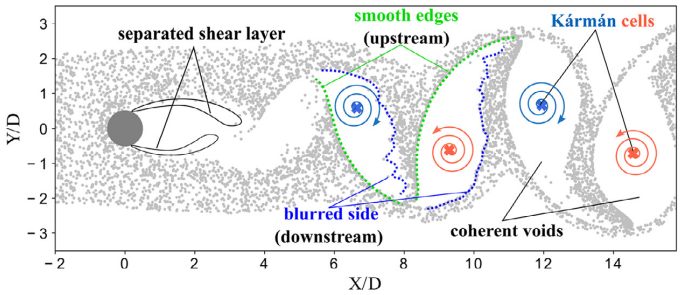

Fig. 1. (color online) Schematic of the instantaneous particle field with superimposed blue and red whirls illustrating oppositely rotating Kármán vortex cells. (For interpretation of the references to colour in this figure legend, the reader is referred to the web version of this article.)

Table 2
Particle simulation framework for each *Sk* in two groups.

Case no.	Injected particle (Y/D)×(Z/D) number per timestep	Injection area	Sample region (X/D)	Sample number in total
1	9	(−4.096, 4.096)×(0, 2.048)	(−2.5, 15.8)	4.7×10^4
2	2	(−2.048, 2.048)×(0, 1.024)	(−2.5, 16.5)	6.1×10^3

After running the simulation for $400\tau_f$, the unsteady flow has developed into a strictly periodic vortex shedding regime. The time-averaged drag coefficient $C_d = 2F_d/\rho_f U_0^2 LD$ and standard deviation of the lift-coefficient $C_{l-rms} = 2F_{l-rms}/\rho_f U_0^2 LD$ (F_d drag force, F_{l-rms} root-mean-square lift force, L cylinder length) are obtained to be 1.391 and 0.240, respectively. The Strouhal number $St = f\tau_f$ is calculated as 0.168 via fast Fourier transformation (FFT). The measured parameters are all within the ranges reported by others, see Ferziger and Tseng (2003). In a post-processing step, we deduced the spanwise vorticity ω_z from the computed velocity components as $\omega_z = \partial v/\partial x - \partial u/\partial y$. The identification of a vortex employed here, according to the *Q-criterion* (Hunt et al., 1988), is a spatial region where the second invariant of the velocity gradient tensor $Q = \frac{1}{2}(|\boldsymbol{\Omega}|^2 - |\boldsymbol{S}|^2)$ is positive ($\boldsymbol{\Omega} = \frac{1}{2}[\nabla \boldsymbol{u} - (\nabla \boldsymbol{u})^T]$ and $\boldsymbol{S} = \frac{1}{2}[\nabla \boldsymbol{u} + (\nabla \boldsymbol{u})^T]$ are the rotation-rate tensor and strain-rate tensor, respectively).

Inertial particles are seeded into the flow from the inlet at initial velocity U_0. The particle simulation, starting at $400\tau_f$, lasts 8 vortex shedding periods (total number of timesteps 9448). At each timestep $i_{step} = 1, 2, \ldots, 9448$, a certain number of new particles are released into the flow and others are leaving the domain through the outlet. Fig. 1 shows the snapshot of the particle distribution and the extracted vortex cores from DNS data at the last timestep $i_{step} = 9448$. The terminology used afterwards are depicted along with the corresponding schematic topology.

Six different Stokes numbers are considered, i.e. $Sk = 1, 3, 5, 8, 12, 16$. Unlike the tracer particles approaching the cylinder wall without colliding, inertial particles lose part of their kinetic energy due to collision with the cylinder surface. We perform two groups of particle simulations with different seedings shown in Table 2. The first case serves for the purpose to exhibit the particle clustering with the sufficient samples used in Sec 3.1 and 3.2. In the second simulation, we intend to output the essential quantities along each particle trajectory at every timestep. The heavy dataset requires to reduce the number of injected particles, therefore, the injection area is only a quarter of that in the first simulation. In the post-processing, we only select the useful particle samples along the streamwise X-direction which are near the cylinder and involved with vortices in the wake. The total particle numbers of the two cases used for statistical analysis in Sec 3.3, are different by a factor of 8.

3. Results and discussion

3.1. Traveling of 'void holes'

The instantaneous particle concentration seen in Fig. 1 exhibits a peculiar repetitive pattern, which intuitively reflects the underlying Kármán vortex street. The characteristic concentration pattern of the $Sk = 1$ particles will be thoroughly explored in the next three sub-sections with focus on the formation and propagation of the void holes (empty areas). Before the closing of the paper, Stokes number effects will be addressed in Section 4. Since the flow at $Re = 100$ is two-dimensional and two-componential, i.e. the only two velocity components u and v are independent of Z, all particles are projected into a single XY-plane. Fig. 2 shows how void holes form in the shadow of the cylinder and travel downstream during one shedding period $T = D/(St \cdot U_0) \approx 6D/U_0$, starting at time $t^* \approx 47D/U_0$, i.e. about 8 shedding periods after the start of the particle seeding. Five leaf-shaped void holes, labeled from 0 to 4, can be seen in the uppermost panel at time t^*. Each of the void holes are partially overlapping with a local vortex cell, visualized by means of the spanwise vorticity ω_z. Consecutive snapshots, separated $T/8$ in time, are shown in the subsequent plots, in which we focus on the motion and shape of hole no 1. The shape of the void hole is approximated by a leaf-shaped contour (in cyan) of which the centroid is indicated by a cross. We observe that the void hole translates downstream with negligible lateral excursions. The void hole becomes more upright with time, which represents a very modest clockwise rotation, i.e. in the same sense as the rotation of the underlying Kármán vortex. The upper part of the periphery of the hole becomes more rounded, whereas the lower cusp becomes peakier. The length of the perimeter of hole no 1 increases by ca 35% during the shedding period considered, thus reflecting the increasing area of the void. A possible void distortion likely caused by an insufficient blockage ratio $\alpha = L_y/D$ can thus be excluded in view of the almost proportional increase of perimeter and area. After a half shedding cycle the topology of the concentration pattern exhibits a mirror-symmetry with respect to the X-axis of that of the original pattern at t^*. After a complete shedding cycle T, the void hole no 1 has translated to the earlier position of void hole no 3, whereas void hole no -1 has taken over the original position of void hole no 1.

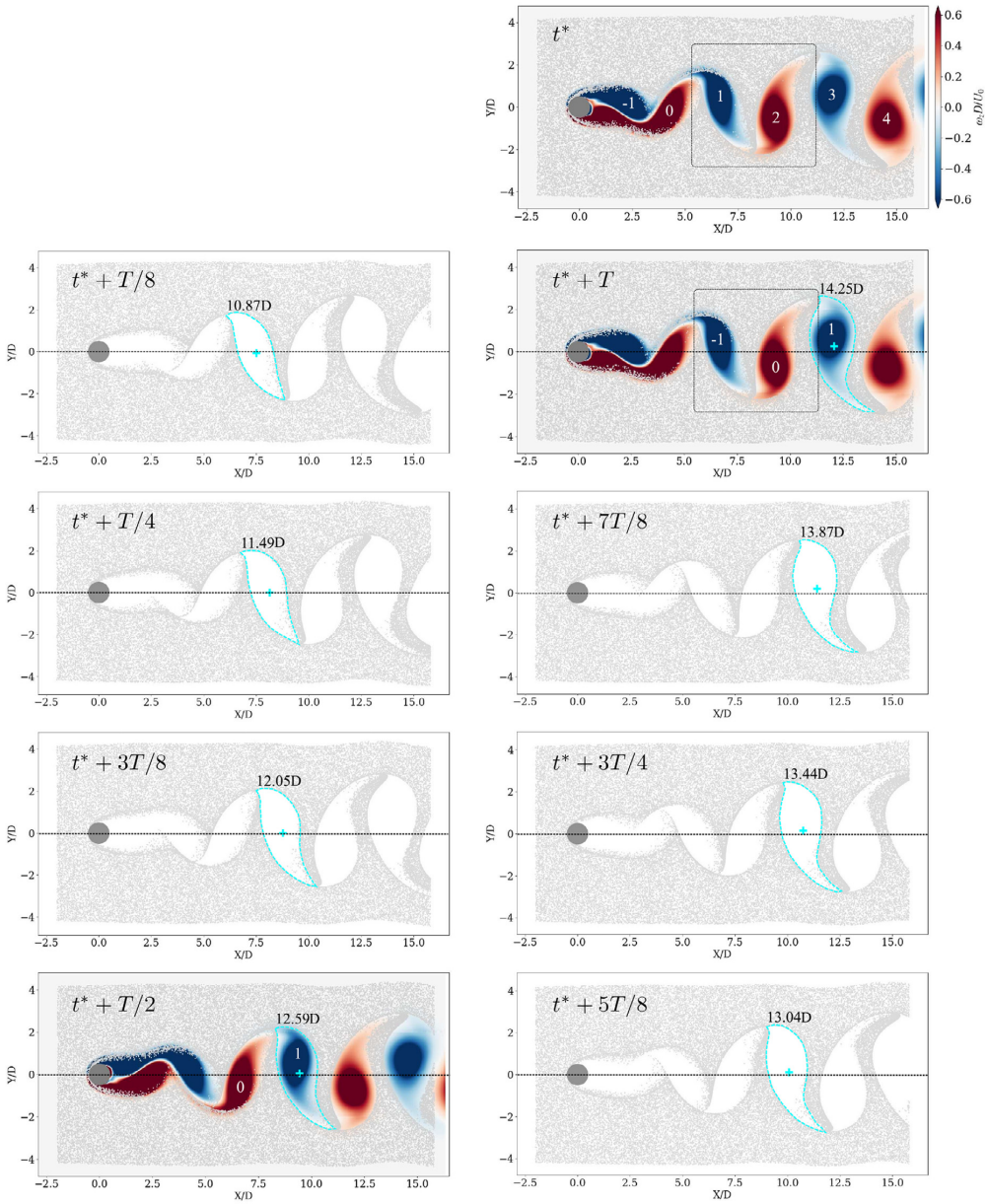

Fig. 2. (color online) Time-sequence of particle distributions during one vortex shedding period T. The characteristic snapshots of the clustering patterns of $Sk = 1$ particles are $T/8$ apart in time. The approximate outline and the centroid (+) of hole no 1 are colored in cyan and the perimeter is indicated at the top. The spanwise vorticity field $\omega_z D/U_0$ is superimposed on the particle distributions at time t^*, $t^* + T/2$ and $t^* + T$.

Let us now take a closer look at how the void holes travel in Fig. 3, where the fluid velocity field now is characterized by the scalar Q-field. The centers of Kármán vortices are marked by orange dots whose position is decided by the local maxima of Q, and the grey chunks represent fluid with $Q > 0$. Unlike the centroids of the void holes (black +), which translate downstream with negligible lateral excursions, the center of the anti-clockwise vortex associated with void hole no 0 is well below the Y-axis, whereas the center of the clockwise vortex cell corresponding to hole no 1 is above the symmetry plane. Although the void holes encompass the Kármán vortex cells, the centroid of a given hole does not coincide with the center of a Kármán vortex. This observation cannot readily be made from the Fig. 2. It is worth to note that the relative distance between the vortex core and the void centroid persists, i.e. that the vortex core remains most offset from the symmetry plane of the wake (Y=0). According to Fig. 3, however, the displacement

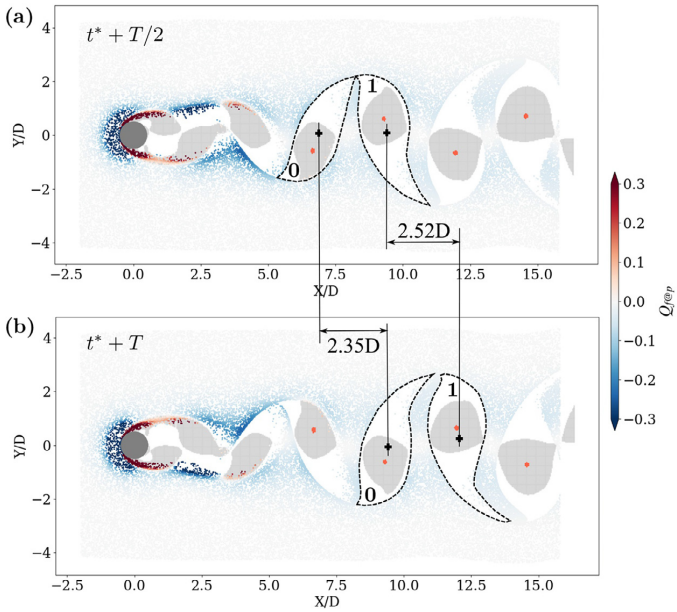

Fig. 3. (color online) Particle distributions and Q at time (a) $t^* + T/2$ and (b) $t^* + T$. The $Sk = 1$ particles are colored by the local value of Q, i.e. $Q_{f@p}$. The grey chunks inside the void holes represent parts of the flow field with $Q > 0$ and the orange dots show positions of local maxima of Q. The translational distance of the centroids (+) of void holes no 0 and no 1 can be measured over the time interval $T/2$. The numbering of the void holes refers to the top panel in Fig. 2.

between the vortex core and the void centroid decreases in the downstream direction, ca 10.2% and 22.1% for void no 0 and no 1, respectively, despite that the displacement at upstream is larger than that at downstream. The reason for the displacement diminishing with time is likely to be attributed to the gradually changing shape of the voids, which shifts the centroids closer to the vortex cores whereas the upstream void hole expands at a slower rate.

The particles have been colored by local Q at particle position, i.e. $Q_{f@p}$. The vast majority of the particles is bluish, which means that they are in a strain-rate dominated region characterized by negative Q-values. One can therefore infer that the $Sk = 1$ particles are expelled from the rotation-dominated Kármán vortex cells and swept to the borders of the void holes. However, it is surprising to observe the many reddish particles located in the two shear layers emanating from the surface of the cylinder. The centrifugal mechanism is active when an inertial particle tries to follow a curved trajectory whereas a particle in a separated shear layer follows a mildly curved path. That is why numerous particles can be seen in the shear layers, in spite of Q being positive. Here, positive $Q_{f@p}$ implies that the rotation rate exceeds the strain rate.

By measuring the traveling distance of the centroids of void hole no 0 and hole no 1 over the time interval $0.5T$ between the two plots, the translational speed of the two holes can be estimated as $0.796U_0$ and $0.854U_0$. The higher speed of hole no 1 reflects the monotonically decreasing velocity deficit with downstream distance X. This reduction of the velocity deficit and the accompanying attenuation of the strength of the vortex cores contribute to the persistent shape of the void holes. The traveling speed of the holes seems to be consistent with the estimated speed $0.895U_0$ of the Kármán vortex cells. The slightly lower traveling speed of the holes can be ascribed to the inertia of the $Sk = 1$ particles. The wavelength λ_x, i.e. the distance between two successive vortex cores with the same sign of ω_z, is about $5.284D$. These estimates of the vortex speed and separation are consistent with data reported from the DNS study by Mowlavi et al. (2016), albeit in presence of a somewhat insufficient blockage ratio in their computational set-up.

3.2. Tracking 'smooth edges'

An interesting phenomenon can be observed already from Fig. 2, namely that particles are densely clustered and form a smooth edge at the upstream side of the void holes. The particles are comparatively more dispersed around the downstream side of the void holes, and the edge of the hole is rather blurred near the cusp. Careful inspection of plots by others, notably (Yao et al., 2009; Haugen and Kragset, 2010) and (Aarnes et al., 2019), shows the same tendencies, but this peculiar phenomenon has neither been addressed nor explained before. To this end we introduce Voronoï diagrams in Fig. 4 to investigate the local particle concentration. The inverse of the area A of a Voronoï cell is a measure of the particle concentration. The leaf-shaped void holes comprise Voronoï cells which are order-of-magnitudes larger than the surrounding Voronoï cells. This cell pattern resembles reticulated veins with the thinnest cell-shape at the upstream (left) half of the void hole. These needle-like Voronoï cells result from the densely populated smooth edge of the void hole.

The particles in Fig. 4 are colored by local $Q_{f@p}/A$ in order to emphasize particles around the void holes better than in Fig. 2. No particles downstream of X=5D are seen to be in rotation-dominated ($Q > 0$) areas and the vast majority of the particles are in strain-dominated ($Q < 0$) areas. Particles near the center-plane ($Y = 0$) are greyish/white ($Q \approx 0$), i.e. neither affected by strain nor by rotation. Recall from Fig. 2 that the vorticity is negligible between the vortex cells and we can now infer that also the strain-rate is negligibly small in this area (between the wavy red-dashed lines).

How is the smooth edge of a void hole formed and maintained? Let us examine the history of the particles which form the smooth edge of holes no 3 and 4 at time t^*. The particles at the edge of

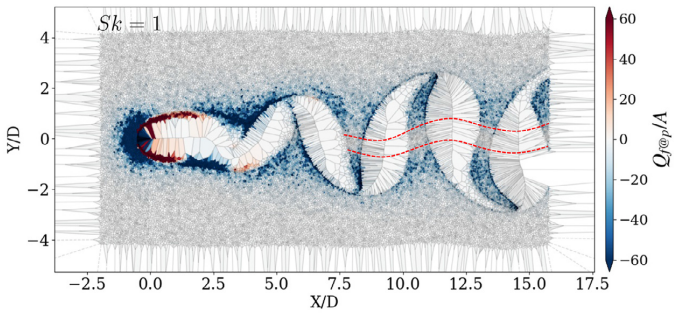

Fig. 4. (color online) Voronoï diagrams at time t^*. The $Sk = 1$ particles are colored by $Q_{f@p}/A$, where A is the area of the corresponding Voronoï cell. $Q_{f@p}/A \approx 0$ in the white band between the two undulating dashed red lines. (For interpretation of the references to colour in this figure legend, the reader is referred to the web version of this article.)

hole no 3 are backtracked in time and plotted in Fig. 5(a) at four earlier time instants $T/4$ apart. The fast-moving particles that make up the smooth edge of void hole no 3 (encompassing a clockwise-rotating Kármán vortex) seem to stem from the smooth edge of hole no 1, which now resides at the earlier position of void hole no 3. The particles, especially those forming the upper part of the smooth edge, seem to translate collectively almost as an ensemble. These particles are not only traveling in the streamwise direction but also translate upwards. This excess traveling distance requires a higher particle velocity magnitude $|\boldsymbol{u}_p|$, as seen by the dark-red colored particles. We believe that the excess velocity is provided by the clockwise-rotating Kármán vortex, which tends to accelerate not only the fluid but also the particles in the upper half of the vortex cell. Similarly, the fast-moving particles that make up the smooth edge of void no 4 (characterized by anti-clockwise vorticity) in Fig. 5(b) seem to stem from the smooth edge of void hole no 2, which is where void no 4 happened to be one shedding period T earlier. The particles that belong to the lower part of the smooth edge are deflected laterally, i.e. downwards, and accordingly move faster than the particles that belong to the upper part of the smooth edges and primarily translate in the X-direction. We are now able to choose a relevant vorticity strength connected with the property of smooth edges to define $Sk_e = |\omega_z|D/U_0 \cdot Sk$. The backtraces of a smooth edge shown in Fig. 5 verify that the expelled particles maintain their relative positions to the local vortex core during the convection once they undergo the most intensive centrifugal ejection around void 0 region. The vorticity maximum of the first detached vortex is thus reasonably used to define $Sk_e = 2.08Sk$, which also indicates a substantial inertial effect in accordance with the nominal Sk equal to unity.

A further look at the particles already examined in Fig. 5(b) is taken in Fig. 6, which shows the magnitude and direction of the acceleration $\boldsymbol{a}_p$ of the particles that make up the smooth edge of void hole no 4 at time t^*. Already one shedding period earlier, when these particles resided around the upstream edge of the present-time hole no 2, only the particles clustered around the lower part of the smooth edge exhibited a substantial acceleration $|\boldsymbol{a}_p|$ with a distinct component in the positive Y-direction. This is consistent with the relatively high velocities $|\boldsymbol{u}_p|$ of particles at the smooth edge of hole no 4. The significant component of $\boldsymbol{a}_p$ perpendicular to $\boldsymbol{u}_p$ suggests that these particles are deflected upwards, i.e. towards the symmetry plane of the wake.

Contrary to Fig. 6, in which the particles were backtracked in time, Fig. 7 shows the acceleration $\boldsymbol{a}_p$ of all particles at the same instant of time t^*. The magnitude of the particle acceleration decays with streamwise distance (the color changes gradually from blue to green). Particularly strong accelerations are seen on both sides of the void holes and most notably near the center of the corresponding Kármán vortices. These accelerations are towards downstream at the smooth edge but upstream at the blurred downstream side of each void hole. The reason that the acceleration vectors roughly point to the center of the Kármán vortex cells is in order to make the particles follow a circular trajectory around the vortex cores (orange dot). The high $|\boldsymbol{a}_p|$ exhibits similar undulations about the mid-plane (Y=0) as the white band in Fig. 4.

The slip velocity vector $\boldsymbol{U}_s$ determines the drag force $\boldsymbol{F}$ in Eq. (1) and therefore also the particle acceleration $\boldsymbol{a}_p$ in Eq. (3). The streamwise and cross-stream components of $\boldsymbol{U}_s$ are shown in Fig. 8, where the streamwise component $U_{s,x}$ in Fig. 8(a) alternates between positive and negative values, whereas the cross-stream component $U_{s,y}$ in Fig. 8(b) retains the same sign on a given side of the wake. One may notice that the two components of the slip velocity vector are of surprisingly similar magnitudes. This is the case because the primary cause of velocity slip is the Kármán vortex cells. A positive slip velocity component in Fig. 8(a) implies that the particles are lagging behind the fluid motion, while $U_{s,x} < 0$ represents particles leading the local fluid. This is fully consistent with the directions of the acceleration vectors on the two sides of the void holes in Fig. 7. The cross-stream slip velocity in Fig. 8(b) is consistently negative in the upper part of the wake (Y > 0), i.e. in the direction of negative Y. This reflects that the particles are moving faster towards the centerline in areas where a clockwise vortex gives rise to a negative fluid velocity component $u_y(x_p, t)$. See, for instance in Fig. 7, the densely populated bluish particles just downstream of void hole no 1 which encompasses a clockwise-rotating Kármán vortex. Similarly, we observe that $U_{s,y} > 0$ in the lower part of the wake. We therefore conclude that the cross-stream slip velocity tends to drive all particles towards the symmetry plane Y = 0.

3.3. Particle trajectories

3.3.1. Group trajectories

Now, after having examined the coherence of the void holes in the cylinder wake, we are shifting our attention to how inertial particles that cluster around a void hole are traveling through the Kármán vortex cells in the near wake. Fig. 9 shows the trajectories of particles landing on both sides of void hole no 2. The coherent voids appear where the first pair of counter-rotating Kármán cells are rolling up and detach from the separated shear layers. We observe from the upper trajectories in Fig. 9 that these particles were first accelerated as they passed the cylinder and the detached shear layer. Most of these trajectories were bent downwards by the first clockwise vortex that shed from the upper shear layer. The particles thereafter experienced a substantial deceleration, caused by an anti-clockwise Kármán vortex shed from the lower shear

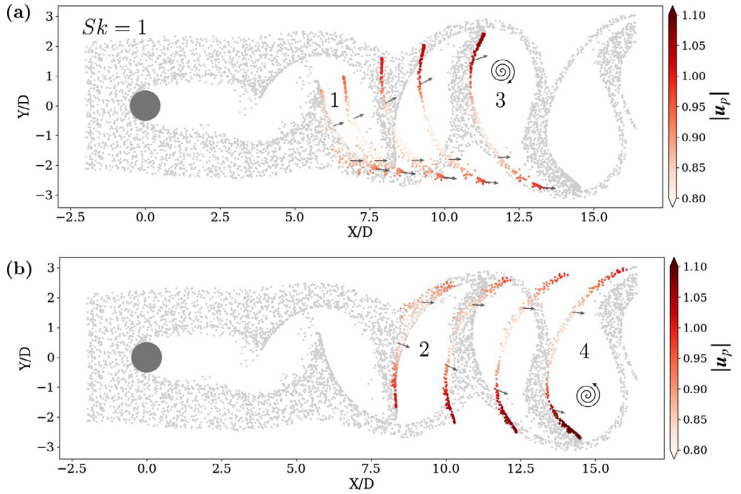

Fig. 5. (color online) Backtracking $Sk = 1$ particles that formed the smooth edge of void hole no 3 (a) and void hole no 4 (b) at t^* in time. The backtracked particles are colored by their velocity magnitude $|\boldsymbol{u}_p|$ at time t^*, whereas the grey particles are all at t^*. The earlier time instants are $T/4$ apart in (a) and separated by $T/3$ in panel (b). The arrows are particle velocity vectors.

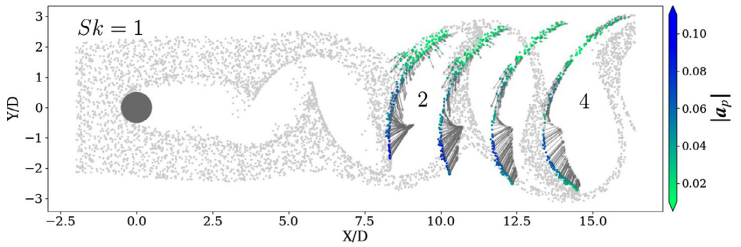

Fig. 6. (color online) Backtracking $Sk = 1$ particles that formed the smooth edge of void hole no 4 at t^* in time (same particles as in Fig. 5(b)). The backtracked particles are colored by their acceleration magnitude $|\boldsymbol{a}_p|$ at time t^*, whereas the grey particles all are at t^*. The earlier time instants are separated by $T/3$ in time. The arrows are particle acceleration vectors.

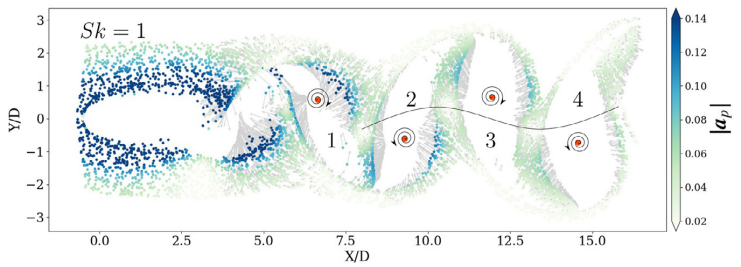

Fig. 7. (color online) Particle acceleration $\boldsymbol{a}_p$ at time t^*. The point particles are colored according to the magnitude $|\boldsymbol{a}_p|$ and a grey arrow represents the particle acceleration vector. An orange dot shows the position of local maximum of Q in the four vortex cores (embedded in void holes nos 1–4) and the whirls illustrate the sense of fluid rotation.

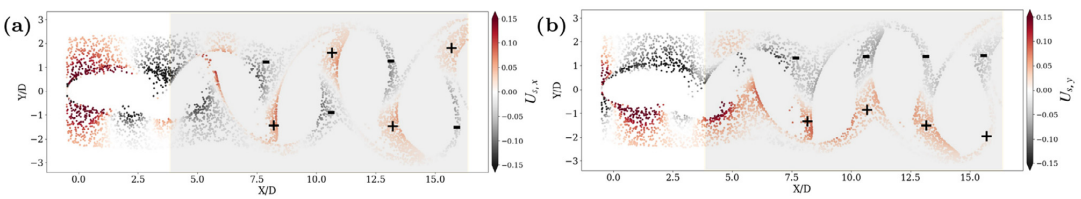

Fig. 8. (color online) Slip velocity $\boldsymbol{U}_s = \boldsymbol{u}_{f@p} - \boldsymbol{u}_p$ at time t^*. (a) Streamwise component $U_{s,x}$; (b) cross-stream component $U_{s,y}$; '+' and '-' denote areas with positive and negative dominance.

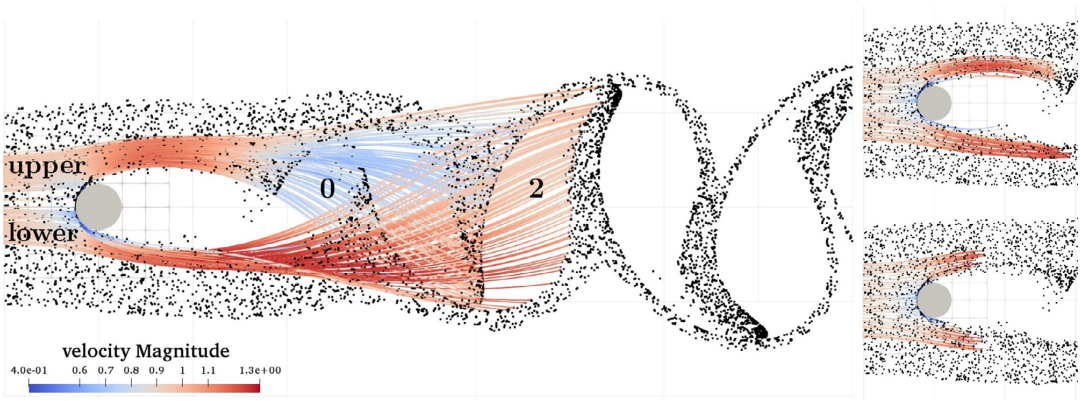

Fig. 9. (color online) Left: Trajectories of $Sk = 1$ particles landing on the upstream (smooth) and downstream (blurred) edges of void hole no 2 at time t^*, colored by the instantaneous particle velocity magnitude $|\boldsymbol{u}_p|$. The age ranges of particles terminating on upstream and downstream are [18.5, 26.1] and [26.2, 27.3] measured in D/U_0, respectively. The age of a particle is defined as the time elapsed since the particle was entered at the inflow boundary. Right: Trajectories of younger $Sk = 1$ particles with ages about $19.8D/U_0$ (upper panel) and $17.8D/U_0$ (lower panel).

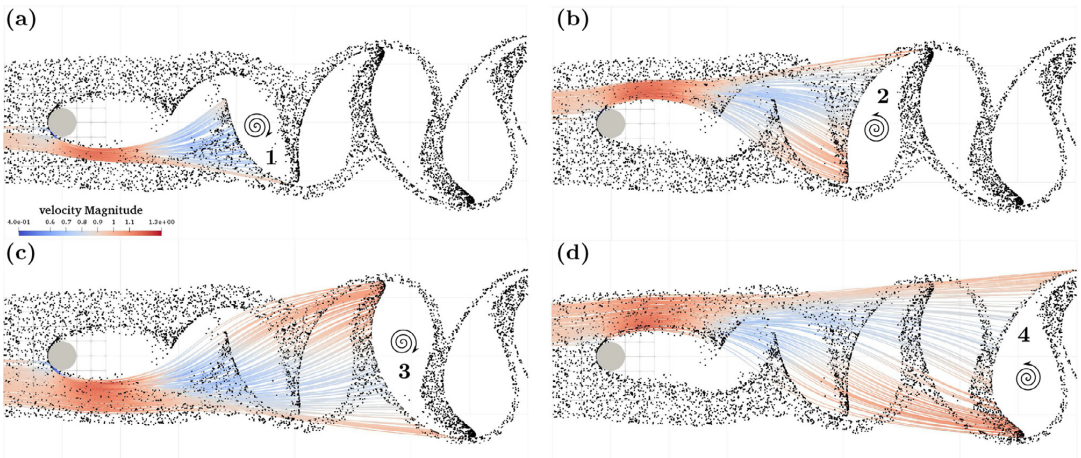

Fig. 10. (color online) Trajectories of $Sk = 1$ particles landing on the upstream smooth edge of a coherent void in the wake at time t^*. (a) void hole no 1; (b) hole no 2; (c) hole no 3; (d) hole no 4. The black dots show the particle distribution at time t^* and the colors represent the instantaneous particle velocity magnitude $|\boldsymbol{u}_p|$ along the trajectories ranging from 0.4 (blue) to 1.3 (red). The whirls illustrate the sense of vortex rotation. (For interpretation of the references to colour in this figure legend, the reader is referred to the web version of this article.)

layer, before the trajectories reached the smooth edge of void hole no 2 at time t^*. In contrast, particles passing below the cylinder maintained their high speed even during the stretch where the upper particles decelerated. Further downstream, however, the lower trajectories are bent upwards due to an anti-clockwise Kármán vortex, but these particles exhibited a more modest deceleration before they ended up at the downstream side of void hole no 2 at time t^*. Trajectories of younger particles, i.e. particles injected later than those tracked in the left panel, are shown to the right. As expected, the upper and lower trajectories remain symmetric about the midplane $Y = 0$ until void hole no 0 is approached. The particle velocity magnitude $|\boldsymbol{u}_p|$ is almost the same at both sides of the near wake until the particles start to be affected by the alternately shed vortex cells.

Next, we focus on group trajectories of the particles clustering at the smooth upstream edge of four different coherent voids at time t^*. The colored trajectories in Fig. 10 reveal a non-monotonic variation of the particle velocity $|\boldsymbol{u}_p|$, before the particles end up at the smooth edge of one of the void holes. Similar deceleration periods are seen in each of the four plots. Moreover, the deceleration sets in at roughly the same place in the wake, namely around the location of void hole no 0. This coincides with the position where the separated shear layers are rolling up into Kármán vortex cells; e.g. the formation of the anti-clockwise vortex embedded in void hole no 0 at time t^*, as shown in the uppermost plot in Fig. 2. However, the particle deceleration is apparently caused by an oppositely rotating Kármán vortex shed from the other side of the cylinder. This observation is supported by the observation that particles forming the central portion of the smooth edges experienced a longer period with relatively low velocity. Particles terminating near the cusp of the coherent voids are almost unaffected by the counter-rotating Kármán vortices and mostly retain their momentum along the almost straight trajectories. At the particular time instant t^*, particles clustering at the smooth edge of an odd-numbered void hole stem from the lower side of the cylinder, whereas those clustered at the upstream edge of even-numbered

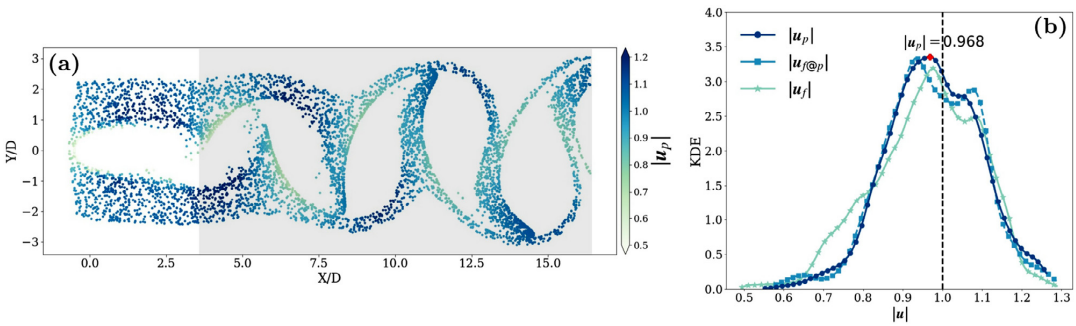

Fig. 11. (color online) (a) Particle velocity $\boldsymbol{u}_p$ at time t^*. The $Sk = 1$ particles are colored according to the magnitude $|\boldsymbol{u}_p|$; (b) KDE of the particle velocity magnitude $|\boldsymbol{u}_p|$ and the local fluid velocity magnitude $|\boldsymbol{u}_{f@p}|$ based on the particles in the shaded area X = [3.75D, 16.5D] in panel (a). The red cross denotes the major peak of the KDE of the particle velocity magnitude at $|\boldsymbol{u}_p| \approx 0.968$, whereas the average value is 0.977. (For interpretation of the references to colour in this figure legend, the reader is referred to the web version of this article.)

holes passed above the cylinder. In all cases, however, the trajectories bend towards the mid-plane Y = 0. The deflections of the particle trajectories are caused by the up-rolling vortex that just shed from the separated shear layer. In Fig. 10(a, c), for instance, the bending of the trajectories is due to the anti-clockwise vortex shed from the lower shear layer. As an immediate consequence, the inertial particles are entrained into the central part of the wake. It can finally be seen that the trajectories in Fig. 10(a) look like the first stretches of the trajectories in Fig. 10(c). This confirms the observation made from Fig. 5(a) that particles that clustered at the smooth edge of void hole no 3 could be tracked backwards T in time to coincide with the upstream edge of void hole no 1.

The Lagrangian particle trajectories shown in Fig. 10 revealed that most of the particles that clustered at the upstream smooth edge of one of the coherent voids at time t^* experienced a deceleration period in passing the very-near wake. To examine the imprint, if any, of the particles' history at the present time t^*, Fig. 11(a) shows the instantaneous particle velocity magnitude $|\boldsymbol{u}_p|$. Indeed, relatively low velocity magnitudes (greenish particles) are observed for the particles clustered around the smooth edges of the coherent voids. Kernel density estimation (KDE) of $|\boldsymbol{u}_p|$ in Fig. 11(b) exhibits a major peak at $|\boldsymbol{u}_p| = 0.968$, i.e. slightly below the average value 0.977. In contrast, the KDE of the local fluid velocity at the particle positions $|\boldsymbol{u}_{f@p}|$ has two peaks, both of which are separated from the $|\boldsymbol{u}_p|$-peak due to particle inertia.

3.3.2. Individual trajectories

The variations of the velocity of particles that cluster at both sides of a void hole seen in Fig. 10 are now explored further by means of trajectories of two particles released at the same time but landing at different sides of void hole no 3. The trajectories of the two particles are plotted in all panels of Fig. 12, to enable comparisons with the streamwise and cross-stream components of the slip velocity, particle velocity and particle acceleration. The coinciding variations of the slip velocity $\boldsymbol{U}_s$ and acceleration $\boldsymbol{a}_p$ components at this Stokes number ($Sk = 1$) suggest that the finite-Re correction factor β in Eq. (1) is close to unity.

We observe from Fig. 12(a, c) that both particles are decelerated as they are approaching the cylinder due to the adverse pressure gradient in the stagnation zone. Both particles start to accelerate at X $\approx -0.6D$ and attain maximum acceleration as they pass the shoulders of the cylinder. The particle passing below the cylinder (labeled P_{low}) decelerates again already from X $\approx +1.2D$ (light green dot) and is accordingly slowed down severely, until another mild acceleration sets in. The other particle passing above the cylinder (labeled P_{up}) experiences a longer acceleration period and accordingly achieves a relatively higher velocity before a stretch of deceleration. The deceleration stage of both particles, caused by the local Kármán vortices, extends over 4–5D. The particles are thereafter accelerated once again so that the streamwise particle velocity component $u_{p,x}$ recovers to approximately U_0 as the particles land on the respective edges of void hole no 3 at time t^*. The particles are now following the fluid more closely and the slip velocity $U_{s,x}$ and the acceleration $a_{p,x}$ are only modestly positive.

Contrary to the decreasing $u_{p,x}$ in front of the cylinder, the magnitude of the cross-stream particle velocity $u_{p,y}$ is rapidly increasing until X ≈ 0 where a sign-change of $a_{p,y}$ can be observed. Both particles continue to move away from the symmetry plane at Y = 0 for a little while, until $u_{p,y}$ changes sign at X $\approx 2D$. Thereafter, the particle (P_{low}) originating at the lower side of the cylinder is dragged by the fluid in the positive Y-direction, whereas the particle (P_{up}) passing above the cylinder is dragged in the opposite direction.

4. Stokes number effect

After having explored how inertial $Sk = 1$ particles are entrained into the wake and yet leave coherent voids, we finally take a brief look at how particles with higher inertia behave in the same unsteady wake flow. Particles with Stokes number higher than unity are believed to be more weakly coupled to the carrier flow due to their larger inertia. The instantaneous particle concentrations in Fig. 13 show that the more inertial particles are able to penetrate the shear layers that separate from the shoulders of the cylinder and thereafter proceed in the downstream direction relatively unaffected by the alternatingly shed vortex cells, as visualized by color contours of spanwise vorticity ω_z. This leads to the formation of a *void shadow* in the near wake, in contrast to the void cells formed by the $Sk = 1$ particles in Fig. 2. The void shadow extends further downstream with increasing inertia, i.e. higher Sk, and thereby postpones the appearance of coherent void cells encompassing the Kármán vortex cells. The increasing particle concentration in high-vorticity regions reflects that the more inertial particles behave ballistically and essentially decouple from the local fluid. The gradually increasing decoupling is caused by the reduction of the factor in front of the slip velocity $\boldsymbol{U}_s$ in Eq. (3). Although coherent voids are formed further downstream in the wake with increasing Sk, smooth edges at the upstream side of the void holes can be observed at all Stokes numbers considered. At the downstream side of the voids, however, more particles are dis-

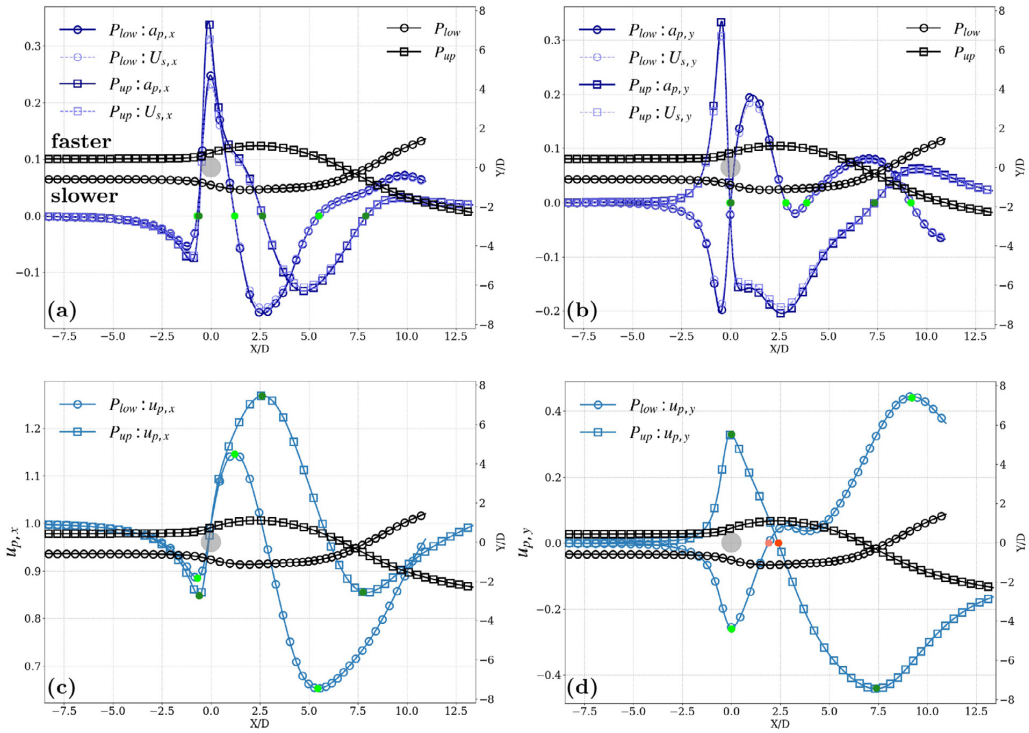

Fig. 12. (color online) Trajectories of two different particles landing on the upstream (P_{low}, circles) and downstream (P_{up}, squares) side of void hole no 3 at time t^* are plotted in all four panels. (a, b) Particle acceleration $\boldsymbol{a}_p$ and slip velocity $\boldsymbol{U}_s$ along the trajectories; (c, d) Particle velocity $\boldsymbol{u}_p$ along the trajectories. Streamwise components are shown in panels (a, c) to the left and cross-stream components in panels (b, d) to the right. The light and dark green dots in (a, c) identify the locations where the streamwise acceleration $a_{p,x}$ of the slow (low) and fast (up) particles changes sign. Similarly, the green dots in (b, d) identify the locations where the cross-stream acceleration $a_{p,y}$ changes sign, whereas the red dots indicate where the cross-stream velocity $u_{p,y}$ changes sign. (For interpretation of the references to colour in this figure legend, the reader is referred to the web version of this article.)

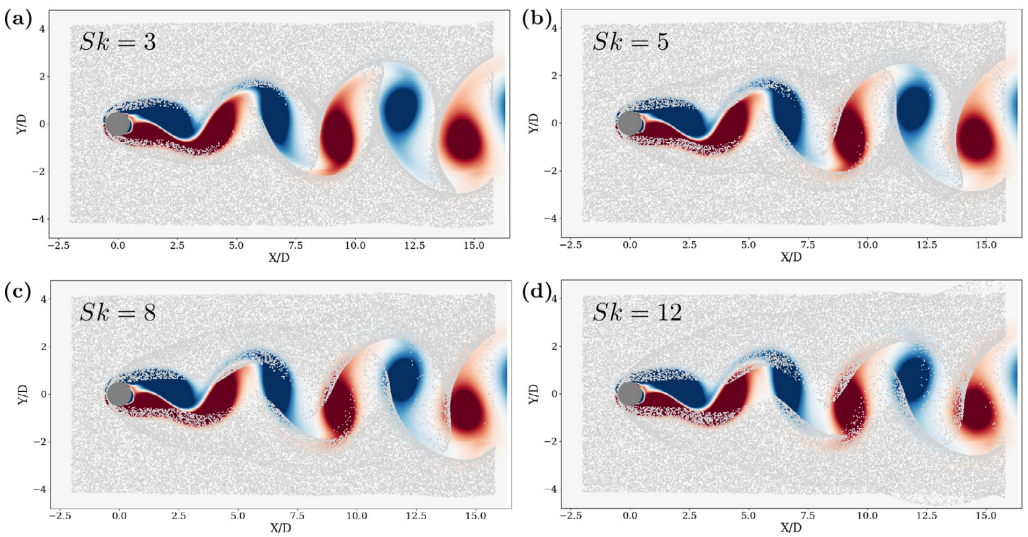

Fig. 13. (color online) Instantaneous distribution of heavier particles at time t^* superimposed with the spanwise vorticity ω_z. (a)$Sk = 3$ (b)$Sk = 5$ (c)$Sk = 8$ (d)$Sk = 12$.

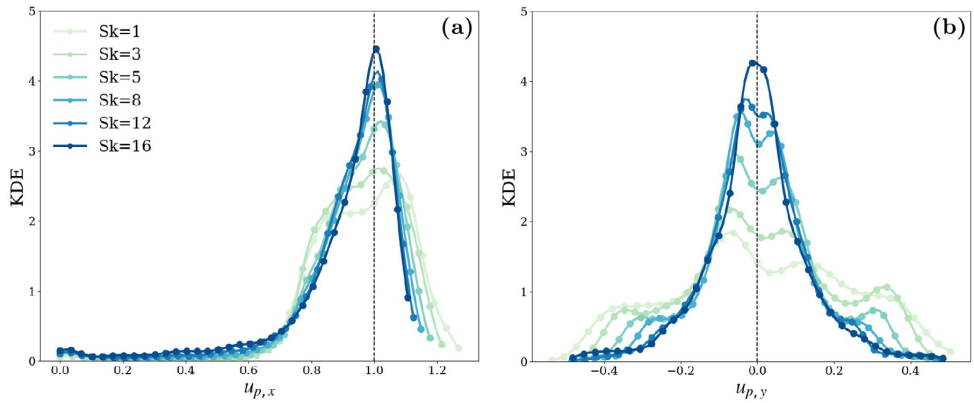

Fig. 14. (color online) KDEs of particle velocity at time t^* for six different Stokes numbers. (a)Particle velocity $u_{p,x}$ in the streamwise direction; (b)particle velocity $u_{p,y}$ in the cross-stream direction. Particles are sampled within X $\in [-0.5D, 15.8D]$.

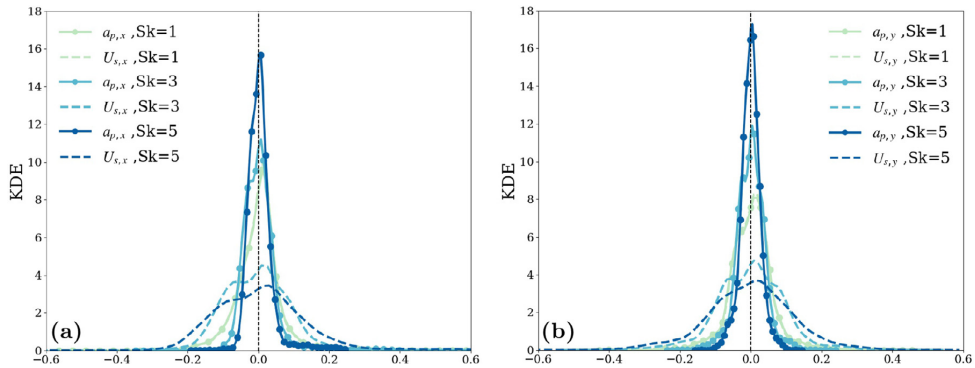

Fig. 15. (color online) KDEs of particle acceleration (solid lines) and slip velocity (dashed lines) at time t^* for three different Stokes numbers. (a)$a_{p,x}$ and $U_{s,x}$; (b)$a_{p,y}$ and $U_{s,y}$. Particles are sampled within X $\in [-0.5D, 15.8D]$.

persed around the cusps of the voids, as compared with the clustering of the $Sk = 1$ particles.

In addition to the phenomenological description of the particle concentration patterns in Fig. 13, we also make quantitative comparisons of the instantaneous distributions of the particle velocity, particle acceleration, and slip velocity for some different Stokes numbers to further investigate the effect of particle inertia. The peaks of the six KDEs of the streamwise particle velocity in Fig. 14(a) become higher with increasing inertia while the peak locations monotonically approach the freestream velocity U_0. A similarly increasing trend of the central peaks of the KDEs of the cross-stream particle velocity are seen in Fig. 14(b), whereas the secondary peaks at the tails of the KDE-distributions vanish with increasing particle inertia. Particle inertia makes the cross-stream velocity $u_{p,y}$ more concentrated around zero and in particular for the $Sk = 16$ particles for which the two secondary peaks do no longer exist. The left of the two near-by central peaks are consistently higher than the right one. We believe that this is caused by the wake topology at the particular time instant t^*, and we conjecture that the right one of the two central peaks will be the higher at $t^* + 1/2T$.

In Fig. 15, the streamwise and cross-stream components of $\boldsymbol{a}_p$ or $\boldsymbol{U}_s$ exhibit fairly similar KDE distributions. However, we observe a significant difference between $a_{p,y}$ and $U_{s,y}$ for the two highest Stokes numbers, namely that the latter is much flatter than that of $a_{p,y}$. With higher inertia most of the particles experience insignificant accelerations in spite of a non-negligible slip velocity. The $Sk = 1$ particles represent an exception, for which the KDEs of the particle acceleration and slip velocity almost coincide, as seen in Fig. 8(c). This suggests that the finite-Re correction $\beta \approx 1$ for the $Sk = 1$ particles, while β deviates from unity for higher Stokes numbers in accordance with the semi-empirical correlation in Eq. (2). This explains the decoupling between particle acceleration $\boldsymbol{a}_p$ and slip velocity $\boldsymbol{U}_s$ as an effect of inertia.

5. Conclusions

We performed three-dimensional numerical simulations of particle-laden fluid flow around a circular cylinder at $Re = 100$. The unsteady 2D flow is laden with inertial spherical particles characterized by a dimensionless Stokes number (Sk). Although previous studies dealt with particle dispersion in cylinder wake flow and/or vortex streets from various aspects, the topology of the particle concentration has never been analyzed in detail, similarly to how we have done in the present manuscript. We focused the investigation on $Sk = 1$ particles, for which it is observed that the inertial particles are expelled from certain parts of the flow field which accordingly appear as *coherent voids*. The local Kármán vortex cells in the near wake contributed to the formation of these voids. Each coherent void encompasses a Kármán vortex shed from the cylinder. An interesting phenomenon is that particles that cluster at the smooth upstream edge of a void hole surrounding a Kármán cell

shed from one side of the cylinder, originate from the other side of the cylinder with oppositely signed vorticity. We could therefore infer that the particles have followed trajectories deflected by a vortex cell shed from the other side. After one shedding period T, the smooth edge formed by particles clustering at the circumference of the next void that surrounds a Kármán vortex with the same sense of rotation. In contrast, a few particles are dispersed away from the downstream edge of each void, and this tendency becomes clearer with increasing Sk. The lack of experimental data unfortunately disables comparisons with our numerical results. We believe, however, that inclusion of inter-particle collisions naturally occurring in experimental configurations will tend to reduce the sharpness of the edges obtained from numerical simulations.Inter-particle collisions are believed to have only a modest influence on the particle clustering as long as the mass loading is low. Collisions, however, are likely to play a role in particle mixing at larger mass loadings which automatically lead to higher particle-particle collision frequencies.

The centrifugal mechanism is the primary reason for the formation of coherent voids, as shown by means of the Q-criterion conditioned on the particle positions. The majority of the particles around the shed vortices are located around the cusps of the vortex cores, while particles in the very near-wake would cast a void shadow which extends further downstream at high Sk as the particles behave more ballistically. However, the pattern formed by the smooth edges is linked to the history of particle movement. We first observed that the instantaneous velocity magnitudes of the particles forming the smooth edges are notably lower than that of the particles downstream of the void holes. This observation suggests that particles originating from different sides of the cylinder are differently affected by one and the same Kármán vortex cell.

The continuous trajectories of particles making up the smooth edges reveal a substantial deceleration period around the first detached shear layer, whereas an acceleration period is simultaneously experienced by the particles dispersed around the downstream edge of the coherent voids. Following a significant deceleration in the near wake, those particles close to the upper/lower parts of the same smooth edges are accelerated by the encompassed vortex core, while the central particles still proceed at lower speed. Therefore, the particles experienced a non-monotonic speed variation along their trajectories. This phenomenon reduces downstream, apparently along with the decaying strength of the vortex cores. The history effect reflected by particle trajectories essentially shapes the smooth edges. The collective effect of particle inertia and path memory could potentially prompt an in-depth examination of the objectivity of aerosol-type flow visualizations from a laboratory perspective, as indicated by Cimbala et al. (1988).

With increasing inertia, i.e. higher Sk, the void shadow extends further downstream due to the ballistic movement of the particles. The coherent voids are therefore formed further downstream than in wakes laden with $Sk = 1$ particles. Smooth edges are, however, still observed, although more particles are dispersed away from the downstream edge. Unlike the $Sk = 1$ case, higher particle inertia results in a decoupling of particle acceleration and slip velocity, together with a more inhomogeneous distribution of the instantaneous particle velocity.

Although the particle transportation in 3D turbulent flows appeals to practical applications more than laminar flows, the unsteadiness of dominant large-scale vortex shedding still perseveres. The LSSs in laminar wake flows, to some extent, also persist at high Re in spite of the intense turbulent fluctuations. Therefore, the investigation of particle clustering in the present 2D laminar cylinder wake is believed to share some features with wakes at higher Reynolds numbers.In higher-Re wakes, which inevitably also share some features with HIT, the potential role of other mechanisms, for instance sweep-stick clustering (Goto and Vassilicos 2008), should be explored and their relative importance should be compared with the centrifugal clustering mechanism.

Declaration of Competing Interest

None.

CRediT authorship contribution statement

Zhaoyu Shi: Software, Validation, Formal analysis, Investigation, Visualization, Data curation, Writing - original draft. **Fengjian Jiang:** Formal analysis, Writing - review & editing. **Lihao Zhao:** Writing - review & editing, Supervision. **Helge I Andersson:** Conceptualization, Writing - review & editing, Supervision, Project administration, Funding acquisition.

Acknowledgment

The first author greatly appreciates the technical support and guidance on MGLET from Dr. Håkon Strandenes and useful discussions with Dr. Pawel Baj. This work was supported by computational resources provided by Norwegian HPC infrastructure (www.sigma2.no), under project nn2649k granted by Norwegian Research Council. The financial support by NTNU Energy through a research fellowship is appreciated. L.Z. acknowledges the Natural Science Foundation of China (Grant Nos: 11911530141 and 91752205).

References

Aarnes, J.R., Haugen, N.E.L., Andersson, H.I., 2019. High-order overset grid method for detecting particle impaction on a cylinder in a cross flow. Int. J. Comput. Fluid Dyn. 33, 43–58.
Aliseda, A., Cartellier, A., Hainaux, F., Lasheras, J.C., 2002. Effect of preferential concentration on the settling velocity of heavy particles in homogeneous isotropic turbulence. J. Fluid Mech. 468, 77–105.
Bagchi, P., Balachandar, S., 2003. Inertial and viscous forces on a rigid sphere in straining flows at moderate Reynolds numbers. J. Fluid Mech. 481, 105–148.
Bagheri, M., Sabzpooshani, M., 2020. On the importance of the history force in dispersion of particles in von Kármán vortex street. Adv. Powd. Tech. 31, 3897–3909.
Bec, J., Biferale, L., Boffetta, G., Celani, A., Cencini, M., Musacchio, S., Toschi, F., 2006. Acceleration statistics of heavy particles in turbulence. J. Fluid Mech. 550, 349–358.
Bec, J., Biferale, L., Boffetta, G., Cencini, M., Musacchio, S., Toschi, F., 2006. Lyapunov exponents of heavy particles in turbulence. Phys. Fluids 18, 091702.
Bec, J., Biferale, L., Cencini, M., Lanotte, A., Musacchio, S., Toshi, F., 2007. Heavy particle concentration in turbulence at dissipative and inertial scales. Phys. Rev. Lett. 98, 084502.
Benczik, I.J., Toroczkai, Z., Tél, T., 2002. Selective sensitivity of open chaotic flows on inertial tracer advection: Catching particles with a stick. Phys. Rev. Lett. 89, 164501.
Bragg, A.D., Collins, L.R., 2014. New insights from comparing statistical theories for inertial particles in turbulence: I. Spatial distribution of particles. New J. Phys. 16, 055013.
Burger, M., Schmehl, R., Koch, R., Wittig, S., Bauer, H.-J., 2006. DNS of droplet-vortex interaction with a Kármán vortex street. Int. J. Heat Fluid Flow 27, 181–191.
Burns, T.J., Davis, R.W., Moore, E.F., 1999. A perturbation study of particle dynamics in a plane wake flow. J. Fluid Mech. 384, 1–26.
Candelier, F., Angilella, J.R., Souhar, M., 2004. On the effect of the Boussinesq-Basset force on the radial migration of a Stokes particle in a vortex. Phys. Fluids 16, 1765–1776.
Cimbala, J.M., Nagib, H.M., Roshko, A., 1988. Large structure in the far wakes of two-dimensional bluff bodies. J. Fluid Mech. 190, 265–298.
Cliff, R., Grace, J., Weber, M.E., 1978. Bubbles, drops, and particles. Academic Press, New York.
Coleman, S.W., Vassilicos, J.C., 2009. A unified sweep-stick mechanism to explain particle clustering in two- and three-dimensional homogeneous, isotropic turbulence. Phys. Fluids 21, 113301.
Daitche, A., Tél, T., 2011. Memory effects are relevant for chaotic advection of inertial particles. Phys. Rev. Lett. 107, 244501.
Daitche, A., Tél, T., 2014. Memory effects in chaotic advection of inertial particles. New J. Phys. 16, 073008.
Dressaire, E., Sauret, A., 2017. Clogging of microfluidic systems. Soft Matter 13, 37–48.
Eaton, J.K., Fessler, J.R., 1994. Preferential concentration of particles by turbulence. Int. J. Multiphase Flow 20, 169–209.
Ferziger, J.H., Tseng, Y.-H., 2003. A ghost-cell immersed boundary method for flow in complex geometry. J. Comput. Phys. 192, 593–623.

Gijs, M.A.M., Lacharme, F., Lehmann, U., 2010. Microfluidic applications of magnetic particles for biological analysis and catalysis. Chem. Rev. 110, 1518–1563.
Gibert, M., Xu, H., Bodenschatz, E., 2012. Where do small, weakly inertial particles go in a turbulent flow? J. Fluid Mech. 698, 160–167.
Gobert, C., 2010. Large Eddy Simulation of Particle-Laden Flow. Technical University of Munich Ph.D. dissertation.
Goto, S., Vassilicos, J.C., 2008. Sweep-stick mechanism of heavy particle clustering in fluid turbulence. Phys. Rev. Lett. 100, 054503.
Haller, G., Sapsis, T., 2008. Where do inertial particles go in fluid flows? Physica D 237, 573–583.
Haugen, N.E.L., Kragset, S., 2010. Particle impaction on a cylinder in a crossflow as function of Stokes and Reynolds numbers. J. Fluid Mech. 661, 239–261.
Hunt, J.C.R., Wray, A.A., Moin, P., 1988. Eddies, streams, and convergence zones in turbulent flows. In: Studying Turbulence Using Numerical Simulation Databases, 2. Proceedings of the 1988 Summer Program. Center for Turbulence Research, Stanford
Ireland, P.J., Bragg, A.D., Collins, L.R., 2016. The effect of Reynolds number on inertial particle dynamics in isotropic turbulence. Part 1. Simulations without gravitational effects. J. Fluid Mech. 796, 617–658.
Jayaram, R., Jie, Y., Zhao, L., Andersson, H.I., 2020. Clustering of inertial spheres in evolving Taylor-Green vortex flow. Phys. Fluids 32, 043306.
Jacobs, G.B., Armstrong, K., 2009. Inertial particle dispersion in the Lagrangian wake of a square cylinder. 47th AIAA Aerospace Sciences Meeting Including the New Horizons Forum and Aerospace Exposition. Orlando
Jung, C., Tél, T., Ziemniak, E., 1993. Application of scattering chaos to particle transport in a hydrodynamical flow. Chaos 32, 555–568.
Kulick, J.D., Fessler, J.R., Eaton, J.K., 1994. Particle response and turbulence modification in fully developed channel flow. J. Fluid Mech. 277, 109–134.
Lee, W., Amini, H., Stone, H.A., Di Carlo, D., 2010. Dynamic self-assembly and control of microfluidic particle crystals. PNAS 107, 22413–22418.
Luo, L., Fan, J., Li, W., Cen, K., 2009. Transient, three-dimensional simulation of particle dispersion in flows around a circular cylinder (Re=140-260). Fuel 88, 1294–1301.
Manhart, M., Friedrich, R., 2002. DNS of a turbulent boundary layer with separation. Int. J. Heat Fluid Flow 23, 572–581.
Manhart, M., Tremblay, F., Friedrich, R., 2001. MGLET: a parallel code for efficient DNS and LES of complex geometries. In: Parallel Computational Fluid Dynamics 2000. Elsevier, Amsterdam, pp. 449–456.
Maxey, M.R., Riley, J.J., 1983. Equation of motion for a small rigid sphere in a nonuniform flow. Phys. Fluids 26, 883–889.
Mohammadreza, M., Bragg, A.D., 2020. Local analysis of the clustering, velocities, and accelerations of particles settling in turbulence. Phys. Rev. Fluids 5, 034306.
Monchaux, R., Bourgoin, M., Cartellier, A., 2010. Preferential concentration of heavy particles: A Voronoï analysis. Phys. Fluids 22, 103304.
Monchaux, R., Bourgoin, M., Cartellier, A., 2012. Analyzing preferential concentration and clustering of inertial particles in turbulence. Int. J. Multiphase Flow 40, 1–18.
Mowlavi, S., Arratia, C., Gallaire, F., 2016. Spatio-temporal stability of the Kámán vortex street and the effect of confinement. J. Fluid Mech. 795, 187–209.
Petersen, A.J., Baker, L., Coletti, F., 2019. Experimental study of inertial particles clustering and settling in homogeneous turbulence. J. Fluid Mech. 864, 925–970.
Raju, N., Meiburg, E., 1997. Dynamics of small, spherical particles in vortical and stagnation point flow fields. Phys. Fluids 9, 299–314.
Salazar, J.P.L.C., De Jong, J., Cao, L., Woodward, S.H., Meng, H., Collins, L.R., 2008. Experimental and numerical investigation of inertial particle clustering in isotropic turbulence. J. Fluid Mech. 600, 245–256.
Shi, Z., Jiang, F., Strandenes, H., Zhao, L., Andersson, H.I., 2020. Bow shock clustering in particle-laden wetted cylinder flow. Int. J. Multiphase Flow 130, 103332.
Squires, K.D., Eaton, J.K., 1991. Preferential concentration of particles by turbulence. Phys. Fluids A 3, 1169–1178.
Tang, L., Wen, F., Yang, Y., Crowe, C.T., Chung, J.N., Troutt, T.R., 1992. Self-organizing particle dispersion mechanism in a plane wake. Phys. Fluids A 4, 2244–2251.
Wang, L., Maxey, M.R., 1993. Settling velocity and concentration distribution of heavy particles in homogeneous isotropic turbulence. J. Fluid Mech. 256, 27–68.
Wen, F., Kamalu, N., Chung, J.N., Crowe, C.T., Troutt, T.R., 1992. Particle dispersion by vortex structures in plane mixing layers. J. Fluids Eng. 114, 657–666.
Yang, Y., Crowe, C.T., Chung, J.N., Troutt, T.R., 2000. Experiments on particle dispersion in a plane wake. Int. J. Multiphase Flow 26, 1583–1607.
Yao, J., Zhao, Y., Hu, G., Fan, J., Cen, K., 2009. Numerical simulation of particle dispersion in the wake of a circular cylinder. Aerosol Sci. Technol. 43, 174–187.
Yoshimoto, H., Goto, S., 2007. Self-similar clustering of inertial particles in homogeneous turbulence. J. Fluid Mech. 577, 275–286.
Zaichik, L.I., Alipchenkov, V.M., 2007. Refinement of the probability density function model for preferential concentration of aerosol particles in isotropic turbulence. Phys. Fluids 19, 113308.
Zhou, H., Mo, G., Cen, K., 2011. Numerical investigation of dispersed gas-solid two-phase flow around a circular cylinder using lattice Boltzmann method. Comput. Fluids 52, 130–138.

Article IV

Scale-dependent particle clustering in transitional wake flow

Zhaoyu Shi, Fengjian Jiang, Lihao Zhao, Helge I. Andersson

Under revision for publication in Journal of Fluid Mechanics, 2021

This article is awaiting publication and is therefore not included.

Article V

Particle concentration in turbulent cylinder wake flow

Zhaoyu Shi, Fengjian Jiang, Lihao Zhao, Helge I. Andersson

To be submitted to Physics Review Fluids, 2022

This article is awaiting publication and is therefore not included.

Article VI

Different topologies of natural vortex dislocations in mode-A wake

Cai Tian, Zhaoyu Shi, Fengjian Jiang, Helge I. Andersson

Accepted for publication in Physics of Fluids Letter, 2022

This article is awaiting publication and is therefore not included.